

Magnetic Order in
Atomic Contacts
of Strong Paramagnets

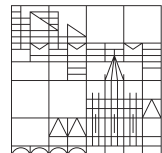
**Dissertation submitted for the Degree of
Doctor of Natural Sciences (Dr.rer.nat.)**

presented by

Martin Wilhelm Prestel

at the

Universität
Konstanz



Faculty of Mathematics and Natural Sciences
Department of Physics

Konstanz, 2020

Tag der mündlichen Prüfung: 27. November 2020

1. Referentin: Prof. Dr. Elke Scheer
2. Referent: Prof. Dr. Wolfgang Belzig

Contents

Contents	1
Deutschsprachige Zusammenfassung	5
1 Introduction	7
2 Magnetism in Atomic Contacts	9
2.1 Mesoscopic Transport	9
2.1.1 Atomic Contacts	10
2.1.2 Formation of Atomic Chains	11
2.2 Magnetic Order	12
2.2.1 Ferromagnetic Atomic Contacts	14
2.2.2 The Kondo Effect	16
2.3 Magnetism in Atomic Contacts of Strong Paramagnets	17
2.3.1 Simulations on the Magnetic Order in Atomic Contacts and Chains .	18
2.3.2 Experimental Evidence from Transport Measurements	19
2.3.3 Stretching of Atomic Contacts	29
2.3.4 Kondo effect in Strong Paramagnets	31
3 Shot Noise	35
3.1 Theoretical Background	35
3.1.1 Shot Noise in Atomic Contacts	37
3.1.2 Shot Noise and Magnetism	41
3.2 Sample Preparation	43
3.2.1 General Process	44
3.2.2 Sample Layout	45
3.3 The Cryostat	46
3.3.1 Electrical Setup	46
3.3.2 Measurement Electronics	47
3.3.3 Measurement Procedure and Data Storage	48
3.4 Digital Data Processing	49
3.4.1 IV Curves	49
3.4.2 Peak Removal	49

3.4.3 Noise Modeling	50
3.4.4 Fano Factor Analysis	52
3.4.5 Limits and Uncertainties of the Noise Modeling	53
3.4.6 Phonon Energy	55
3.5 Results	56
3.5.1 Gold – Reference Material	57
3.5.2 Cobalt – Ferromagnetic Reference	57
3.5.3 Platinum	62
3.5.4 Palladium	63
3.5.5 Comparison between strong paramagnets	65
3.6 Summary	67
4 Spin Polarization Investigated by Multiple Andreev Reflection	69
4.1 Theoretical Background	69
4.1.1 BCS Theory	70
4.1.2 Weakly Coupled Superconductors	71
4.1.3 Channel Analysis with MAR	72
4.1.4 Effect of Magnetic Impurities on MAR	73
4.2 Sample Preparation	77
4.2.1 Shadow Evaporation	77
4.2.2 Multi-Step Lithography	78
4.3 The Setup	82
4.3.1 The Cooling System	82
4.3.2 Breaking Mechanics	82
4.3.3 Wiring and Filters	83
4.3.4 Measurement Electronics	85
4.3.5 Measurement Procedure and Data Storage	86
4.3.6 Fitting Procedure of the Superconducting IV Curves	87
4.4 Results	89
4.4.1 Aluminium	89
4.4.2 Proximity Superconductivity: Aluminium and Gold	91
4.4.3 Aluminium – Palladium: Shadow Evaporation	96
4.4.4 Aluminium – Palladium: Multi-Step Lithography	99
4.5 Discussion	104
5 Conclusion	107
Bibliography	109
Danksagung	125

A Appendix	127
A.1 Noise Setup	127
A.1.1 Adder	127
A.1.2 IV Converter	129
A.2 MAR Setup	131
A.2.1 Adder MAR Setup	131
A.2.2 Chirp Noise of the Voltage Source	131
A.2.3 Shift in Magnetic Field	131

Deutschsprachige Zusammenfassung

Die fortschreitende Verkleinerung von elektronischen Bauteilen, wie integrierte Schaltkreise und Speicherbausteine, kommt an eine physikalische Grenze, die durch die schiere Größe und die dissipierte Leistung gegeben ist. Eine Möglichkeit, die entstehende Wärme zu reduzieren, ist Spintronik, Elektronik mit Spins anstatt Ladungen. Die Eigenschaft der Spins hängt direkt mit dem Magnetismus zusammen, daher muss man verstehen, wie Magnetismus auf der atomaren Skala entsteht.

In dieser Arbeit wurden atomare Kontakte aus starken Paramagneten auf das Vorhandensein von magnetischer Ordnung untersucht. Dazu wurden an dem starken Paramagneten Iridium verschiedene elektronische Transportmessungen durchgeführt und auf indirekte Hinweise auf Magnetismus untersucht. Ein direkter Nachweis magnetischer Ordnung ist über den Nachweis von Spin-Polarisation möglich. Dazu gibt es zwei Möglichkeiten: Erstens die Methode über das Schrotrauschen und zweitens die Analyse von supraleitenden Strom-Spannungs-Kennlinien (*IV*-Kennlinien), deren Nichtlinearitäten auf Spin-Polarisation oder sogar magnetische Momente hinweisen können.

Durch Untersuchungen von Transporteigenschaften mit angelegtem Magnetfeld und ohne wurde in atomaren Kontakten aus den starken Paramagneten Palladium und Platin bereits ein indirekter Nachweis von magnetischer Ordnung erbracht. Der Nachweis der magnetischen Ordnung in atomaren Kontakten aus Iridium stand noch aus. In dieser Arbeit wurden atomare Kontakte mit lithographisch definierten Bruchkontakten hergestellt und mit Hilfe von magnetischen Feldern untersucht. Die Ergebnisse zeigen eine große, nicht monotone Abhängigkeit des Leitwerts vom magnetischen Feld (Magnetoleitwert, MC) sowie eine anisotrope Leitwertsänderung mit 10 % Effektgröße (anisotroper Magnetoleitwert, AMC). Die Form und die Amplitude sowohl des MC als auch des AMC lassen sich durch Dehnen der Kontakte modifizieren. Ein weiterer Hinweis auf das Vorhandensein einer magnetischen Ordnung sind Anomalien bei null Spannung (zero bias anomaly, ZBA). Diese ZBAs konnten mit der Theorie für den Kondo-Effekt beschrieben werden und für Iridium wurde eine Verteilung der Kondo-Temperatur mit Maxima bei 26 K und 125 K bestimmt.

Für den Nachweis von Spin-Polarisation wurde ein Versuchsaufbau für die Messung von Schrotrauschen ausgerüstet. Hierzu musste die Verkabelung eines bestehenden Aufbaus auf möglichst geringe Kapazität optimiert und der verwendete Strom-Spannungs-Verstärker charakterisiert werden. Mit Messungen an Gold konnte der Versuchsaufbau getestet werden. An

Cobalt konnte gezeigt werden, dass es möglich ist Spin-Polarisation nachzuweisen. Die starken Paramagneten Palladium, Platin und Iridium zeigen hingegen keine oder keine eindeutige Spin-Polarisation, jedoch ist für atomare Kontakte eine Häufung der Messdaten an der Grenze des Bereichs des spin-polarisierten Transports erkennbar.

Auch die zweite Nachweismethode für Spin-Polarisation über multiple Andreev-Reflexionen, Nichtlinearitäten in supraleitenden *IV*-Kennlinien, wurde verwendet, um magnetische Momente in atomaren Kontakten aus starken Paramagneten zu zeigen. Dafür musste ein Kryostat, der Temperaturen $< 20\text{ mK}$ erreicht, zur Verwendung mit Bruchkontakte ausgerüstet und getestet werden. An Proben aus Aluminium und Aluminium – Gold konnte gezeigt werden, dass der Aufbau für die Messung von supraleitenden *IV*-Kennlinien geeignet ist. Die Probenherstellung für die Hybridproben aus Palladium und Aluminium erwies sich als herausfordernd. Die erste verwendete Methode, Schattenbedämpfung, welche für Aluminium – Gold problemlos funktionierte, stieß bei Aluminium – Palladium, bedingt durch die mechanischen Spannungen im Palladiumfilm, an ihre Grenzen. Außerdem sind bei Palladium deutlich dickere Schichten nötig, damit die Probe leitfähig ist, was jedoch durch den inversen Proximity-Effekt zu einer starken Unterdrückung der Supraleitung führt. Die zweite Möglichkeit, eine Mehrschritt-Lithographie, erwies sich auf dem isolierenden Substrat als sehr herausfordernd. Daher war es nur möglich zwei funktionierende Proben zu messen. Die *IV*-Kennlinien der einen Probe sind durch den inversen Proximity-Effekt deutlich verrundet, trotzdem konnte hier ein erster Hinweis auf Spin-Polarisation oder zumindest das Vorhandensein eines magnetischen Moments gefunden werden. Die zweite Probe zeigt zwar im Histogramm Signale, die auf Palladium hinweisen, jedoch weisen die *IV*-Kennlinien auf einen Kontakt zwischen Aluminium und Palladium hin. Hier konnten keine eindeutigen Hinweise für Spin-Polarisation oder magnetische Momente gefunden werden.

Zusammenfassend kann gesagt werden, dass es durch indirekte Transportmessungen möglich war, Hinweise auf eine magnetische Ordnung in atomaren Kontakten aus starken Paramagneten zu finden. Hinweise auf eine Spin-Polarisation in solchen Kontakten konnten jedoch nicht eindeutig bestätigt werden. Messungen mittels supraleitender Kontakte zeigten für eine Probe eine Veränderung der *IV*-Kennlinien, welche auf Magnetismus hindeutet.

Chapter 1

Introduction

The ongoing digitization of the world requires increasing number of transistors in a circuit as well as an increasing amount of storage. The number of transistors on a chip doubles every two years, additionally, the size of one transistors reduces constantly [Moo65]. This leads to an increase of power density on a standard chip, which produces unwanted heat [BRK05]. Additionally, the size of a transistors is limited by the minimum distance between gate and channel. One possible solution to reduce the power consumption is to reduce the current flowing. The net transport of electrons could be reduced to zero, if spintronics is used [WCT06]. The reduction in feature size of magnetic bits is limited by the superparamagnetic effect [GM12, p. 736]. Both, spintronics and the minimum size of a magnetic bit, need information about the emergence of magnetism at the atomic scale.

One promising system to analyze the properties of magnetism on the atomic scale are strong paramagnets. For these materials it has been calculated, that a magnetic order evolves at the atomic scale [DT03]. First transport measurements on platinum [Str+15] and palladium [Str+16] show a big, non-monotonous magneto-conductance, a first sign of the predicted magnetic order. In this work, the third metal iridium is investigated for the same signatures. Additionally, the presence of spin-polarized transport through such contacts is investigated. There are two different methods to analyze the electrical transport through a ballistic contact: shot noise and multiple Andreev reflection. The first method uses the suppression of current noise for fully transmitting channels [BR99]. The latter one makes use of superconducting properties and the resulting non-linearities in the current voltage (*IV*) curves [Sch+98]. For both methods a setup was designed and characterized. First measurements on strong paramagnets were carried out.

This work is structured as followed: In [chapter 2](#), the transport through atomic contacts and the influence of magnetism on the transport through single atoms is discussed. The results of atomic contacts of strong paramagnets are discussed and exemplified in detail for iridium. One way to measure direct evidence of spin-polarization is through shot noise. This method is discussed in [chapter 3](#). First, the non-magnetic theory and then the influence of magnetism

on shot noise is presented, followed by the experimental setup and the sample preparation. The measurement of gold, cobalt, and the strong paramagnets palladium and platinum are discussed. A short comparison between the strong paramagnets platinum, palladium and iridium is drawn.

A second option to probe the presence of spin-polarization are multiple Andreev reflections. With this technique, presented in [chapter 4](#), it is also possible to detect local magnetic moments. To understand the experiment, an introduction to the theory is given first. Then the setup and the sample preparation, including the difficulties, are presented. To validate the results of this setup, control measurements on aluminium and aluminium – gold are presented, followed by results on aluminium – palladium.

All results are summarized in [chapter 5](#).

Chapter 2

Magnetism in Atomic Contacts

To understand how a spin-polarized transport through an atomic contact is possible, first the magnetic order in such contacts should be explained. In this chapter I introduce the transport mechanism in atomic contacts (see [section 2.1](#)) and the influence of magnetism on the transport through atomic contacts ([section 2.2](#)). In [section 2.3](#) I focus on simulations and measurements of atomic contacts made of strong paramagnets like platinum, palladium, and particularly iridium, which was measured in the framework of this thesis.

2.1 Mesoscopic Transport

The explanation of the transport in atomic contacts requires the consideration of the length L of the sample. For large samples with length $L \gg l_e$, the mean free path, the electrical transport is diffusive, meaning that electrons or other charge carriers, undergo many scattering events while passing the sample. Therefore, the transport is dominated by these scattering events and one can describe it with Ohm's law $R = \rho \frac{L}{A}$. Here, ρ is the resistivity and A the cross section of the conductor. For the opposite case, $L < l_e$ the transport is ballistic, meaning there are no scattering events for charge carriers inside sample. Hence, the momentum of the charge carriers is conserved in the sample. A second differentiation of the transport regime can be done using the phase coherence length l_ϕ , which states over which distance charge carriers are able to interfere with each other. This length is limited by the number of inelastic scattering events. Samples with $l_\phi > L$ are called mesoscopic [[CS10](#)].

For atomic contacts, another length is important for the transport of charge carriers. If the Fermi wavelength λ_F is bigger than the width of the sample W , one talks about quantum point contacts. In this case the transport is limited to so called channels with a defined transmission. A perfect transmitting channel leads to a conductance equal to the conductance quantum $G_0 = \frac{2e^2}{h} = 7.75 \times 10^{-5} \text{ S}$ in the case of spin-degeneracy. The transport in atomic

contacts is not limited to perfectly transmitting channels. Due to the valence of the used metal(s), multiple channels with arbitrary transmission are possible. A theoretical model, which also applies to atomic contacts, has been published by Landauer [Lan70]. For n channels with transmissions $\{\tau_i\}$, one gets

$$G = \frac{2e^2}{h} \sum_{i=1}^n \tau_i = G_0 \sum_{i=1}^n \tau_i \quad (2.1)$$

for the overall conductance of the contact [AYR03].

2.1.1 Atomic Contacts

There are different approaches to the formation of atomic contacts and chains. The three main methods are using a scanning tunneling microscope (STM), electromigration, and a mechanically controllable break junction (MCBJ) [AYR03; CS10; Wie94; Hof17; Rui+96]. In the following, the advantages and disadvantages of the different approaches are discussed.

The mechanically most stable method is the electromigration [Hof08; Hof17]. There, one defines a structure with a constriction directly on the substrate. The atomic contact is then formed by controlled thinning of the constriction using high currents. This method relies on the local heating of the constriction and the atoms in the constriction are then transported away by electrical forces. The direct contact with the substrate makes the contact robust against mechanical distortion. With this method it is only possible to change the junction from a closed to an open state, i.e. from low to high resistance of the junction. Thus, one is not able to form multiple junctions using one sample.

The most versatile method for forming atomic contacts is the STM. There, one crashes the STM tip into the sample and forms an atomic contact by retracting the tip. Not only ripping apart a contact, but also forming is possible [GM87; ARV93]. The two main advantages of the STM are the speed and the flexibility. The fast movement of the tip, caused by the piezo drive, enables fast contact formation. The lateral movement of the tip allows to use fresh surfaces to form new contacts or even contacting adatoms and molecules on sample surface. Combining a STM with an AFM (atomic force microscope) adds the possibility of measuring the force of the breaking process [RK06; MK06]. However, the drawback of the STM configuration is the low long-term stability of the contacts due to vibration and piezo creep, especially when changing temperature or in magnetic fields.

A compromise between electromigration and STM, in the means of flexibility and stability, is the MCBJ technique [Rui+96; AYR03]. A sample, consisting of a metal with a defined constriction on a flexible substrate, is placed in a three point bending mechanism (see figure 2.1). The relative movement of the pushing rod toward the counter supports leads to a bending of the

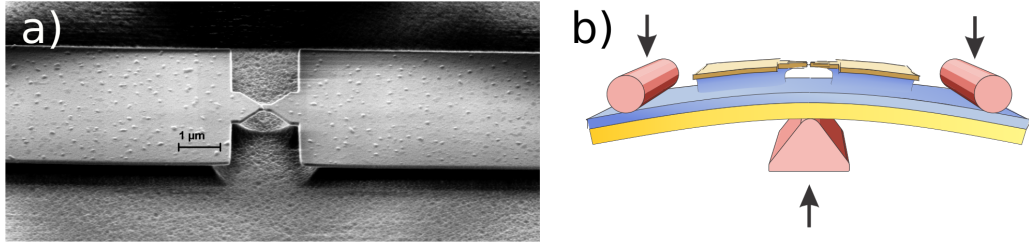


Figure 2.1: In a) a SEM picture of a lithographically defined break junction after measurement is shown. The scale bar is 1 μm long. b) Working principle of a MCBJ: The sample is mounted between two counter supports (round) and the pushing rod (the relative displacement between them is marked by arrows). The bending of the sample translates into a stretching of the constriction.

sample. This bending, in turn, results in a strain in the constriction and with increasing strain the metal starts to rupture. Since the substrate is elastic, it is also possible close the sample again, when retracting the pushing rod [AYR03]. There are two possibilities to place the metal on the substrate. The notched-wire technique uses a thin metal wire, which is notched in the middle and glued to the substrate at two points on either side of the notch. The second approach defines the break junction on the substrate using lithography [Vro+05]. This second approach is used in the present work. The advantages are the reversibility of the breaking process and the high stability compared to STM junctions. The stability originates from the reduction between the movement of the pushing rod and the movement between the two tips. This stability makes it possible to measure contacts over several days, if the whole system remains undisturbed. The drawback of the MCBJ is the slow speed of several minutes to open a contact and the reduced flexibility in choosing the location of the atomic contact.

2.1.2 Formation of Atomic Chains

Not only the formation of atomic contacts is possible, but for some metals it is also possible to prepare atomic chains. Metals which are known for forming atomic chains are gold, iridium, and platinum [RU01; RK06; KM09]. There are special requirements for the formation of atomic chains which are mainly material dependent [Smi+01]. Adding oxygen to the chain facilitates the formation of chains also in elements, which do not form chains in vacuum [Thi+06]. One experimental evidence for the formation of atomic chains is the length of the last conductance plateau in stretching experiments. Using STM or MCBJ enables to calculate the elongation of the chain by knowing the length of a single atom. Additionally, the conductance changes periodically while stretching the contact. Exact measurements show even-odd oscillations, when adding atoms to the chain [Smi+03]. These oscillations are material dependent and are well visible in gold and the oxidized chains, but not so pronounced in platinum and iridium [Smi+03].

To understand the process of chain formation, many calculations on different metals have been performed [Rub+01; BJ01; SSF01] and Thiess *et al.* published a comprehensive theory of chain formation [Thi+08]. In their work, the two main criteria for chain formation are the producibility and the stability of an atomic chain. Both rely on energy considerations of a stretched chain with an interatomic distance d . The chain is stable as long as the energy of a chain with $N + 1$ bindings (N atoms) with distance d is smaller than the energy of a chain with N bindings with equilibrium distance d_0 and the energy of one broken bond. The producibility is the criterion for adding a new atom to a stretched chain. Thiess *et al.* consider a chain with $N + 1$ atoms at a stretched interatomic distance d and calculate the energy difference to a chain with relaxed distance \hat{d} with an additional atom in the chain. As shown in their article, Thiess *et al.* find a region for chain formation for the three transition metals gold, platinum, and iridium as well as for gold – oxygen chains and silver – oxygen chains. In a subsequent article, Thiess *et al.* also investigated the influence of magnetic order on the formation of atomic contacts [Thi+09]. They calculated stability diagrams for different materials with and without a magnetic order. They assumed that the ground state is mainly ferromagnetic, but for tungsten and rhenium an anti-ferromagnetic ground state is taken into account. These calculations lead to an energy difference between the (anti-)ferromagnetic and non-magnetic state for a given atomic distance. Using this energy difference, they conclude that for most investigated materials the presence of a magnetic state hinders the formation of an atomic chain.

2.2 Magnetic Order

To understand magnetism in reduced dimensions, a short introduction into magnetism is given. A detailed description of different magnetic effects can be found in [Blu01; GM12]. To understand the magnetism at the atomic scale, two models for itinerant electrons are important: the Pauli paramagnetism and band ferromagnetism.

Pauli paramagnetism is a simple model to explain a positive susceptibility χ . A positive χ means an external magnetic field B_{ext} features a magnetization M in the same direction as the applied magnetic field. The most important ingredient is the magnetic moment based on the spin of the electrons: $\mu_s = -g_s m_s \mu_B$. For negligible orbital effects the Landé factor $g = 2$. $m_s = \pm 1/2$ is the spin quantum number and $\mu_B = \frac{e\hbar}{2m_e}$ the Bohr magneton. Due to the external magnetic field, the electrons with spin parallel to the applied magnetic field, named spin-up, are lowered in energy. The electrons with opposite spin, spin-down, are subject to an increase in energy. This shift in energy leads to a rearrangement of the electrons increasing the number of spin-up electrons. The resulting magnetization reads

$$M_{\text{Pauli}} = D(E_F) \mu_B^2 B_{\text{ext}} \quad (2.2)$$

with the density of states $D(E_F)$ at the Fermi energy. A simplified picture of the split density of states is shown in figure 2.2 a). The susceptibility is reduced if orbital effects are included:

$$\chi_{\text{Landau}} = -\frac{1}{3} \left(\frac{m_e}{m^*} \right)^2 \chi_{\text{Pauli}}. \quad (2.3)$$

m^* is the effective electron mass, which is $m^* = m_e$ for most metals, leading to a paramagnetic behavior of these metals. Prominent exceptions are the noble metals gold, silver, and copper.

To explain ferromagnetic order, a spontaneous spin splitting, meaning a rearrangement of electrons from spin-down to spin-up, is needed. For a stable rearrangement of electrons, it has to be energetically preferred. Therefore, one assumes a non-split density of states, as shown in figure 2.2 b), and places some electrons of the spin-down band into the spin-up band. This costs some kinetic energy

$$E_{\text{kin}} = \frac{1}{2} D(E_F) (\delta E)^2, \quad (2.4)$$

with the energy δE between E_F and the uppermost energy of the transferred electrons. There are more electrons with spin-up, leading to a local magnetization resulting in an energy reduction

$$E_{\text{pot}} = -\frac{1}{4} U (D(E_F) \delta E)^2 \quad (2.5)$$

with the material dependent Stoner parameter U [Sto38; Sto39]. The total change in energy is, therefore,

$$\Delta E = E_{\text{kin}} + E_{\text{pot}} = \frac{1}{2} D(E_F) (\delta E)^2 \left(1 - \frac{1}{2} U D(E_F) \right). \quad (2.6)$$

This energy change is negative if the Stoner criterion $\frac{1}{2} U D(E_F) - 1 \geq 0$ is fulfilled¹. For bulk materials, this is true for the three known band ferromagnets iron, cobalt, and nickel. If the Stoner criterion is not fulfilled, there is no spontaneous spin-splitting and, therefore, no ferromagnetism. However, metals with $0 < \frac{1}{2} U D(E_F) < 1$ experience an enhancement of the susceptibility by

$$\chi = \frac{\chi_{\text{Pauli}}}{1 - \frac{1}{2} U D(E_F)} \quad (2.7)$$

in magnetic fields: The so called Stoner enhancement. Metals with a pronounced Stoner enhancement are strong paramagnets, e.g. palladium or platinum. Their exact properties are

¹Here, the definition $U = 2\mu_0\mu_B^2\gamma$ is used, with the mean field constant γ , connecting the mean field $B_A = \mu_0\gamma M_A$ with the magnetization. Others, like [Blu01], uses a the definition $U = \mu_0\mu_B^2\gamma$ and resolve a different looking Stoner criterion $UD(E_F) - 1 \geq 0$.

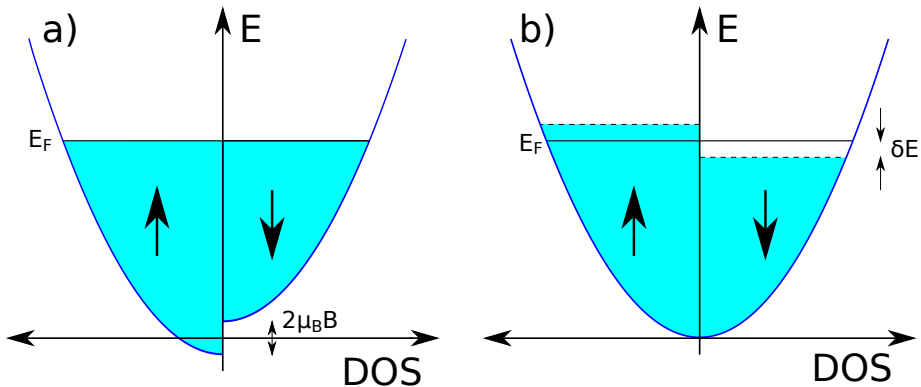


Figure 2.2: The density of states for two important magnetic phenomena are depicted. **a)** The density of states for Pauli paramagnetism with an external magnetic field B is shown. **b)** shows the density of state for deriving the band ferromagnetism according to Stoner. Adapted from [Blu01].

discussed in [section 2.3.2](#).

Since the factor $\frac{1}{2}UD(E_F)$ is also dependent on the density of states $D(E_F)$, a change of $D(E_F)$ will also change the Stoner enhancement. One possibility to change $D(E_F)$ is to change the coordination, i.e. the number of neighbors of the atoms and, as a result, the Stoner enhancement changes. Major changes in $D(E_F)$ might lead to a fulfilled Stoner criterion of ferromagnetism. Reducing the number of neighboring atoms can be achieved in small clusters consisting of few atoms or in atomic contacts and chains. Measurements of atomic contacts of ferromagnets are discussed in [section 2.2.1](#) and the effect of localized moments inside a junction is described in the framework of the Kondo effect (see [section 2.2.2](#)). The theory and experiments on strong paramagnets in reduced dimensions are presented in [section 2.3](#).

2.2.1 Ferromagnetic Atomic Contacts

First investigation of magnetism in atomic contacts have been performed by Ono *et al.* by studying histograms of atomic nickel contacts [[Ono+99](#)]. They found a pronounced transition from a quantization of $2e^2/h$ in zero magnetic field to half-quantization of e^2/h starting in magnetic fields around 100 Oe. This finding is in contrast to measurements published by Untiedt *et al.* [[Unt+04](#)]. They investigated atomic contacts of the three metals iron, cobalt, and nickel with and without a magnetic field of 5 T. The published histograms of Untiedt *et al.* do not show any differences between applied magnetic field and no magnetic field. One possible explanation for the differences found by Ono *et al.* and Untiedt *et al.* is the applied field scale of 100 Oe compared to 5 T. I am not aware of studies investigating the evolution of histograms with the magnetic field, thus a conclusion is not available.

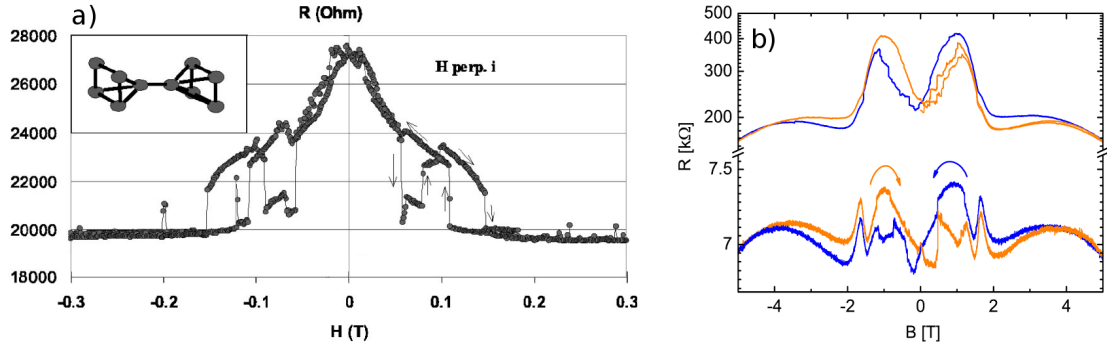


Figure 2.3: Magneto-resistance measurements of atomic contacts are shown for the ferromagnets nickel (a) and cobalt (b)). Taken from [Vir+02; Egl+10].

Other studies did not use a statistical approach, but looked at the behavior of the resistance of single contacts in magnetic field. The results of nickel [Vir+02; Wei+06; KYN06] and cobalt [Egl+10] are comparable (see figure 2.3). The characteristics of these measurements are rich, sweep direction dependent features, which are sometimes step-like, and a transition to a smooth, non-monotonous behavior above a certain field scale (~ 2 T for cobalt and ~ 0.2 T for nickel). The low-field features can be understood as local rearrangements due to magnetostriction (see below) or to overcome the local saturation fields. The features at high magnetic fields may be effects of spin-dependent scattering events (cf. section 2.3.2).

Further publications investigated the dependence of the resistance of such atomic contacts as a function of the angle between the current and the magnetic field. The results of these measurements is called anisotropic magneto-resistance (AMR). These measurements show a pronounced dependence of the resistance on the angle [BKR06; Vir+06; Sok+07; Aut+08]. Some of the curves show a two level behavior rather than a continuous transition, which one would expect from bulk measurements. This two level behavior was also subject of discussions [SR07]. One possible explanation is atomic movement in the contact region [Shi+07], since theory predicts either step-like [NN00; Chu+02] or continuous transitions [HVC09]. Another explanation is again magnetostriction, which is discussed in the following.

Magnetostriction describes a change in length (width/ volume) with respect to the applied magnetic field. This effect is known for a long time and has been investigated intensively for bulk materials [Lee95]. For atomic contacts, it is not easy to distinguish mechanical deformation caused by magnetostriction from effects based on electronic interactions, since it is hard to produce non-freestanding, tunable constrictions. Especially samples with long free-standing parts are prone to magnetostriction [CH15; Ien+12]. Nonetheless, Gabureac *et al.* tried to avoid magnetostrictive effects and proposed an experiment to exclude them [Gab+04]. They used a special sample geometry and adjusted the MCBJ in such a manner, that they have a tunneling contact. Any changes in position are now visible as changes in the tunnel current,

based on the exponential dependence of the tunnel current from the distance between the two tips.

2.2.2 The Kondo Effect

The Kondo effect was first measured in clean metals including a small amount of magnetic impurities [HBB34]. In these experiments, the resistance increases with falling temperature. This phenomenon was first covered theoretically by Kondo [Kon64] and later refined by Wilson [Wil75] using the Anderson model [And61]. An exact solution was developed in the 1980s with the Bethe ansatz [And80; Vig80]. An overview over the different models is given in [Hew93].

A more reliable way to identify the Kondo effect is by a zero-bias anomaly (ZBA) in dI/dV measurements. First measurements of this ZBA in ballistic contacts were done by Ralph and Buhrman [RB92; RB94] in disorderd point contacts without any magnetic impurity². In point contacts including magnetic impurities the first measurements were presented by Yanson *et al.* and van der Post *et al.* [Yan+95; Pos+96]. Many further investigations of the Kondo effect in quantum dots made from various materials have been published [COK98; NCL00]. There are two publications on measurements of the Kondo effect in atomic contacts, which were published nearly simultaneously³ [Li+98; Mad+98]. The work of Madhavan *et al.* investigated a single-atom contacts made of a cobalt atom on a gold surface, whereas Li *et al.* reported results for cerium atoms on a silver surface.

The dI/dV curves mostly show Lorentz-like line shapes, but in atomic contacts the line shape may differ. Therefore, it is easier to model these curves with a Fano resonance [Fan61], which describes a tunneling process through two coupled states. For atomic contacts the two articles of Calvo *et al.* [Cal+09; CJU12] refine this model. The rates, energies, and couplings on which this model is based are depicted in figure 2.4. The line shape is described by:

$$dI/dV = g_0 + \frac{A}{1+q^2} \cdot \frac{(q+\epsilon)^2}{1+\epsilon^2}. \quad (2.8)$$

In this model g_0 is the conductance at $V = 0$, A the amplitude of the resonance, q the Fano factor, which describes the shape of the resonance and $\epsilon = (eV - \epsilon_0)/(k_B T_K)$ the energy of the magnetic state. There, $k_B T_K$ is the half-width of the resonance, which is related to the Kondo temperature T_K and $\epsilon_0 < k_B T_K$ describes the shift of the magnetic state with respect to the Fermi level. The physical interpretation of the parameters is described in [CJU12]. Also in the STM experiments of [Mad+98] and [Wah+07] similar models were used.

²Measurements in diffusive contacts are available since the 1980s, e.g. [YS86].

³The work of Li *et al.* was submitted first in September 1997, but was published slightly later than the work of Madhavan *et al.*, which was submitted in January 1998.

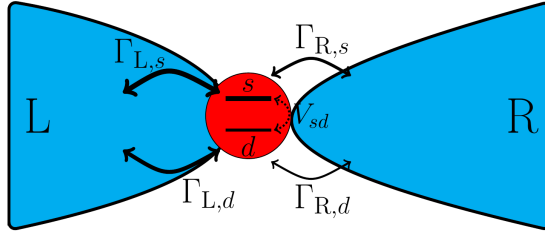


Figure 2.4: A simple model of an atomic contact to describe the Kondo effect is shown. It includes the coupling parameters $\Gamma_L > \Gamma_R$ between the atom and the electrodes and the coupling V_{sd} between the s - and the d -orbital of the atom. Adapted from [CJU12].

There are different possibilities to distinguish between a ZBA based on the Kondo effect from other ZBAs:

1. Applying a magnetic field should split the dI/dV above a certain field size. The splitting depends on the size of the magnetic field. The distance between the two peaks is $2g\mu_B B$ with g the Landé factor, B the applied field and μ_B the Bohr magneton. One only observes a splitting, if the line width of the resonance is smaller than or comparable with the splitting due to the magnetic field [Pos+96; COK98; Qua+07].
2. By varying the temperature of the sample, two observations in the dI/dV are made: First the amplitude of the resonance should decrease logarithmically and second the width should increase linearly with temperature [COK98].

Both effects are shown in figure 2.5 for a measurement of a quantum dot, performed by Croonenwett *et al.* [COK98]. Because of the high Kondo temperature of atomic contacts of ferromagnets, it is not possible to measure these effects. The magnetic energy $\mu_B B$ has to be comparable to the energy related with the Kondo temperature T_K to resolve the splitting in magnetic fields: $\mu_B B \approx k_B T_K$. Assuming $T_K \approx 100\text{K}$ [CJU12] leads to $B \approx 150\text{T}$, which is far beyond any possible static magnetic field in low temperature experiments. Resolving the effect of the temperature on the Kondo resonance requires at least $T = T_K/2$. Unfortunately, it is not possible to keep an atomic contact stable over a such big temperature range. Reasons for that are thermal fluctuations at higher temperatures and different thermal expansion for the used materials leading to modifications of the contact.

2.3 Magnetism in Atomic Contacts of Strong Paramagnets

The magnetic order in small clusters and especially in atomic contacts of strong paramagnets has been studied in recent years. Regarding the Stoner criterion, strong paramagnets

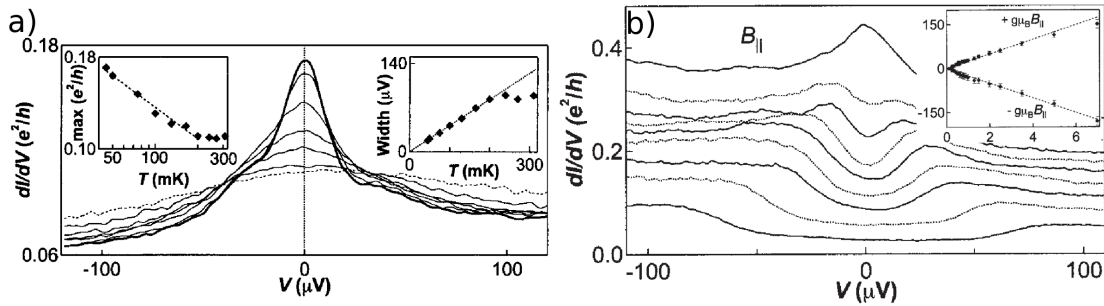


Figure 2.5: The effect of the temperature **a)** and the magnetic field **b)** on a Kondo resonance is shown. This measurement was performed on a quantum dot. The insets in **a)** show the decrease in height (left) and increase in width (right) of the resonance. The inset in **b)** shows the peak position in μV over the applied magnetic field. The splitting follows the $g\mu_B B$ line. Taken from [COK98].

are close to ferromagnetism and so one expects a magnetic order as soon as the density of states changes, connected to the dequenching of the d orbitals. For palladium a 6 % larger bond length should be sufficient [MM89]. First approaches to the magnetic order in strong paramagnets have been made by simulating respective structures with the means of DFT calculations. First simulations showed a magnetic ground state for clusters of palladium up to 13 atoms [RKD93; Zha+95; Agu+07]. Stern-Gerlach experiments with clusters with more than ten atoms do not show any resulting magnetic moment [Cox+94], however, photoelectron spectra indicated a magnetic order up to seven atoms [GE96]. Later SQUID measurements showed a hysteresis loop in bigger clusters with up to some hundred atoms [Sam+03]. Also other materials should feature a magnetic order in few-atom clusters [FF07]. Since electrical measurements on single clusters are challenging, the field started to calculate the emergence of magnetic order in atomic wires and contacts. The results of the different studies are discussed in section 2.3.1. Corresponding measurements on atomic contacts of strong paramagnets are presented in section 2.3.2. There, the focus is on iridium, since this metal was investigated during this work. Signs of Kondo resonances in these contacts are scoped in section 2.3.4, again with a focus on iridium.

2.3.1 Simulations on the Magnetic Order in Atomic Contacts and Chains

There is a large number of simulations of the magnetic order in atomic contacts and chains for strong paramagnets. The focus here is on the three metals platinum, palladium, and iridium. First simulations dealt with infinite monoatomic chains of iridium and platinum leading to a magnetic order for elongated chains [DT03; DT04a; NRK04]. Soon also other metals [DT04b], differences between straight and zig-zag chains [Gar+05; FGF07; TG10; Sah+11],

	platinum	iridium	palladium
infinite wire	0 μ_B to 0.2 μ_B [DT03; FF07; Smo+08] $\sim 1 \mu_B$ [Gar+09]	0.64 μ_B [DT03; FF07]	-
atomic contact	0.3 μ_B [TMH10]	0.2 μ_B to 0.4 μ_B [TMH10]	0.7 μ_B [DT04b; Gav+10]

Table 2.1: An overview over simulations of magnetic moments per atom: The top row gives the value for infinite atomic wires, the lower row for atomic contacts. The corresponding references are given as well.

and more refined structures have been investigated [Sme+08; Smo+08; Gav+10]. Also the direction of magnetisation, along or perpendicular to the direction defined by the connection line between the two apex atoms, was focus of a study [Smo+08]. For a long time, only the magnetic moment of the chain and apex atoms have been calculated. Later, effects on the transport properties were analyzed [Fer+05; Gar+09], as well as the magnetic anisotropy energy (MAE) [Mok+06; FGF07], which measures the pinning of the magnetic moments to their direction. Comprehensive calculations of the MAE for platinum and iridium were performed by Thiess *et al.* These calculations include different position types⁴, as well as variations of the bond lengths between the atoms in the contact caused by strain [TMH10]. The results of this paper are discussed later (see section 2.3.3). The effects of non-collinearity and spin-orbit coupling were taken into account in the theory [Kum+13b; Zha+14].

One major outcome from most of the simulations is the knowledge of the size of the magnetic moment at the equilibrium bond length. The most probable values are given in table 2.1. Especially for iridium the value changes depending on the position of the atom in the contact.

2.3.2 Experimental Evidence from Transport Measurements

First measurements of the change in resistance as a function of the magnetic field in atomic contacts of the strong paramagnet palladium showed effects up to several hundred percent [Ien+12]. Ienaga *et al.* used notched-wire break junctions with a long suspended part. They explain the large effect with magnetostriction (cf. page 15), which seems reasonable for long suspended junctions. Measurements of short suspended junctions are also published for the three strong paramagnets platinum, palladium, and iridium. The corresponding publications of Strigl *et al.* and Prestel *et al.* report the presence of a magnetic order in atomic

⁴Position type means the role of the atom inside the contact, e.g. apex or center atom.

contacts [Str+15; Str+16; Pre+19]. In all three studies the changes in the conductance were measured while changing the magnetic field continuously. The results of iridium have been obtained in the present thesis project. Therefore, the results of iridium will be discussed in more detail. For all three metals similar properties of the magneto-conductance traces have been found. These properties can be connected to indications for a local magnetic order. The five different indications for a local magnetic order are [Str+15; Str+16]:

1. The size and
2. the shape
- of the magneto-conductance (MC) and anisotropic magneto-conductance (AMC) traces are comparable to those of ferromagnetic atomic contacts.
3. MC and AMC strongly depend on the exact contact, i.e. the atomic configuration.
4. The sweep with in- and decreasing field show a hysteresis at $B = 0\text{T}$
5. and the MC traces are dependent on the history of the contact.

Strigl *et al.* introduced a qualitative model to explain the shape of the measured MC traces with $B \perp I$ [Str+15]. The model is based on considerations, comparable to those of the GMR effect. Strigl *et al.* assigned magnetic moments to each atom in the atomic chain, the two apex atoms and also each lead. Due to their spin, electrons passing through the constriction feel the changes in magnetic field arising from the magnetic moments. Applying a magnetic field will influence the orientation of the magnetic moments. The effect of this influence depends on the magnetic anisotropic energy (MAE) of each magnetic moment. As calculated by Smogunov *et al.*, the MAE depends on the position of the magnetic moment in the contact [SDT08]. Therefore, the electrodes, which are only weakly bound, will change their orientation first. The magnetic moments of the chain atoms are pinned strongest and, therefore, unaffected by the experimentally available fields. Not only the orientation of the magnetic moments changes, but, more importantly for the model, also the relative orientation between the moments changes with changing magnetic field.

Phenomenological Model

In the following, the model of Strigl *et al.* will be described in detail for the two most common cases depicted in figure 2.6. There are also explanations for the more complex cases reported in [Str+15; Str16]. In most cases, the curves are similar for positive and negative fields. Mostly, they follow the same trend for in-/decreasing field, but one also finds exceptions. The following explanations are formulated for increasing, positive field. The behavior in decreasing and negative field is accordingly.

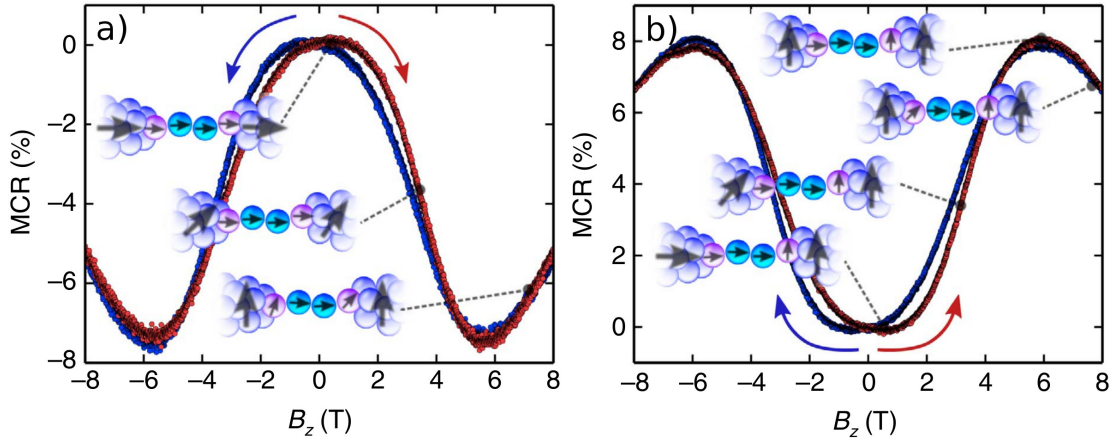


Figure 2.6: Some different orientations of the magnetic moments for the two dominating shapes of MC traces for negative **a)** and positive **b)** MCR are depicted. The model includes electrode atoms in blue, apex atoms in magenta and chain atoms in cyan. The direction of the magnetic moments is indicated by arrows, the size of which is reciprocal to the MAE of the corresponding part. Taken from [Str+15].

For a negative MCR, the curve has a maximum at $B = 0$ T. This case is depicted in the figure 2.6 a) and belongs to the collinear ground state. This means without any applied field, all magnetic moments point in the direction of the chain and, therefore, in the direction of current. With increasing field, the weakly bound magnetic moments of the electrodes start to align with the applied field. This leads to a decrease of the conductance, because the magnetic moments are misaligned leading to additional scattering events. At the local minimum in conductance, the magnetic moments of the electrodes are fully aligned with the external magnetic field. With further increasing field, the magnetic moments of the apex atoms start to change their orientation, because the respective MAE is overcome. Since the magnetic moments of the apex atoms bridge the perpendicular orientated magnetic moments of chain atoms and the electrodes, the overall transparency recovers and the conductance increases again. One does not find any further extremes, since the needed magnetic field to rotate the apex atoms fully and to begin to rotate the magnetic moments of the chain atoms is too high for the used experimental setups.

For the positive MCR, with a minimum at $B = 0$ T, a non-collinear ground state is required. As depicted in figure 2.6 b), the magnetic moments of one electrode and apex atom are pointing perpendicular to the chain axis. By increasing the field, the magnetic moment of the second electrode changes its orientation. This enhances the tunneling probability between the two leads and the conductance increases. At the finite-field extreme, the magnetic moment of the electrode is aligned with the magnetic field and the magnetic moment of the second, still collinear aligned, apex atom is changed. This results in a reduction of conductance, due to increased misalignment in the system.

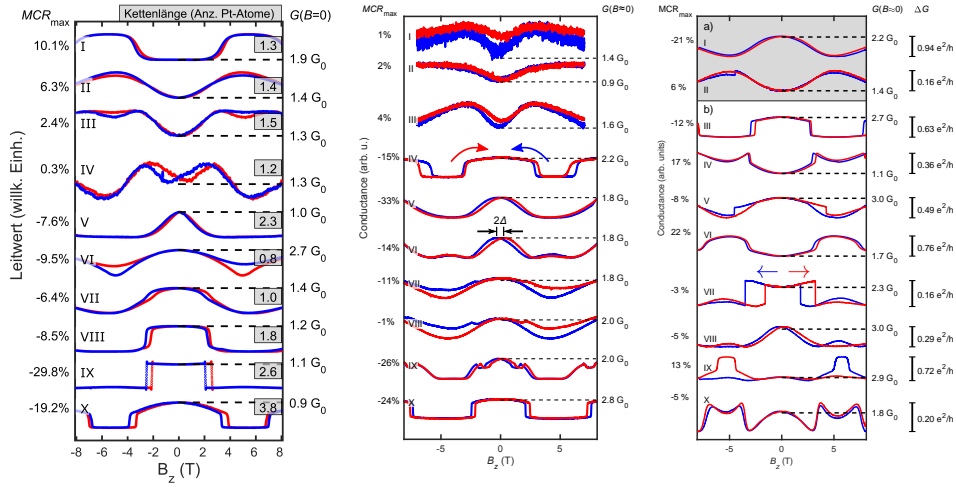
Characterization of the MC Curves

In general a large variation of shapes was found for all three metals. An overview of ten typical MC traces for each metal is given in [figure 2.7](#). A discussion about the shapes and their abundance is done in the corresponding publications [[Str+15](#); [Str+16](#); [Pre+19](#)] and will not be reproduced here. The exact shape depends on the atomic configuration and the coupling between the different parts of the junction. Considering only contacts of the three different metals, which do not change their conductance at zero field during measurement, one can compare the key features of the MC traces. This overview is given in [table 2.2](#).

Going from platinum via iridium to palladium, one sees a monotonous development in the key features of the MC traces: hysteresis, effect size, finite field extremes, and ratio of collinear to non-collinear ground states. This trend can be compared to two properties: The first one is the spin-orbit coupling (SOC), which enhances the spin-mixing and, therefore, leads to the formation of a non-collinear ground state. The second property is the Stoner parameter, which is a measure of the vicinity to ferromagnetism (cf. [section 2.2](#)). Both parameters are listed in [table 2.2](#), too. The SOC supports the trend from platinum to iridium, the Stoner enhancement does not follow this trend. But platinum and iridium form atomic chains, palladium does not. This will influence the dequenching of the orbitals in the palladium contact, due to a higher coordination of the atoms in the contact. The third parameter which should also be mentioned in this discussion, is the calculated magnetic moment μ of the contact atoms. This parameter is not shown in [table 2.2](#), since the different simulations are run with different approaches and methods. A overview over the results of these simulations is given in [table 2.1](#). Additionally, the given magnetic moments differ from chain atom to apex atom up to a factor of two and are highly dependent on the actual bond length (see [section 2.3.3](#)). The relative abundance of negative compared to positive MC traces is linked to the SOC via spin-mixing [[Str+16](#)]. This trend is well developed in the data. The MCR_{\max} values reflect the influence of the local magnetic moment on the transport. There, the SOC, which connects the spin with the external magnetic fields and the size of the magnetic moment will play an important role.

The hysteresis is probably dependent on the residual remanence in parts of the contact. Here, the electrodes with the lowest MAE play the key role. One might correlate this value to the Stoner enhancement, which is biggest in palladium. This corresponds to the fact, that a hysteresis is always present in palladium, but not always in platinum and iridium. Additionally, one would expect, that the upper limit of the hysteresis is effected by the Stoner enhancement. However, this limit of palladium does not fit to the values of the other two metals. Hence, it remains unclear if the hysteresis can be ascribed to the Stoner enhancement solely, or if other properties have to taken into account.

The finite-field extremes B_z^{ext} should be connected at first glimpse with the coercivity and, therefore, with the Stoner enhancement. However, the obtained values mirror the values of the SOC. In reduced dimensions the SOC might play a more important role. The SOC, as



(a) Platinum, from [Str16].

(b) Palladium, from [Str+16].

(c) Iridium, from [Pre+19].

Figure 2.7: An overview over the different shapes of the MC curves of the three metals platinum, palladium, and iridium: For each metal the effect size is noted on the left side and the conductance at $B = 0$ T on the right side. For platinum also the chain length in number of atoms is given and for iridium the change in conductance ΔG is given in units of e^2/h . In the panels of palladium and iridium, the sweep direction of the magnetic field is indicated by arrows. For curve VI in the palladium panel, the hysteresis is depicted.

well as all other features are strongly dependent on the exact configuration of the magnetic moments and depend strongly on the bond length and other contact properties, which are experimentally not available. Therefore, a conclusive explanation of these key features is not possible.

	platinum	iridium	palladium
MCR_{\max}	-40 % to 40 %	-73 % to 24 %	-45 % to 10 %
# neg : # pos	2:1	3.9:1	5:1
Δ	0 mT to 800 mT	0 mT to 550 mT	140 mT to 310 mT
B_z^{ext}	4 T to 7 T	4.7 T to 6.5 T	3 T to 5 T
SOC	1.09 eV	0.94 eV	0.34 eV
$\frac{1}{2}UD(E_F)$	0.57	0.27	0.775 to 0.86

Table 2.2: The key features of the MC traces for the strong paramagnets platinum, palladium, and iridium are summarized in the upper part of the table. The values are taken from [Str+15; Str16; Pre+19]. In the lower part the bulk properties SOC and the Stoner parameter are given. The SOC is taken from [And70], the Stoner parameter $\frac{1}{2}DN(E_F)$ is calculated from values given in [And70; And+77]. The second value for palladium originates from [Jan77].

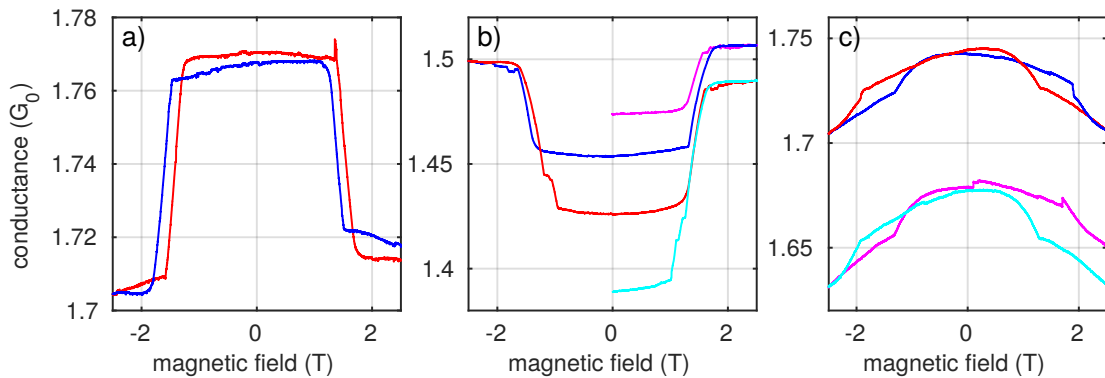


Figure 2.8: Three measurements of the behavior in parallel field on a bronze substrate are shown. The curve shown in a), reveals steep changes around 1.5 T. The staircase-like behavior is shown in b), characteristic is the ongoing change in conductance (magenta: initial curve; blue: decreasing field; red: increasing field; cyan: final curve). In c) two measurements in parallel field are depicted, one before (red/blue) and one after (magenta/cyan) applying a perpendicular field.

Parallel Field

Additionally to measurements with the magnetic field applied perpendicular to the contact and, thereby, the current direction, also measurements with the magnetic field applied parallel were performed. In the works on platinum and palladium and also in this work, the maximum experimental available field is limited to 3 T. Therefore, one is not able to fully align the magnetic moments of the electrodes. Nonetheless, there are some remarkable results found in field sweeps parallel to the contact (hereafter named *x*-sweep or B_x). For platinum and palladium only a small number of *x*-sweeps have been measured, most of them show a small variation below 1 %. The shape is mostly parabolic and shows the opposite curvature to the corresponding *z*-sweep [Str+15; Str+16]. For platinum, Strigl *et al.* investigated the shape of the *x*-sweeps as function of the magnetic history [Str+15]. They found a featureless parabolic behavior for no or only low field applied in *z*-direction prior to the *x*-sweep, but for $|B_z| > 7$ T, the *x*-sweep shows a strong hysteresis and a sweep direction dependence.

Measurements in parallel field were also carried out for iridium. One of the presented samples has already been shown by Ritter [Rit18], who performed his master thesis in the framework of this thesis. The measurements in parallel field have been limited to $|B_x| \leq 2.5$ T to avoid quenching of the superconducting magnet. The sample reported by Ritter showed an unusual behavior with steep changes in resistance for fields below 2 T. One exemplary curve is depicted in figure 2.8 a). Additionally, many curves show a continuing change in resistance leading to a staircase like behavior. The exact reason for this is not clear. An example of this behavior is depicted in figure 2.8 b). Strigl *et al.* reported rare cases of similar behavior in atomic contacts of palladium in parallel field. They attribute it to particular contact config-

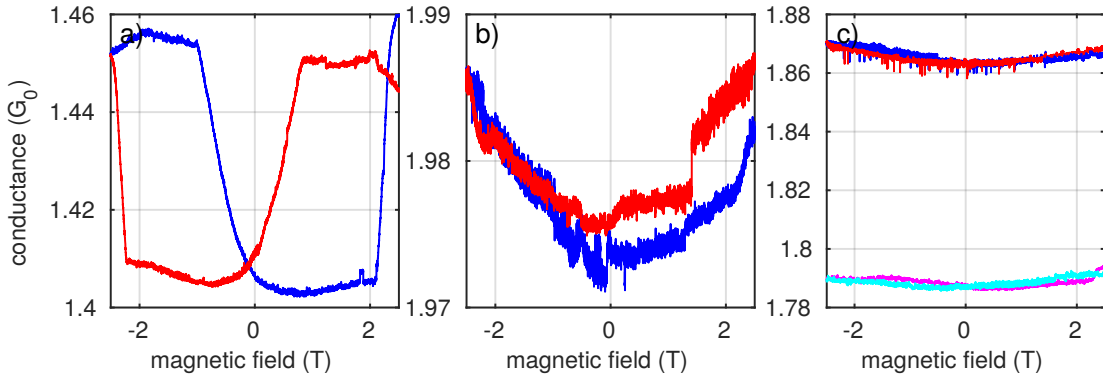


Figure 2.9: Measurements in parallel field on Kapton substrate: **a)** The hysteretic behavior, caused by the weak thermal coupling through the Kapton, disappeared after increasing the thermal coupling via exchange gas. Then **b)** a parabolic magneto-conductance is found. **c)** Both measurements in parallel field, before (red/blue) and after (magenta/cyan) applying perpendicular field, show a parabolic behavior.

urations [Str+16]. There is only one example of a contact, which did not show the staircase behavior and was stable enough to measure in parallel field before and after applying a perpendicular field. The two curves in the parallel field are shown in [figure 2.8 c](#)).

A second sample was measured to check for the staircase behavior. To investigate a possible influence of the substrate material, this sample was produced on Kapton. There, a hysteretic behavior as shown in [figure 2.9 a](#)) was found. Similar behavior was reported by Hamsch for gold on Kapton in the same dewar. He proposed a bad thermal coupling through the substrate as a possible cause of the hysteresis and, therefore, suggested to improve the thermal coupling via exchange gas [Ham18]. After adding a lot of exchange gas, the hysteresis disappeared and a parabolic shape of the conductance with respect to the magnetic field was found. One typical curve is shown in [figure 2.9 b](#)). The effect size is below 4 % for all measured contacts. The influence of a perpendicular field on the shape was tested for this sample as well. The corresponding curves are depicted in [figure 2.9 c](#)). For iridium no clear changes in shape were found. This is in contrast to the findings in platinum, reported by Strigl *et al.* [[Str+15](#)].

Anisotropic Magneto Conductance (AMC)

A third transport measurement type with changing the magnetic field is the anisotropic magneto-conductance. In these measurements, the absolute value of the magnetic field is kept constant, but the angle θ between the current direction and the magnetic field is changed. For $\theta = 0^\circ$ the magnetic field is parallel to the current direction. The conductance may go

up or down and has an amplitude of 4 % to 6 % for platinum [Str+15] and up to 10 % for palladium [Str+16]. The reported shape is roughly $\sim \cos^2\theta$, but shows significant deviations. These deviations from the perfect $\cos^2\theta$ shape were also found by Bolotin *et al.* in permalloy contacts. Additionally, these deviations seem to be voltage dependent [BKR06]. For atomic contacts of nickel, Viret *et al.* also reported deviations from the $\cos^2\theta$ -form [Vir+06]. Häfner *et al.* proposed, on the bases of simulations, that these deviations are created by the reduced dimensions of the contact [HVC09].

For iridium, Ritter [Rit18] measured the AMC on bronze substrate. There, one finds an amplitude of over 10 % with a minimum or a maximum at $\theta = 0^\circ$. One example of such a curve with a minimum at 0° and an amplitude of about 10 % is shown in [figure 2.10 a\)](#). For comparison also a $\cos^2\theta$ fit is displayed. The deviations from a pure $\cos^2\theta$ behavior are negligible and consist mostly in a steep increase around $1.75 G_0$. Stretching an atomic contact and measuring the AMC for different elongations of the contact leads to a transition from a curve with a minimum to a maximum at $\theta = 0^\circ$. This curve is shown in [figure 2.10 b\)](#). The intermediate state does not show a clear $\cos^2\theta$ behavior, but features a local minimum at $\theta = 0^\circ$ and a more pronounced minimum at $\theta = 90^\circ$. Hence, an influence of the stretching on the exact configuration of the atomic contacts is expected. Due to the lack of successful stretching experiments, an interpretation is complicated. For the measurements with perpendicular field, stretching experiments have been performed. These measurements are discussed in [section 2.3.3](#).

The bronze substrate of these measurements might have a small intrinsic magnetism, which could influence the measured signal. Therefore, some control measurements on Kapton have been carried out. The results are presented in the following.

The measurements on the Kapton substrate are significantly more challenging, since the contacts seem not to be as stable as on the bronze substrate. Hence, only a few contacts were stable enough to record an AMC over a whole circle sweep. The starting point is $\theta = 0^\circ$, where the magnetic field is parallel to the constriction and, therefore, parallel to the current direction. Then the direction of the magnetic field is changed in a continuous way. Two recorded traces are depicted in [figure 2.11](#). The two curves show a $\cos^2\theta$ behavior with minor deviations at the extremes at 90° and 270° . The effect size for this sample is smaller than that for iridium on bronze. The maximum amplitude is around 3 %. An explanation for this deviation cannot be given, but the effect size is always dependent on the exact atomic configuration and thus, variations are expected. Given the small number of stable contacts for iridium on Kapton, it is statistically probable that higher amplitudes were not measured.

Also a stretching experiment, as explained in [section 2.3.3](#) and performed on bronze, was tried. Unfortunately, mainly unstable contacts have been measured for this sample. Only one sequence was stable over more than two stretches. This one sequence is depicted in [figure 2.12](#). For the four measured contacts, the conductance changes from $2.18 G_0$ to $1.87 G_0$,

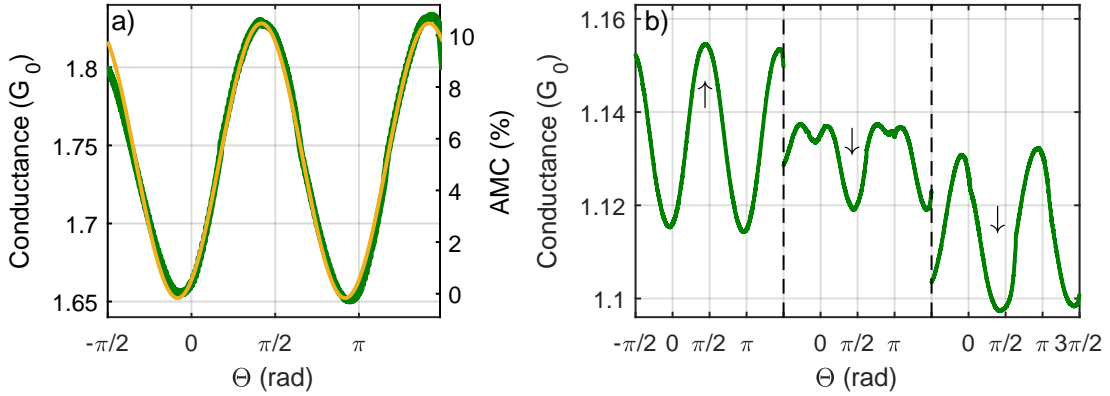


Figure 2.10: AMC measurements of iridium atomic contacts on bronze substrate: In **a)** one AMC curve with a distinct minimum at 0° (green) is shown. This curve is fitted with a $\cos^2 \theta$ function (yellow). In **b)** a stretching experiment on the same sample is depicted. The measurements shows a transition from a minimum at 0° to a maximum. The intermediate state looks like a superimposed curve with minima at 0° and 90° . Reproduced from [Rit18].

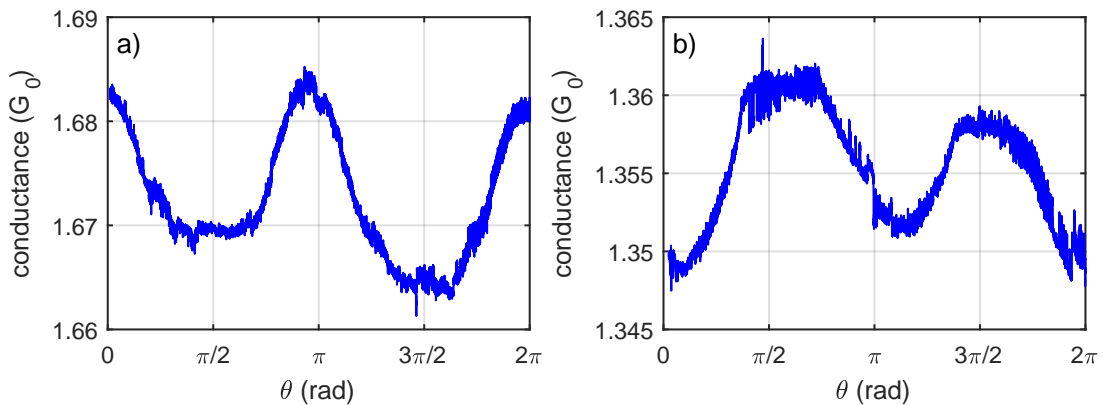


Figure 2.11: Two AMC measurements showing a $\sim \cos^2 \theta$ behavior, with slight deviations, are depicted. The effect has a size $\sim 1\%$ for both curves, but a different direction: The curve in **a)** has a maximum at $\theta = 0^\circ$ and the curve in **b)** shows a minimum at $\theta = 0^\circ$.

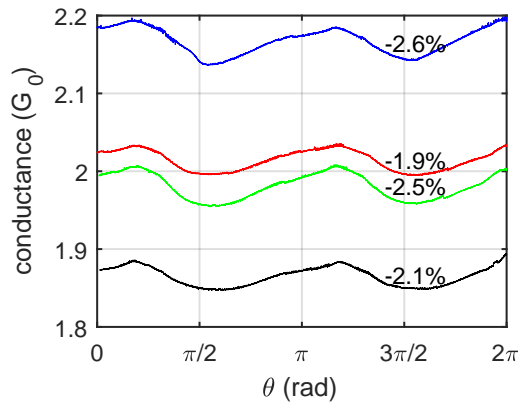


Figure 2.12: A stretching attempt of an atomic iridium contact: The overall shape of the AMC signal does not change, only the conductance reduces from blue, over red and green to black. The amplitude varies as well as the exact shape of the minima and maxima.

but the shape does not change. This is in contrast to the change in shape of the AMC for iridium on bronze. Even though there is no transition from a minimum to a maximum at $\theta = 0^\circ$, minor changes and deviations are present. The effect size changes only by about 0.5 %. Other measurements, which were not stable beyond the first stretch, showed an onset of a transition similar to the one found for iridium on a bronze substrate.

One can conclude that the measurements on Kapton support the measurements on bronze, but with smaller effect size. Nonetheless, the whole range of different shapes is recorded, as well as a first hint for a dependence on the stretching. Thus, a solely substrate driven effect can be excluded.

Histograms with Magnetic Field

One last approach to check the influence of the magnetic field on the conductance is measuring histograms with and without magnetic field. In figure 2.13, three histograms are shown. Two (blue/green) without and one (red) with an applied field of 8 T. To verify that the sample did not change, one histogram was performed before (blue) and one after (green) the measurement with field. These two histograms do not show major changes. Smaller deviations are expectable, since the break junction technique does not allow to have a high number of opening curves in histograms and, therefore, single events can have a notable influence. Also there are no significant deviation between the histogram with and without magnetic field. There are two possibilities, either the applied field is not appropriate for seeing any effect, or the method of a statistical measurement is not sensitive to changes caused by magnetic field.

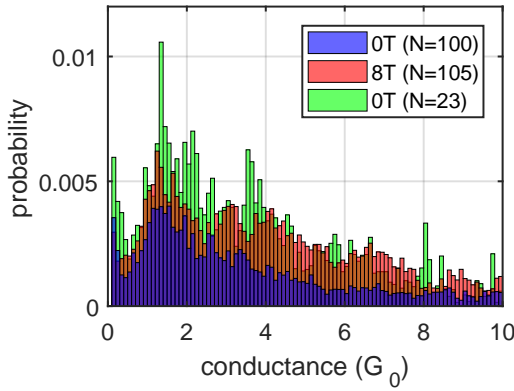


Figure 2.13: Histograms of iridium with (red) and without (blue/green) applied magnetic field of 8 T: The blue data was taken before and the green data after the red histogram. The number of opening traces the histogram consists of is given in the top right corner.

2.3.3 Stretching of Atomic Contacts

As indicated earlier, the magnetic order depends, among others, on the distance between the single atoms. For strong paramagnets this behavior was investigated by Delin and Tosatti for $5d$ metals [DT03]. Their calculations showed the dependence of the magnetic moment per atom from the bond length in infinite mono-atomic chains of osmium, platinum, and iridium. A realistic model was calculated by Thiess *et al.* for platinum and iridium [TMH10]. They investigated a trimer, consisting of one central and two apex atoms, between two electrodes and calculated for both atoms the magnetic moment and the MAE upon stretching the whole model up to $3 a_0$ ⁵. The distances electrode – apex atom and the distance apex atom – chain atom behave differently upon elongation of the contact. Because of the difference in binding forces, the distance electrode – apex atom do not change significantly in contrast to the distance apex atom – chain atom, which increases proportional to the elongation of the contact. This leads to a different evolution of the magnetic moment and the MAE for apex and chain atoms. The spin magnetic moment increases for both, apex atoms and chain atoms, with stretching. More interesting is the development of the MAE. For iridium the MAE of the apex atom undergoes a sign change around an elongation of $1 a_0$ and further stretching leads to sign change of the MAE of the chain atom for $\Delta L > 3 a_0$. At least the first sign change should be experimentally available. The second sign change at a stretching of more than $3 a_0$ is at the edge of stable contacts. So probably it is energetically more favorable to add another atom to the chain, than to sustain this high strain. For platinum the behavior is not so clear, nonetheless, the MAEs undergo a sign change for $\Delta L < 1 a_0$ as well.

These sign changes should allow to observe the change from collinear to non-collinear be-

⁵Thiess *et al.* calculate the length in multiple of the Bohr radius $a_0 = 0.53 \text{ \AA}$, which is often denoted as a.u.

havior or vice versa. Strigl *et al.* measured MC traces at multiple positions while stretching a platinum contact from a single atom between the electrodes to a chain with two atoms [Str+15]. They found multiple shapes and the MCR_{\max} as well as the hysteresis Δ varies between each measurement. In platinum, they do not find a particular correlation between the strain or, respectively, the bond length and the MCR_{\max} value of the corresponding curve. The favorable ground state of a relaxed chain of platinum is, because of the small MAE, unclear. Hence, both configurations, collinear and non-collinear, are possible for an undisturbed chain and, therefore, might develop differently during elongation.

The MAE for a relaxed chain of iridium is clearly negative. A change from collinear (negative MC) to non-collinear (positive MC) ground-state is expected for increasing stress in the contact. The stretching of atomic chains of iridium has been measured in the course of this work in collaboratoin with Ritter [Rit18]. One exemplary trace has already been published in [Pre+19]. Nonetheless, the main arguments are reproduced here, and the mechanism is explained for the opening trace depicted in [figure 2.14](#).

Before a stretching experiment is performed, the sample is closed completely and opened until the single-atom contact regime is entered. Then the motor is stopped and a MC trace is recorded. Afterwards the contact is stretched repeatedly for about $0.5 a_0$ and further MC traces are recorded, while the motor is stopped. This procedure is repeated until the contact breaks into tunneling. In [figure 2.14 b\)](#) the whole opening curve is depicted. The plateaus are separated by more or less abrupt changes in conductance. These abrupt changes are interpreted as mechanical changes in the contact/chain, i.e. a rearrangement of the contact leading to an additional atom in the atomic chain. After such a rearrangement, the contact is assumed to be in equilibrium bond length and, therefore, in a collinear ground state. Hence, the elongation of the contact, without major conductance changes, so called conductance plateaus, leads to a transition from collinear to non-collinear ground state of the magnetic moments. This measurement shows four plateaus, three of which show a transition in magneto-conductance.

The most prominent transition is depicted in the green box. The initial MC trace (XIX) shows a clear negative magneto-conductance, corresponding to a collinear ground state, because a rearrangement happened just before. Trace XX is recorded after an elongation of $0.8 a_0$ and shows still a negative MC, hence a collinear ground state. The third trace (XXI) is recorded after a further elongation of $0.3 a_0$. So, the total elongation of the contact is now at $1.1 a_0$. This elongation is in the regime where Thiess *et al.* predicted a change in the MAE for the apex atoms. Indeed, one finds a MC trace which shows neither negative nor positive magneto-conductance, which could be interpreted as a ground state being neither collinear nor non-collinear. A further stretching of $0.4 a_0$ leads to clear positive MC trace (XXII), which is connected to a non-collinear ground state. For an elongation of $1.5 a_0$, which has been performed in the discussed measurement after entering the plateau, Thiess *et al.* calculated MAE with different signs for apex and center atoms. Thus, we expect a non-collinear ground state,

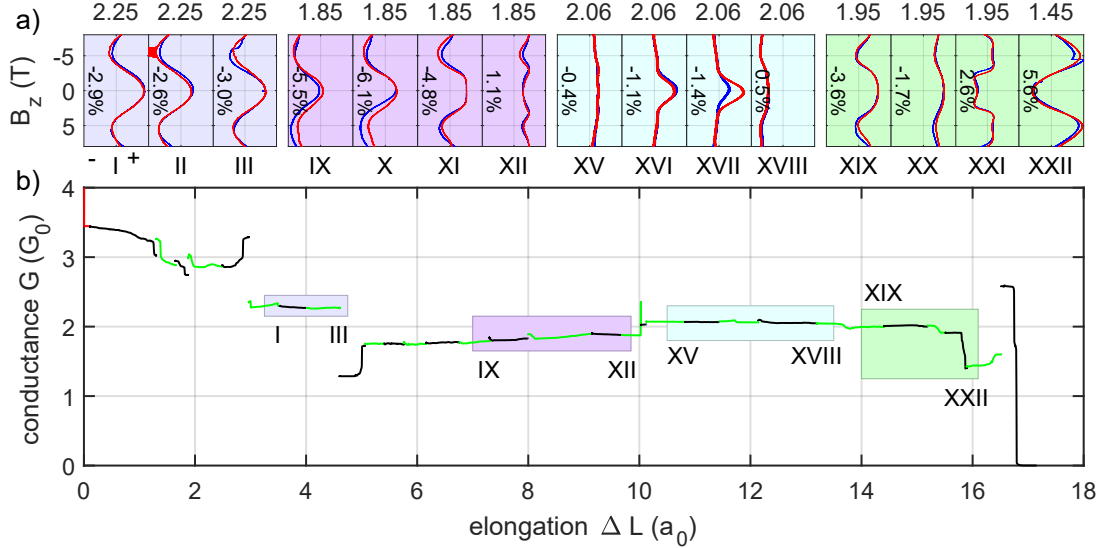


Figure 2.14: Stretching of an atomic contact of iridium: In a) multiple MC traces are depicted. For each curve the effect size is given in % inside of the panel. On top of each panel the middle conductance of this panel is given in G_0 . The roman numbering of the curves and the background color corresponds to them in the opening trace, depicted in b). There the initial opening curve is shown in red, for better distinction of the single stretches they are plotted alternating in black and green.

as we found. This elongation is still well below the equilibrium bond length of atoms in an atomic chains of iridium, calculated to be $4.2 a_0$ to $4.5 a_0$. Nonetheless, the chain changes rapidly in conductance after the last MC trace and does not form a stable plateau anymore. The rearrangement of the chain after only $\sim 2 a_0$ is exceptional, most other stretching experiments resulted in configurations, which did not show any rearrangement below about $4.0 a_0$. Two of these curves are highlighted by the purple and the cyan boxes, showing an elongation of $4 a_0$ and $3.5 a_0$ respectively. The stability of an atomic chain decreases with increasing chain length [Thi+08]. Hence, a possible explanation for the unexpected rearrangement after only $2 a_0$ at the end of the green box is the mechanical distortion introduced by a helium transfer, between two MC curves.

2.3.4 Kondo effect in Strong Paramagnets

The model for Kondo resonances by Calvo *et al.* (see also equation (2.8)) was also applied to atomic contacts of palladium [Kel15; Str16; Str+16] and iridium [Rit18]. Here, I will briefly describe the results on palladium, the results on iridium are described in more detail later. Palladium exhibits a magnetic order (see section 2.3.2 and [Str+16]), which should influence the transport characteristics. Indeed Strigl *et al.* found a number of contacts showing a dis-

tinct ZBA. By fitting the model of [CJU12] (cf. equation (2.8)), Strigl *et al.* found a distribution of Kondo temperatures with two maxima. One pronounced maximum was found at about 30 K and one at higher temperatures around 160 K. The experimental restriction of Strigl *et al.*, prevent the measurement of a splitting in magnetic field or the expected temperature dependence. Strigl *et al.* compared their deduced properties with the properties reported by Calvo *et al.* for the iso-electric nickel [CJU12]. This comparison supports the assumption of a magnetic Kondo state in atomic contacts of palladium. The small Kondo temperature of 30 K is contradicting the calculations of Romero *et al.* [Rom+09]. They calculate a Kondo temperature of 212 K for a contact of a single palladium atom between two pyramidal leads made of palladium. These calculations are supported by measurements of Islam *et al.*, who also measured ZBAs interpreted as Kondo effect [Isl+17]. Their distribution of Kondo temperatures has a maximum at around 160 K. Islam *et al.* suggest local disorder, leading to two-level fluctuations (TLF), as a possible reason for the low Kondo temperature measured by Strigl *et al.* The phenomenon of TLF driven ZBAs has been reported earlier by [RB92; KSK85]. The high Kondo temperature, reported by Islam *et al.*, would match the second peak Strigl *et al.* reported.

For atomic contacts made of iridium, Ritter also reported ZBAs [Rit18], which were fitted with the model of Calvo *et al.* The analysis of 260 contacts yields a log-normal distribution, which is expected for the Kondo temperature, with a maximum at 26^{+18}_{-9} K. The data and a fit with a log-normal distribution are shown in figure 2.15 b). For some of these contacts, also the dependence of the dI/dV on magnetic field and temperature was measured. Due to limitations of the setup it was only possible to see effects on contacts with low Kondo temperature. There, the typical decrease in feature size with increasing temperature was found. Ralph and Buhrman also found a logarithmic dependence of the conductance with temperature [RB92]. Therefore, this is no proof for magnetic impurities. Thus, one has to investigate the magnetic field dependence of the resonance. The measurements of Ritter in magnetic field do not show a splitting of the resonance. Most investigated contacts have a Kondo temperature of > 26 K, which corresponds to a field of roughly 30 T for splitting. Such a large magnetic field was not available, so it remains unclear, whether or not there is a magnetic origin of the resonances. However, for one contact it was possible to measure a broadening of a resonance between 3.5 T and 7.5 T. The 3.5 T trace reveals a Kondo temperature of 14 K. Taking into account that this curve might be already magnetically broadened, it is a first hint for a magnetic Kondo resonance.

Ritter does not report any second peak in his distribution, which may have two reasons. The first is simply the low number of analyzed contacts, the second reason are additional features Ritter found in the dI/dV traces, which he interprets as conductance fluctuations. These additional features may superimpose with a Kondo resonance with a higher Kondo temperature and, therefore, the detectability of these resonances is not straight forward (three examples for superposition are given in figure 2.16 c)). To verify the absence of a second peak in the

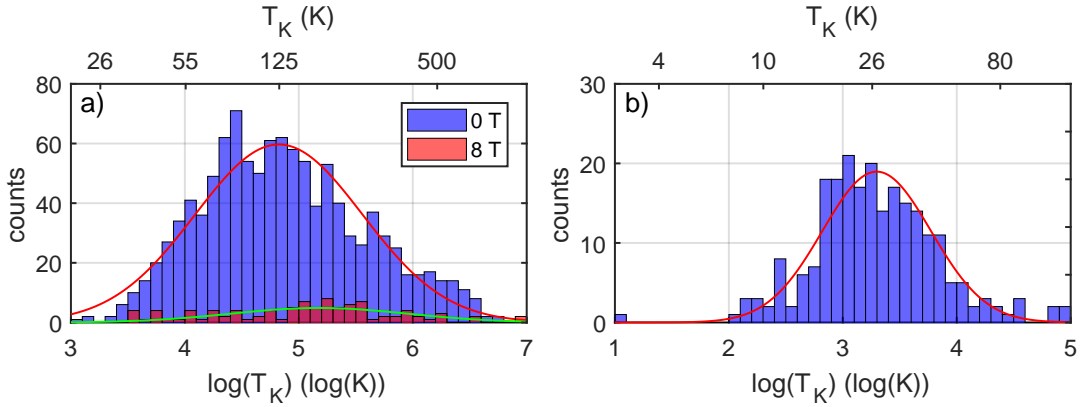


Figure 2.15: The two different distributions of the logarithm of the Kondo temperature are depicted together with a log-normal distribution. The distributions of the reanalyzed data shown in **a)** without magnetic field, in blue, has a maximum at 125^{+135}_{-65} K and with a magnetic field of 8 T, in red, has a shallow maximum at 178^{+208}_{-96} K. The original analysis from Ritter shown in **b)** has a maximum around 26^{+18}_{-9} K. The data in **b)** was taken from [Rit18].

distribution of the Kondo temperature, the contacts measured by Ritter were analyzed again together with additional dI/dV traces measured in the same setup for contacts on Kapton substrates.

This second analysis of the data was focused on ZBAs which are at least 20 mV wide, to avoid fitting small features which might result from conductance fluctuations. The distribution of the Kondo temperatures is displayed in figure 2.15 a). One expects a log-normal distribution of the Kondo temperature. Therefore, the data is also presented in a logarithmic scale. A fitted normal distribution indicates a maximum at around 125^{+135}_{-65} K, which is significantly higher than the value of 26^{+18}_{-9} K reported by Ritter. The uncertainties are given by the variance of the normal distribution fitted to the data.

One possible explanation for this big difference of the Kondo temperatures is the interval of fitting the dI/dVs . In the reanalyzed data all data, with a half-width below 10 mV have been neglected. Nonetheless, many of the dI/dV curves showed an oscillatory behavior with a small half-width. These features were often not centered around zero volt and did not merge smoothly into the rest of the dI/dV . Additionally, measurements with slow opening of the contact, as suggested by Islam *et al.*, have been performed. These measurements did not show significant differences to the distribution depicted in figure 2.15 a). But do not feature sharp resonances, which would lead to a Kondo temperature around 26 K. Unfortunately, the number of successful fits is low. Therefore, these data points are not shown.

The influence of a static magnetic field of 8 T on the distribution of the Kondo temperatures was investigated as well. The number of successful fits is low, too. The distribution is depicted in figure 2.15 a) and shows a maximum at 178^{+208}_{-96} K, which is higher than the value obtained without any magnetic field. Nonetheless, the statistical significance of this value is low, so no

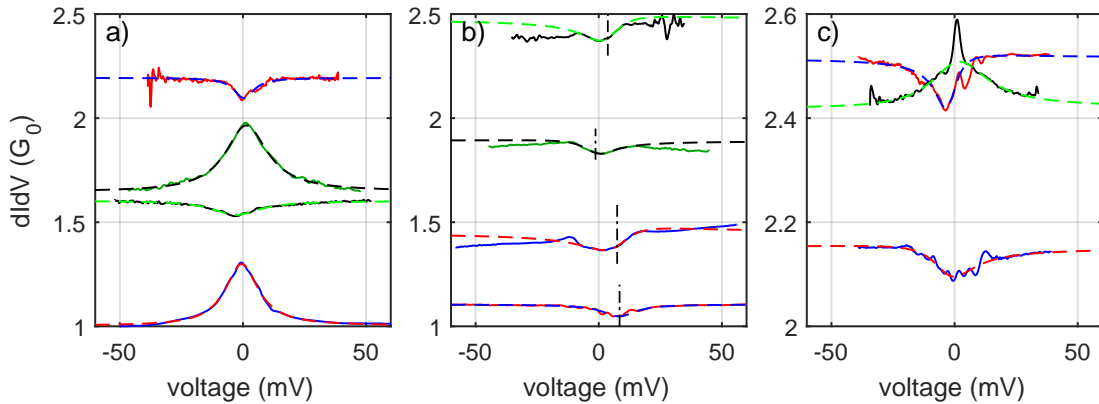


Figure 2.16: Different Kondo like ZBAs and the corresponding fits (as dotted line) are depicted: In **a)** four ZBAs which nicely blend into the rest of the dI/dV . In **b)** four curves where the center of the resonance is offset, indicated by the dashed-dotted line, are shown. The upper three curves do not blend into the rest of the dI/dV nicely. The curves in **c)** show superposition with smaller ZBAs, which influences the detectability and the fitting procedure.

further discussion is performed.

Nonetheless, I want to summarize the differences between the analysis performed by Ritter and the new analysis presented here. Ritter mainly analyzed contacts with small feature sizes: the half-width of the resonance of most of the presented curves is below 5 mV. These curves are often superimposed with a second, broad resonance. Additionally, Ritter excluded all contacts showing oscillatory behavior at low bias.

In the new analysis presented here, the focus was on broader resonances with a half-width of at least 10 mV. Also resonances with small oscillatory behavior at low bias have not been excluded, if a broad resonance was superimposed. In this case the broad resonance was fitted, as indicated in [figure 2.16 c\)](#), especially the blue and the red curve. For superpositions of two resonances, only the large one was fitted, leading to higher Kondo temperatures (cf. black curve in [figure 2.16 c\)](#)).

Hence, both analyses are valid, but result in different Kondo temperatures. For palladium Strigl *et al.* found two maxima in the distribution of the Kondo temperature as well [Str+16]. One possible explanation was given by Islam *et al.* [[Isl+17](#)]. They attribute the lower maximum to Kondo resonances driven by two level fluctuations and the maximum with the higher Kondo temperature to Kondo resonances based on magnetic phenomena.

Chapter 3

Shot Noise

This chapter deals with the measurement and the channel analysis through noise measurements. This method is handy, since one does not need highly specialized samples with different materials or preparation techniques. On the other hand the experimental setup and the suppression of unwanted noise contributions is quite challenging. Additionally, one has to consider the effects of parasitic capacitances. This chapter is organized as follows: The first section, [section 3.1](#), introduces the concepts of (shot) noise and the influence of magnetism on the noise of a mesoscopic contact. In [section 3.2](#) a short summary of the sample preparation is given, followed by a description of the setup ([section 3.3](#)) and the data processing ([section 3.4](#)). The results are discussed in [section 3.5](#) and a conclusion is drawn in [section 3.6](#).

3.1 Theoretical Background

There are different sources of electronic noise. Here, I will focus on shot noise, for a detailed description of all different noise contributions I would like to refer to textbooks like [[BS71](#); [Kog96](#); [Mül90](#)].

The transport of electrons through a conductor is described by the current $I(t)$. Its fluctuation around the mean value $\langle I(t) \rangle$ is $\Delta I = I(t) - \langle I(t) \rangle$. Generally, one has to distinguish between the time average $\langle I(t) \rangle$ and the ensemble average $\langle I \rangle$. For all cases considered in this work these are the same: $\langle I \rangle = \langle I(t) \rangle$.

Per definition $\langle \Delta I \rangle = 0$, so, to get information from the noise, one analyses the mean of the square $\langle \Delta I(t)^2 \rangle$. Normally, one is not interested in the time dependence of the shot noise, but in the spectral noise density $S(f)$ which is calculated with the Fourier transform of the

auto-correlation:

$$S(f) = \int_{-\infty}^{\infty} \exp(2\pi i f \tau) \langle \Delta I(t + \tau) \Delta I(\tau) \rangle d\tau \quad (3.1)$$

A typical spectral noise density has sections with different frequency dependence. For $f = 0\text{Hz}$ one expects a delta peak due to the DC part of the current, followed by a $1/f$ section, which then develops into a section with constant energy per bandwidth: the white noise. At high frequencies the noise then reduces to zero, since the total noise power may not diverge. The reasons for the $1/f$ -noise contribution are manifold [Mil02] and will not be discussed here. The $1/f$ -noise has been analyzed for atomic contacts in the article by Mu *et al.* [Mu+19], which will be discussed later (see [page 39](#)). Here, I will focus on the thermal noise and the classical shot noise.

Thermal Noise

Due to the Brownian motion of the electrons inside a resistor, a frequency independent noise contribution, namely the thermal noise, is generated. The spectral noise density is given by

$$S_i(f) = 4k_B T G . \quad (3.2)$$

There $k_B = 1.38 \times 10^{-23}\text{J/K}$ is the Boltzmann constant, T the temperature and $G = 1/R$ the conductance of the resistor. This relation might be deduced by an RC model or the Drude model. For both derivations I refer the reader to textbooks like [BS71; Kog96; Mül90].

Shot Noise

A classical current is built up from many individual electrons with a discrete charge of the size of the elementary charge $e = 1.602 \times 10^{-19}\text{C}$. If the electrons have to overcome a potential barrier, this quantization of charge will lead to an additional noise. Which was first discovered by Schottky in vacuum tubes [Sch19]. For frequencies well below the recombination time¹ τ ($f \ll (2\pi\tau)^{-1}$), the spectral noise density is proportional to the average current $\langle I \rangle$:

$$S_i(f) = 2e \langle I \rangle \quad (3.3)$$

If one assumes uncorrelated electrons, the shot noise is described by the Poisson statistics [Kog96; BB00].

¹The term recombination time describes the time one charge carrier needs to pass through the potential barriers in devices like vacuum tube or diode.

3.1.1 Shot Noise in Atomic Contacts

In atomic contacts one has to drop the assumption of uncorrelated electrons. There are many different review articles [BB00; AYR03; Req+16] and even books [CS10], which summarize the research in that field. Here I will only give a brief overview over the different subfields, which are connected with the measurements presented in this work.

The two main arguments for correlated electrons are the Coulomb repulsion and the Pauli principle. In atomic contacts the transport is based on quantum mechanical principles and, therefore, the transmission and reflection probabilities are essential. On the bases of the Landauer approach, one may calculate the spectral noise density of a mesoscopic conductor [BB00]. Therefore, one has to evaluate the transmission and reflection for each transport channel separately. The Landauer approach leads to

$$S_I(V) = 2eVG_0 \coth\left(\frac{eV}{2k_B T}\right) \sum_{i=1}^N \tau_i(1-\tau_i) + 4k_B T G_0 \sum_{i=1}^N \tau_i^2 \quad (3.4)$$

when temperature effects are included. For contacts dominated by a few channels with $\tau_i \neq \{0, 1\}$ this noise is reduced compared to full shot noise discovered by Schottky. The first experimental evidence of a reduction of the excess noise was presented by van den Brom and van Ruitenbeek [BR99]. They measured the noise of atomic sized gold contacts and found a reduction of the excess noise at multiple integers of G_0 (see also [figure 3.1](#)). For gold, they showed the existence of a minimal excess noise, which can be explained by single-channel transport. For contacts with a higher excess noise they deduced a model with one major channel and a second contributing channel, which carries up to 20 % of the current. The resulting excess noise is also displayed in [figure 3.1](#) as dashed lines.

Since a full fit to [equation \(3.4\)](#) is complex and only possible for up to two channels (see below), one normally introduces the so called Fano factor

$$F = \frac{\sum_{i=1}^N \tau_i(1-\tau_i)}{\sum_{i=1}^N \tau_i}. \quad (3.5)$$

This Fano factor is a measure for the reduction of the shot noise compared to the full shot noise, since for $2k_B T \ll eV$, $S_I = 2e\langle I \rangle F$ [Kum+12]. For ballistic contacts with a few participating channels, one gets $F \leq 1$ [CS10]. For a high number of channels involved in the current transport, the Fano factor converges to $F \rightarrow 1/3$ [Che+15; Lum+18].

To get experimental access to the Fano factor, one defines reduced parameters X and Y ,

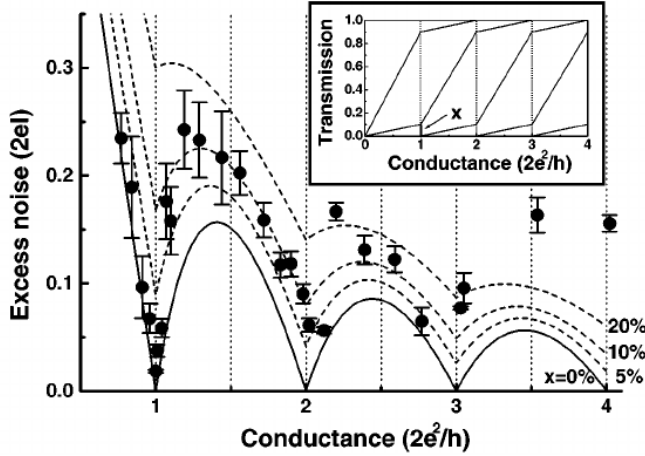


Figure 3.1: The dependence of the minimal excess noise as a function of the conductance for a single transmitting channel is shown as full line. If one assumes one additional channel with a fixed contribution, the broken lines can be calculated. The data points are recorded at contacts made of gold, which follow the full line for a single channel. Taken from [BR99].

which are normalized to the thermal noise of the sample:

$$X(V) = \frac{eV}{2k_B T} \coth\left(\frac{eV}{2k_B T}\right) \quad (3.6)$$

$$Y(V) = \frac{S_I(V) - S_I(0)}{S_I(0)} \quad (3.7)$$

The Fano factor is then available as $Y = (X - 1) \cdot F$, which is a linear regression and therefore simplifies the data analysis.

A full analysis of equation (3.4) may reveal the exact transmission of the different contributing channels, which is called the channel configuration $\{\tau_i\}$. To determine an exact solution for $\{\tau_i\}$ one needs as many independent measurable quantities as the number of channels. Since one only has two independent quantities, the conductance G and, as a result of current noise S_I , the Fano factor F the maximum number of channels reduces to two.

For more than two channels the system of equations is underdetermined. Hence, multiple possibilities of channel configurations are possible. To extract the most probable channel configuration Vardimon *et al.* established a statistical analysis [VKT13]. Assuming a set of transmission probabilities $\{\tau_i\}$, which are ordered in transmission. A finite precision $\Delta\tau$ in transmission τ results in a limited number of different sets $\{\tau_i\}$. By calculating all possible sets $\{\tau_i\}$ and comparing F and G of these sets with the experimental obtained values including a variation of ΔF and ΔG leads to the most probable set of transmission probabilities. This procedure gives a range for each channel transmission and it is possible to estimate the channel configuration also for contacts with more than two channels.

Influences to the Shot Noise

In this paragraph I want to discuss properties of the shot noise in atomic contacts, which are present in many results in this work but not main subject of interest. Since they are not always discussed separately at the place they are shown, I will give a quick overview and the corresponding literature. As already mentioned at the beginning of this section many of the effect are also covered in reviews like [BB00; CS10].

If one assumes additional current paths, which open at certain energies, this might lead to a change in shot noise. One possible and the most prominent example for a change in transport is phonon mediated transport [CS10]. One easy way of detecting the corresponding energy is inelastic electron tunneling spectroscopy (IETS) [Ree08]. In 2012 Kumar *et al.* observed a kink in the shot noise of gold atomic contacts as a function of voltage [Kum+12]. They found a correlation between the voltage at which the kink occurred and the energies determined by IETS. They presented a model for interpreting the change in the slope. A larger slope results in a positive change in the Fano factor F , a smaller slope in negative change in F . They found positive changes above $0.95 G_0$ and negative changes below. Similar results are reported by Bahouosh *et al.* for both atomic and molecular junctions from theoretical and experimental side [Bah+19].

Measuring the noise at higher voltages reveals additional features, attributed to interaction with phonons, like presented by Tewari *et al.* for Pt-D₂-Pt junctions [TSR19]. They claim that the phonons activate two-level fluctuators (TLF), which can be identified in the third derivative of the noise ($d^3 S_I / dV^3$). Tewari *et al.* found a peak in the third derivative of the noise, which position they interpret as the energies of the corresponding TLF.

A recent study by Mu *et al.* investigates the behavior of the shot noise at high voltages up to some hundred mV [Mu+19]. Their theoretical calculations even go to several volts. They figured out, that due to voltage dependent transport channels, the shot noise deviates continuously from the usual linear behavior. Both positive and negative deviations seem to be possible. Their model includes two assumptions, first a change of the transmission function with applied voltage and second an asymmetric voltage drop over the constriction. For the modeling, they need to fit the differential conductance dI/dV . With this fit, they are able to reproduce the different noise data quite well, but their model only works for the case of one dominating transport channel and a second channel with minor contribution to the transport.

Also pointed out by Mu *et al.* [Mu+19] and especially in the accompanying supplementary information, there is $1/f$ -noise, which rises with increasing voltage. As already pointed out, the origin of the $1/f$ -noise might be manifold [Mil02], and also Mu *et al.* give no explanation for the source of the additional noise in their measurements. Nonetheless, they estimate the influence of that noise on their measurement results. To this end, they fit the noise with an

power function $S(f) = S_c/f^\alpha$ with a constant S_c and the exponent α . For their samples and different voltages they find a value of $\alpha = 1.5$ to 1.7 , which differs from the expected value of 2 for classical $1/f$ -noise². Unfortunately, they do not give any reason for that reduced exponent. Their estimations lead to an effect of 10% at a voltage of 240 mV , but this value is highly dependent on geometry of the single contact.

Shot Noise due to Temperature Difference

Up to now, we assumed a negligible temperature difference across the constriction. Lifting this condition, there might also be an influence on the shot noise. First investigations from theory and experiment have been reported by Lumbroso *et al.* [Lum+18]. They derived a formula for the current noise as function of the temperature difference. In this formula the noise is proportional to the square of temperature difference:

$$S_I(V=0, \Delta T \neq 0) \approx 4k_B \bar{T} G_0 \sum_i \tau_i + \frac{k_B (\Delta T)^2}{\bar{T}} \left(\frac{\pi^2}{9} - \frac{2}{3} \right) G_0 \sum_i \tau_i (1 - \tau_i). \quad (3.8)$$

Here $\bar{T} = \frac{1}{2}(T_h + T_c)$ is the average temperature and $\Delta T = T_h - T_c$ the temperature difference between the hot part (T_h) and the cold part (T_c). This additional noise contribution can be understood by considering the Fermi distribution on both sides of the junction as depicted in figure 3.2. As there are occupied (unoccupied) states on the hot side, the electrons may pass to the cold (hot) side of the junction. The transmission probabilities restrict this current to the already known factor $\sum_i \tau_i (1 - \tau_i)$. It is also worth mentioning some of the assumptions [Lum+18] made. To derive equation (3.8) one has to assume that the transmission is energy independent at the Fermi energy $\frac{\partial \tau}{\partial \epsilon}|_{\epsilon_F}$ and only terms up to the second order of ΔT are included.

To estimate the size of this contribution, one may calculate the ratio of the delta-T noise $S_{\Delta T}$ and the thermal noise S_{TN} . This is possible by calculating the ratio between the two terms of equation (3.8), where the first term is the thermal noise and the second one is the delta-T noise:

$$\frac{S_{\Delta T}}{S_{TN}} = \frac{F}{4} \left(\frac{\Delta T}{\bar{T}} \right)^2 \left(\frac{\pi^2}{9} - \frac{2}{3} \right). \quad (3.9)$$

For experiments in a helium cryostat the lowest possible temperature is $T_c = 4.2\text{ K}$. Assuming a high temperature $T_h = 7.8\text{ K}$ leads to a mean temperature of $\bar{T} = 6\text{ K}$. This \bar{T} results in a thermal noise of $S_{TN} = 2.56 \times 10^{-26} \text{ A}^2 \text{ s}$ for a contact with $G = 1 \text{ G}_0$. For a Fano factor of 1 , the delta-T noise is $S_{\Delta T} = 9.9 \times 10^{-28} \text{ A}^2 \text{ s}$, which is 3.9% of the thermal noise. A more realistic

²A classical $1/f$ -noise, will have an exponent of 2 , as Mu *et al.* uses squared noise densities, as also done in this thesis.

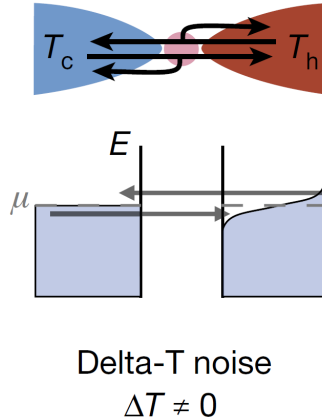


Figure 3.2: Schematic of a junction with a temperature difference over the constriction: Due to the smearing of the Fermi distribution, electrons pass through the junction summing to a net current of 0. Taken from [Lum+18].

Fano factor of 0.3 leads to a delta-T noise of 1.2 % of the thermal noise. Lumbroso *et al.* measured a value of about $5 \times 10^{-27} \text{ A}^2 \text{ s}$ for $\Delta T = 25.3 \text{ K}$ and $\bar{T} = 26.3 \text{ K}$. Additionally, they only show measurements for $G < 1 G_0$ which leads also to a low thermal noise. This increases the ratio in favor of the delta-T noise.

3.1.2 Shot Noise and Magnetism

Up to now only spin-degenerate transport through the contact has been considered. However, in magnetic materials, one has to account for the possibility of different transport probabilities for the different spin directions σ . This leads to two major changes in the considerations: The maximum contribution to the conductance per channel changes to $G_0^{\text{sp}} = G_0/2 = \frac{e^2}{h} = \frac{1}{25.8 \text{ k}\Omega}$. The second consideration leads to the fact that one has to sum over the spin configuration σ as well, if one wants to calculate the conductance and the Fano factor:

$$G = \frac{G_0}{2} \sum_{i,\sigma} \tau_{i,\sigma} \quad (3.10)$$

$$F = \frac{\sum_{i,\sigma} \tau_{i,\sigma} (1 - \tau_{i,\sigma})}{\sum_{i,\sigma} \tau_{i,\sigma}}. \quad (3.11)$$

A fully spin-polarized current through a single channel, results in a new limit for the excess noise, located below the limit for spin-degenerate transport. The area in between these two limits is forbidden for spin-degenerate processes, but may be occupied by partly or fully spin-polarized transport. Both limits and the additional allowed area are depicted in figure 3.3.

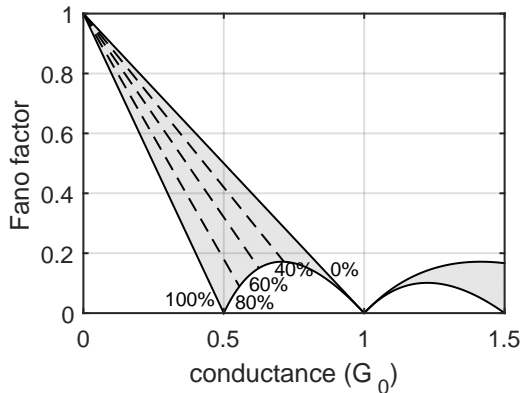


Figure 3.3: The minimal Fano factor allowed for spin-degenerate and spin-polarized transport differs for different conductances. This leads to a new area, highlighted in gray, where only spin-polarized transport can take place. The dashed lines indicate possible spin-polarization for one contributing channel for each spin direction. Adapted from [Bur+15].

Introducing the spin-polarization as

$$P = \frac{G_\uparrow - G_\downarrow}{G_\uparrow + G_\downarrow} \quad (3.12)$$

with G_\uparrow the conductance of all channels with spin-up and G_\downarrow the conductance of all spin-down channels. The polarization of the measured current can be estimated using equation (3.12). Figure 3.3 shows a few exemplary lines for polarizations assuming only two contributing channels, one for spin-up and one for spin-down electrons.

Burzlaff *et al.* reported first measurements of spin-polarized transport through single atoms [Bur+15; Bur+16]. They contacted single atoms of cobalt and iron on a Au(111) surface with a STM tip made of gold. Measuring the shot noise in the 100 kHz-regime leads to Fano factors which can only be explained by spin-polarization of about 40 % to 50 % (50 % to 60 %) for cobalt (iron). This result is emphasized in their DFT calculations predicting similar Fano factors. Further information about the measurements and the calculations also can be found in [Bur17].

In addition to the calculations of Burzlaff *et al.*, Pradhan and Fransson [PF18] also study the noise of a similar configuration. They are able to reproduce the experimental data and claim higher Fano factors for low transmission. They also calculate the influence of magnetic fields and temperature on the noise. For the used set of parameters one should be able to extract additional non-linearities in the voltage dependence of the shot noise. Unfortunately, it is hard to extract experimental parameters from the given information, since Pradhan and Fransson normalized their values to the uniaxial and transverse anisotropies, but do not give numbers to these parameters. Hence it is hard to estimate the probability to measure these

non-linearities.

Spin-polarized transport is expected for atomic wires of platinum [WW11]. Motivated by these calculations Kumar *et al.* tried to measure this spin-polarization by shot noise measurements [Kum+13a]. They found no clear indication for spin-polarization. Their own calculations reveal only weak polarization in the current carrying s-bands and strong polarization in the d-bands, which are only slightly involved in the transport. Therefore, they argue, that it is not surprising, not to measure the predicted spin-polarization.

Kondo Effect and Shot Noise

Additional to the effect of spin-polarization due to the magnetic moments, the Kondo effect (cf. section 2.2.2) may influence the shot noise. Cocklin and Morr [CM19] addressed that problem in a STM configuration from the theoretical side. They assumed different couplings between the tip and impurity (t_f) and the tip and surface (t_c). With the presented model, they are able to reproduce the Fano line shapes in the dI/dV curves. For a small coupling between tip and impurity ($\left| \frac{t_f}{t_c} \right| << 1$), leading to realistic Fano line shapes, the noise-voltage dependence differs a lot from the dependence without a Kondo impurity. Both, dI/dV and noise data, modeled by Cocklin and Morr are shown in figure 3.4. Similar dependence of the noise with respect to the voltage has been found by Strohmeier in atomic contacts of gadolinium [Str19]. Some of the curves presented there also show a bump at low voltages and transition into linear behavior. One of these curves and the corresponding dI/dV is presented in figure 3.4. Due to different geometry and a different material it is quite probable, that the dI/dV and also the anomaly in the noise, in shape as well as in voltage, differs from the calculations. Nonetheless, the calculations for $t_f/t_c = 0.01$ reproduce the shape of the anomaly in the noise quantitatively. Here one has to analyze the data of [Str19] more carefully and also to investigate other materials before drawing conclusions.

3.2 Sample Preparation

The sample preparation for the measurement of shot noise in atomic contacts uses a well established process. For metals, which can be evaporated, a simple lift-off process is used. This process is well described for example in [Sch10; Kel15]. The process for the high reactive rare-earth metal Gadolinium (Gd) is described with all hitches by Strohmeier [Str19]. For some metals with high melting points, in this case platinum and iridium, a etch-off process was used. This etch-off process was developed for platinum in Konstanz by [Str10] and was adapted for iridium by [Kel15; Rit18]. A short overview over the two methods is given in the following.

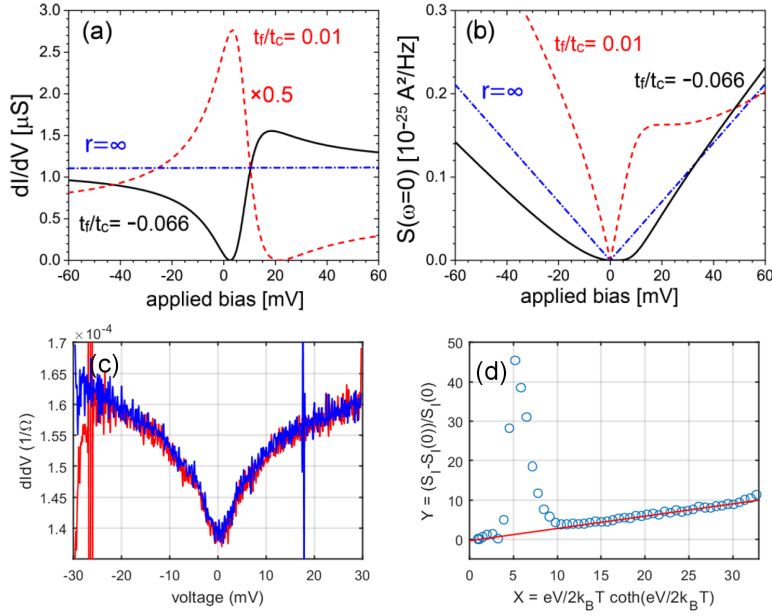


Figure 3.4: Calculated dI/dV (a) and zero frequency noise (b) in dependence of the applied voltage for a tunnel contact with a Kondo impurity. (c) A gadolinium contact with $6.5 \text{ k}\Omega$ shows a distinct ZBA. (d) The corresponding noise shows a peak at 4 mV. Theory and experiment are similar in the noise data for $t_f/t_c = 0.01$. The ZBA differs a lot in shape for that set of parameters. (a) and (b) are taken from [CM19], (c) and (d) are adapted from [Str19].

3.2.1 General Process

First, I want to concentrate on the lift-off process. A sketch of the different steps is depicted in figure 3.5. We are using either non-magnetic phosphor-bronze or Kapton [Fra17] as substrate. After polishing, a sacrificial layer of polyimide (PI, [Fuj19]) and the double layer resist, consisting of MMA-MAA EL11 and PMMA A4, are applied (a-c). Then the 5 cm diameter wafers are cut into $3 \text{ mm} \times 18 \text{ mm}$ chips. Each chip is exposed in a scanning electron microscope (SEM) with a dose of about $130 \mu\text{C}/\text{cm}^2$ with the desired pattern and developed in MIBK 1:IPA 3 for 25 s, rinsed with IPA and blown-dry with N_2 (d-e). Then the desired metal is evaporated at UHV conditions. Often one aims at a thickness of 80 nm. The excess material is removed in a lift-off process in acetone at 60°C . For getting a free-standing constriction, about 500 nm in thickness of the PI is removed in a O_2 - or O_2SF_6 -plasma.

The etch-off process is a bit more complicated. Here also the substrate is polished and then coated with PI. But before applying the resist layers, the metal will be sputtered on. The sputter process was done in house (for platinum) or by a collaboration partner in Cambridge³ (m-o). After cutting the wafer into chips, the structuring is also done by e-beam lithography with an increased dose of $160 \mu\text{C}/\text{cm}^2$. After development, a 20 nm to 30 nm thick aluminium

³A. Di Bernardo, Department of Materials Science and Metallurgy, Cambridge

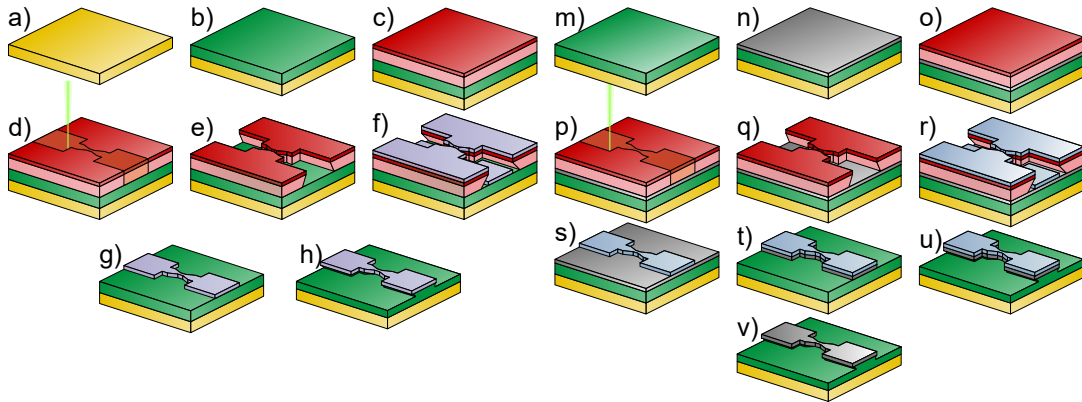


Figure 3.5: Different stages of the sample preparation for the lift-off process (a-h) and the etch-off process (m-v).

mask is evaporated and the additional material is removed in acetone (p-s). Two consecutive dry-etching steps follow: The first one structures the metal film in a SF₆ plasma, the second one is a O₂SF₆ plasma for underetching the constriction. The aluminium etching mask is removed in KOH afterwards (t-v).

Now the sample is ready to be contacted. This is done by gluing a thin copper wire to each contact pad. For electrical contact a silver conductive paint⁴ is used. For more mechanical stability a two-component epoxy⁵ is added next to the silver paint.

3.2.2 Sample Layout

For the samples a simple break junction (BJ) design was used. This design was initially used by Schirm [Sch10] and was slightly adapted. The constriction was designed to be 100 nm × 100 nm. The leads are 2 mm long and end in pads with a size of 0.5 mm × 0.5 mm. This design gives enough space to contact the sample with conductive silver paint. The wires are secured with two component epoxy next to the pads. On each chip, the design includes three constrictions and leads with pads. These three constrictions allow for more redundancy and speed up the contacting process if one of the constrictions is subject to contact problems. To account for small differences in the beam current, the dose factor of the three structures on each chip is varied by 5 %.

⁴SCP - Silver Conductive Paint; Electrolube; Leicestershire LE65 1JR UK; www.electrolube.com

⁵UHU Plus Sofortfest; UHU GmbH & Co. KG, D-77815 Bühl

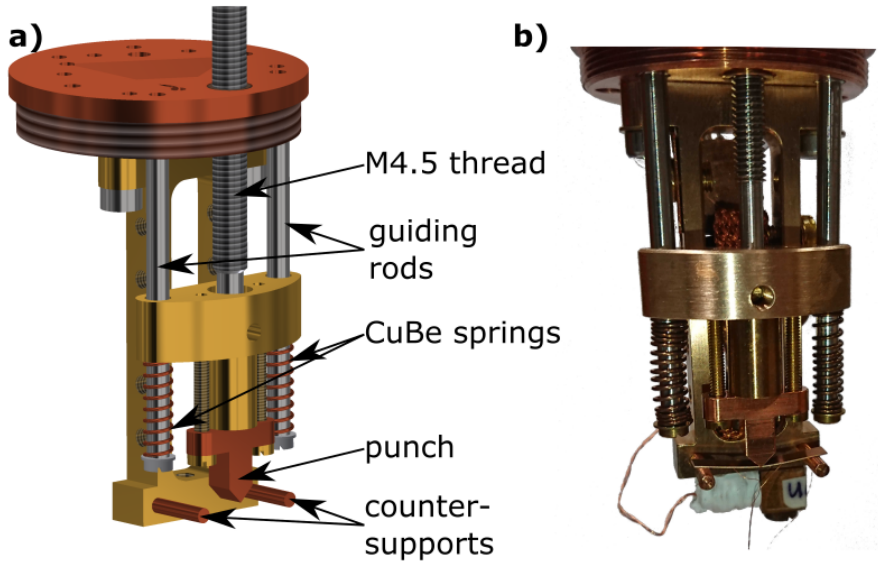


Figure 3.6: a) Schematic figure of the mechanics: The pushing rod is driven by a M4.5 thread and reset by two CuBe springs on the guiding rods. b) The photograph of the mechanics includes additionally an installed sample and the thermometer at the lowest part of the sample holder.

3.3 The Cryostat

The measurements are performed in a low temperature setup equipped with a break junction mechanics. For providing the cooling power, a bath cryostat with a superconducting magnet up to 8 T is used⁶. The breaking mechanics is installed into a variable temperature insert (VTI) by ICEoxford⁷ with a base temperature of 1.5 K. A functional drawing and a photograph of the breaking mechanics is shown in figure 3.6. The sample is mounted on two countersupports and is bent by a punch. The punch slides on two guiding rods and is moved by a simple screw, which is driven by a motor outside the VTI. The reset force, to move the punch back, is provided by CuBe springs wound around the guiding rods.

In the following the wiring and the electronic devices are discussed first, later the measurement procedure and the data storage will be covered.

3.3.1 Electrical Setup

There are two opposing requirements for the wiring: The first requirement settles on the fact, that we are dealing with high frequency signals. High frequency in this case means signals

⁶Oxford Instrument: Superconducting Magnet System

⁷ICEoxford Ltd.: ⁴ICE^{DIPPER} VTI

up to 2 MHz. At these frequencies one has to account for influences of the impedance $Z = R + j(\omega L - \frac{1}{\omega C})$. The second requirement is a good thermal contact with the bath to reduce the electronic temperature of the sample. Since the influence of the impedance on the measured spectra is more restricting, I decided to concentrate on the impedance. The inductive part (L) is easy to avoid. However, the capacitance is limited by the geometry. Here, the ~ 1 m long tubing from room temperature to low temperature was the most difficult part. I decided to use a long thin insulated copper wire, inside a PTFE sleeve. For equal spacing in the tube, I placed Teflon spacers every 10 cm, to ensure a concentric layout. To lower the electronic temperature, the wires have to be anchored thermally. This anchoring is done by a 10 cm long Manganin wire, which is directly glued to a copper rod with GE varnish⁸. To enhance the cooling in this part a copper bar was screwed on top of the wire while the GE varnish was still liquid. The overall capacitance of one line to ground is measured to be about 50 pF.

3.3.2 Measurement Electronics

In this paragraph, the electric devices of the setup are described. All devices are depicted in [figure 3.7](#). For mechanical control of the break junction a motor with a motor controller from Faulhaber⁹ is used. The superconducting magnet is controlled via a specialized power supply¹⁰. Most interesting is the electronics which is used to measure the transport characteristics. The transport measurements are controlled with inserts into a NI PXIe-1073 chassis with five possible slots. A NI PXIe-4463 card is used to source a voltage up to ± 10 V. The card is used to supply simple DC or a voltage ramp.

To ensure that a clean, noiseless signal is supplied to the sample, an active low-pass filter is used. This device was designed for adding and filtering two lines. In this setup just one input line is used. The original design was created by M. Herz and the device was fabricated by the electronics workshop of the university. A circuit diagram is provided in the appendix. This adder is powered by a battery pack to avoid any ground loops. The cutoff frequency is 16 Hz. This value is high enough to allow the voltage sweeping necessary for the *IV* measurements, but cuts off all unwanted noise and parasitic signals.

The current across the sample is converted into a voltage by the IV converter IVF10M, produced by JanasCard¹¹. The converter is designed to work up to 2 MHz at 10^6 V/A amplification and up to 450 kHz at an amplification of 10^7 V/A. All specifications can be found in [table A.1](#).

The converted current is measured by a NI PXIe-5922 card. This card serves as a low-frequency oscilloscope for measuring the current in standard IV traces or during histograms.

⁸VGE-7031

⁹Dr. Fritz Faulhaber GmbH & Co. KG

¹⁰Intelligent Power Supply, Oxford Inc.

¹¹JanasCard, Prague, Czech Republic, info@janascard.cz

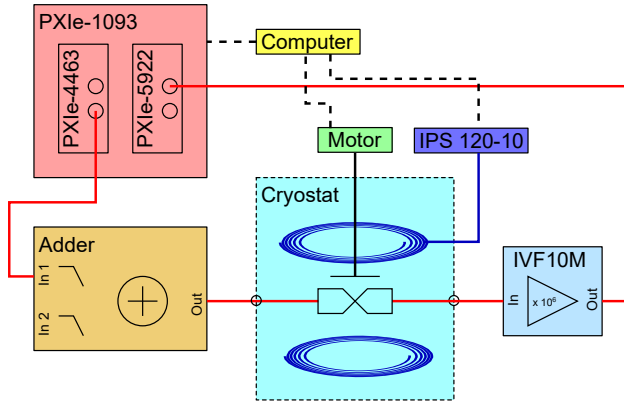


Figure 3.7: A schematic overview of the different devices, which are used to control the setup and measure the transport properties is shown. For a overview of the different noise sources, refer to figure 3.9.

For measuring the noise spectra it is possible to increase the sample rate and measure multiple spectra in short time.

3.3.3 Measurement Procedure and Data Storage

In the previous sections the setup and the used devices are presented. To get information about the spin-polarization and the channel configuration of atomic contacts it is necessary to measure many contacts. This is done in an automated way. For controlling the measurement and saving the measured data a LabVIEW based program was developed. The concept of a modular software was developed by Lorenz [Lor18] and his concept was adapted. In the following sections I will concentrate first on a pre-characterization and then on the noise measurement.

After cooling down the sample from room temperature to liquid helium, a soft electromigration [Hof17] is performed. This step reduces contamination and lattice defects. This is followed by the initial break of the sample. If the sample closes again, a histogram is performed. Therefore, the sample is repeatedly opened and closed. Normally about 300 to 500 opening traces are recorded before the actual histogram is calculated. It provides information about the purity of the metal and also tests, if the break junction works properly. Then one may decide, whether a sample is worth measuring or not.

After this pre-characterization, the measurement of the noise characteristics of atomic contacts starts. As already indicated this is normally done in an automated way. The routine opens the contact until it is in a given resistance range. Then an *IV* curve is recorded to be

able to calculate the resistance of the contact. Afterwards, noise spectra at different bias voltages are gathered. To avoid any problems with small offsets in the sub mV range, the voltage span starts at small negative voltages and goes up to positive 30 mV to 40 mV. Finally, a spectrum at 0 V and another *IV* curve are recorded. Both serve as an indication if the contact was stable over the measurement time.

3.4 Digital Data Processing

In this section, the processing of the measured data is described. All the processing is done in MATLAB. The process is exemplified mainly on a 10 k Ω resistor, which also served as a noise source for the calibration of the setup. After a quick look into the resistance calculation, we will have a look into the modeling of the noise and how the noise contributions of the devices play a role. Then, I will give a short survey over the two ways of analyzing the data: First, I will show the analysis in reduced quantities ([section 3.4.4](#)) and afterwards I will briefly discuss the estimation of the phonon energy ([section 3.4.6](#)).

3.4.1 IV Curves

As already mentioned, two *IV* curves are recorded for each contact. One before the actual noise measurement and one afterwards. There are two reasons for this procedure: The first one is, that we leave out contacts for which the two *IVs* and the corresponding dI/dVs are not similar. The second reason is that one can easily extract the resistance of the sample from these curves. The resistance is determined as the slope of a linear fit to the *IV* curve at small bias. A second possibility to determine the resistance, is the mean value of the numerically calculated dI/dV . One has to consider the additional low-temperature resistance of the setup $R_{\text{setup}} = R_{\text{amp}} + 2 \cdot R_{\text{cable}} \approx 110\Omega$. This value has been confirmed by cooling down a zero-ohm resistor instead of a sample and is subtracted to get the sample resistance R_{sample} . Two *IV* curves, one for a 10 k Ω resistor and one for an atomic gold contact are shown in [figure 3.8](#).

3.4.2 Peak Removal

In principle, the setup has been optimized not to show any distinct peaks at single frequencies in the noise spectra. Unfortunately the setup is sensitive to disturbances from the magnet power supply and other setups in the lab. These disturbances show up as narrow peaks in the spectrum and influence the data analysis.

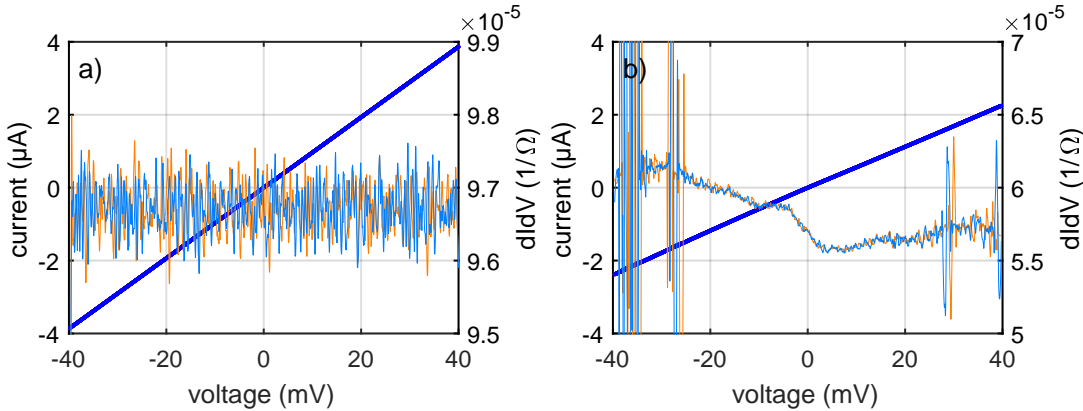


Figure 3.8: **a)** IV (red/ blue) and dI/dV (orange/ light blue) curves of a $10\text{ k}\Omega$ resistor measured to be $10.34\text{ k}\Omega$ at low temperature and **b)** of an atomic gold contact with a resistance of $17.17\text{ k}\Omega$ are shown. The curves before (red/ orange) and after (blue/ light blue) the noise measurement are similar.

Therefore, all distinct peaks which protrude the surrounding signal more than about 20 % are removed. This is done with the MATLAB routine `findpeaks`, which also gives the half width at half maximum (HWHM) of the peak. All data points in an interval $[-1.25, 1.25] \cdot \text{HWHM}$ centered at the peak location are excluded for the following analysis.

3.4.3 Noise Modeling

Different influences of the setup change the measured noise. To reveal the noise contribution from the sample, one has to determine the so called transfer function. To calculate the transfer function, the different noise sources and influences from the impedance have to be included in the modeling. All these sources and the relevant parts of the setup are displayed in [figure 3.9](#). The transfer function presented here has been developed in collaboration with T. Möller and M. Strohmeier.

The different noise sources are:

Source The voltage source, in this case the home-built adder (see [section 3.3.2](#)), adds some intrinsic noise to the system. The noise of the adder including the noise of the source is heavily filtered by the low-pass filter in the adder. An estimation (see [appendix A.1.1](#)) adds up to about $23\text{ pV}/\sqrt{\text{Hz}}$.

Amplifier The IV converter adds two different noise contributions to the signal: The input voltage noise $W_u^{\text{amp}} = 2.82 \times 10^{-18}\text{ V}^2/\text{Hz} - 6.59 \times 10^{-25}\text{ V}^2/\text{Hz} \cdot f$ and the input current noise W_i^{amp} . The first one is described in detail in [appendix A.1.2](#), the second can be measured with an open input (for a spectrum see [figure 3.10](#)).

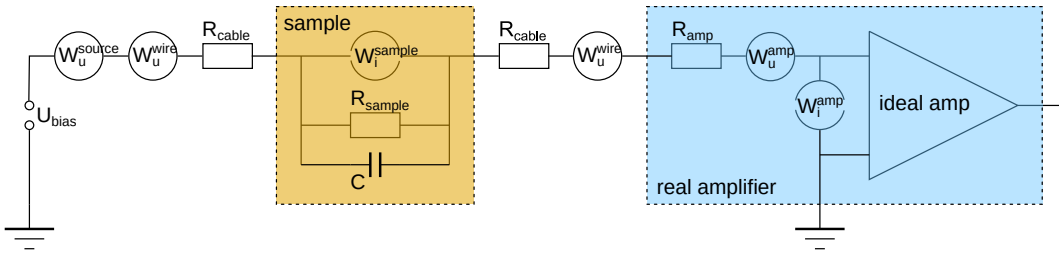


Figure 3.9: To calculate the transfer function all different noise sources, resistances and the total capacitance of the circuit have to be known. Here all these factors are depicted and labeled. The exact values and noise contributions are given in the text.

Wiring The wiring of the cryostat also adds some voltage noise to the system. It has been determined to be $W_u^{\text{wire}} = 1.8 \times 10^{-19} \text{ V}^2/\text{Hz}$ by cooling down several resistors to 4 K and measuring their noise.

Sample The noise contribution of the sample is the contribution of interest. For an atomic contact, it consists of a thermal and an excess noise part. To verify the setup a simple resistor and a diode were measured. There, one expects just thermal or shot noise respectively.

All these contributions add up, but different sources have different frequency dependences due to the impedance of the system. The relevant resistances of the system are the resistance of the sample R_{sample} , which is meant to change and additional resistances of the setup (R_{setup} , R_{cable}), making up 110Ω at low temperature. There are different capacitances (C_{sample} , C_{cable} , C_{BJ} , C_{amp}), which all collapse into a single capacitance C in terms of equivalent circuit theory. This capacitance is shown in figure 3.9 in parallel to the break junction. Since any loops in the cabling have been avoided, the inductance should be negligible and is not necessary for modeling the noise.

The noise density S_I of the sample can be calculated from the measured signal \tilde{S} with

$$S_I = \left[\tilde{S} - W_i^{\text{amp}} - \frac{W_u^{\text{amp}}(f) + W_u^{\text{source}} + W_u^{\text{wire}}}{|Z_{\text{total}}|^2} \right] \cdot \left| \frac{Z_{\text{par}}}{Z_{\text{total}}} \right|^{-2} \quad (3.13)$$

with the impedance $Z_{\text{par}} = \left(i\omega C + \frac{1}{R_{\text{sample}}} \right)^{-1}$ and the total impedance $Z_{\text{total}} = Z_{\text{par}} + R_{\text{setup}}$. Since the capacitance changes from contact to contact, and also slightly depends on the exact geometry of the sample, it is not possible to determine the capacitance by a calibration measurement. Therefore, we use equation (3.13) together with the spectrum at 0 V. In this case we expect the noise to be only determined by the thermal noise $S_I(0) = S_{\text{thermal}} = 4k_B T \frac{1}{R}$ for all frequencies. By fitting of \tilde{S} with the inverse of equation (3.13) it is possible to get values for C and T . This fitting is depicted in figure 3.10 for the $10 \text{ k}\Omega$ resistor. One has to mention,

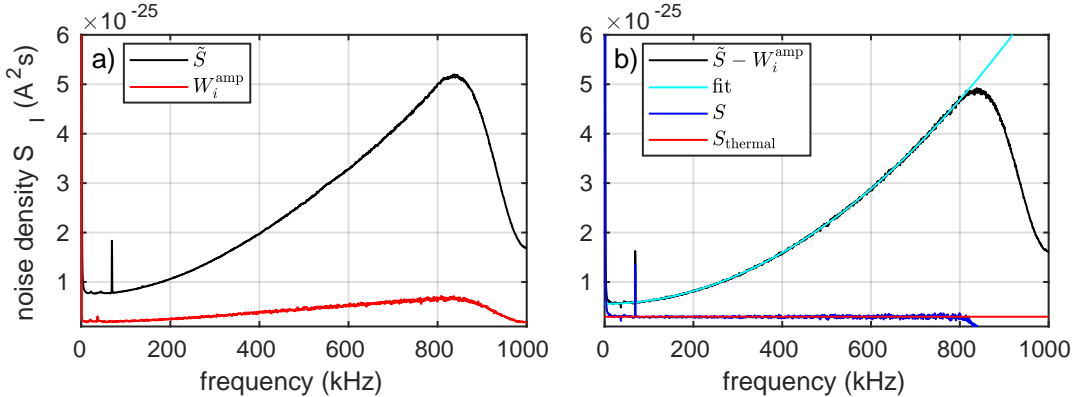


Figure 3.10: Correction of the measured noise: **a)** The measured noise \tilde{S} and the current noise contribution W_i^{amp} of the IV converter measured with an open input. **b)** The partial corrected noise $\tilde{S}^* = (\tilde{S} - W_i^{\text{amp}}) \cdot \Gamma$, the fit to this noise \tilde{S}^* with equation (3.13) to reveal the corrected noise S , which is the thermal noise S_{thermal} of the sample, in this case a $10 \text{ k}\Omega$ -resistor.

that two consecutive fits are done, one at low frequencies to determine the thermal noise and one over the full range to model C .

This correction can be applied to all spectra, recorded for one contact leading to mainly white spectra which are offset by a small value. This value is the additional noise contribution due to the shot noise of the contact. Exemplary corrected spectra are displayed in figure 3.11 for one gold contact. This prepared data can be processed further. The two possibilities are described in the next two sections.

For comparison, the spectra of a diode¹² are also displayed in figure 3.11. For low frequencies, the diode show full shot noise of $2eI$. At higher frequencies recombination processes appear and the expected shot noise changes (see [BS71]).

3.4.4 Fano Factor Analysis

The corrected spectra, as shown in figure 3.11, are further processed to extract the Fano factor. There are two possibilities depending on the $1/f$ -noise in the high voltage spectra. The simple possibility is to average the noise in a certain frequency interval. The lower limit of the interval is chosen in a way, that all low-frequency disturbances are excluded: A default value is 100 kHz. The upper limit is normally given by the cutoff frequency of the oscilloscope, which lays at 800 kHz. This cutoff is well visible in all spectra. The averaged noise is labeled with $\langle S_I \rangle(V)$. This method is depicted in figure 3.12 a). The second possibility includes the fact, that the average over a spectrum will often include some $1/f$ -noise, which

¹²6A80G from Taiwan Semiconductors [Tai].

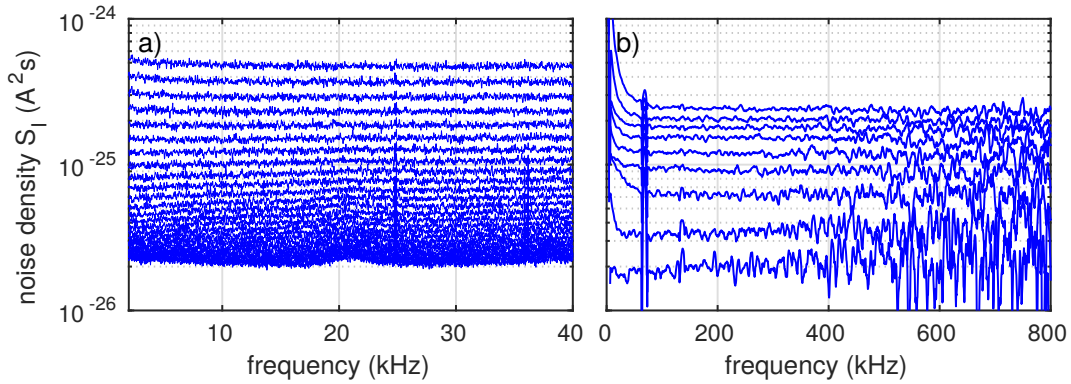


Figure 3.11: **a)** The noise of a standard diode to verify the full shot noise $2eI$: The offset of each curve with respect to the zero voltage curve is proportional to the full shot noise $2eI$. **b)** Spectra of an atomic gold contact with $17.17\text{ k}\Omega$. Here, the offset is reduced by the Fano factor $F = 0.304$. For clearance only nine spectra up to the same current as for the diode ($\approx 2.3\mu\text{A}$) are shown.

will add an additional component, especially if the upper limit of the frequency range is, because of disturbances, not available. This will lead to an error, which increases with the bias voltage. If one assumes only $1/f$ -contributions, one may extract the constant white part of a spectrum by fitting the spectrum. Since in this thesis squared noise units are used, the used function is $S_I(f) = (a/f)^\alpha + b$. This ansatz is necessary, because of several frequency dependent contribution to the noise. Some fits to the noise are shown in figure 3.12 b). A similar way is described by Mu et al. [Mu+19] in their supporting information. They find an exponent $\alpha = 1.5 - 1.7$, which is comparable to the value found for α over all investigated materials in this work. The white-noise part of the spectrum is then $\langle S_I \rangle(V) = b^2$. Except for the gold sample and some resistors, large $1/f$ -noise contributions and/or disturbances at higher frequencies are present. Therefore, only the $1/f$ -method is used in this work.

For extracting the Fano factor it is useful to use the already introduced reduced quantities X and Y (equations (3.6) and (3.7)). With these, one can extract the Fano factor F with a linear fit to the gathered data by using $Y(V) = (X(V) - 1) \cdot F$. One example of such a fit, together with both methods for gathering the reduced noise, is shown in figure 3.12. There the fit is done up to $X = 20$ for the $1/f$ -data. In this interval the both methods would give a similar result, but for other contacts the non-linear increase of Y starts at even lower voltages.

3.4.5 Limits and Uncertainties of the Noise Modeling

The noise modeling is the backbone of the data analysis. Therefore, a careful look into the uncertainties and pitfalls follows.

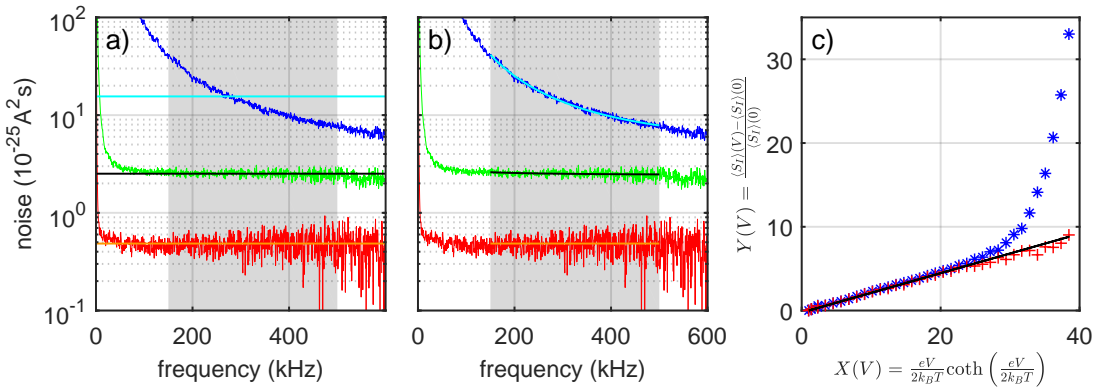


Figure 3.12: The processing of the noise data to reveal the Fano factor, exemplified for a platinum contact. **a)** The classical method by averaging the spectra in a frequency interval, here marked in gray. **b)** To consider the $1/f$ -noise one may fit the spectra with $(a/f)^\alpha + b$. Here shown for three selected voltages. **c)** Comparison of the two averaging methods and the liner fit. The * markers came from the averaging, the + markers from the $1/f$ -fitting and the black, solid is the linear fit with Fano factor $F = 0.235$.

1. Zero Bias Anomalies: Many of the investigated metals tend to show ZBAs, especially Kondo resonances. Hence, the resistance of the sample is voltage dependent. The shape of the dI/dV s should be included in the analysis, since Cron *et al.* demonstrated the effect of the shape of the dI/dV on the shot noise [Cro+01]. Since no lock-in amplifier was used, all dI/dV traces are numerically differentiated. This leads to noisy dI/dV curves, which cannot be used for the analysis of the measured data. To calculate the temperature, the resistance at low bias ($V \leq 10$ V) was used.
2. Thermal noise vs. temperature: The thermal noise of the sample is fitted with equation (3.13). To extract the sample temperature T , one needs the resistance of the sample. T is later used to calculate the reduced quantities X and Y . Therefore, all uncertainties of the resistance will directly influence the calculated temperature, X , Y , and the fitted Fano factor.
3. Capacity C : The increase of the spectra with frequency might be modeled by a capacitive effect inside the sample. But due to the layout of the IV-converter one does not get the pure capacity of the setup and the sample. Thus, the extracted parameter has only limited physical significance and is better described as a model parameter.
4. Amplifier noise: The noise (current and voltage) might be changing over time, mostly due to temperature effects. Even though the input current noise was measured regularly, small deviations are still possible. The input voltage noise is not easy to determine, and may be affected, too. Changes of either in the range of only 5 % may lead to a temperature error of up to 1 K.

5. Thermal coupling: Since the sample is not immersed directly into the liquid helium, but measured inside a vacuum chamber, which is inside the liquid helium, the exact thermal couplings via exchange gas and metallic thermalization are important for the resulting temperature of the BJ.

Since in this work the Fano factor analysis (see [section 3.4.4](#)) is done via the reduced quantities, the influence of the temperature uncertainties to the Fano factor have to be considered. For low temperature and higher voltages ($T < 6\text{ K}$ and $V > 2\text{ mV}$) $X \approx \frac{eV}{2k_B T}$. As already written, in this work $Y = \frac{[S_I(V) - S_I(0)] \cdot R}{4k_B T}$. With $\chi = [S_I(V) - S_I(0)] \cdot R$ the temperature dependence of the Fano factor in first order approximation is

$$F = \frac{\chi}{2} \cdot (eV + 2k_B T) . \quad (3.14)$$

The relative uncertainty of the Fano factor then reads

$$\frac{\delta F}{F} = \frac{2k_B \delta T}{eV + 2k_B T} . \quad (3.15)$$

If one assumes a voltage of $V = 9\text{ mV}$ and a temperature of $\bar{T} = 5\text{ K}$, leading to $X = 10.4$, as well as $\delta T = 1\text{ K}$ the effect on the Fano factor is $\frac{\delta F}{F} \lesssim 2\%$. Since in this work the fit goes up to $X = 15 - 20$, the uncertainty δF is even less. Therefore, this uncertainty is neglected for the Fano factor.

Nonetheless, one may calculate an uncertainty for the Fano factor on the bases of the variance of the excess noise and the range of the fit. Here, the range is the value X up to which one is able to perform the fit. The fitting procedure gives a confidence interval for the fit parameter. The interval for 99 % is used to determine the error bars of the Fano factor. Since often many data points are shown in the same graph, the error is given as color code: Fano factors with a small error bar are plotted in black, the bigger the error bar gets, the whiter the marker is displayed. As an indicator one can note that the error bar is smaller than the marker size for the majority of the data points.

3.4.6 Phonon Energy

Due to additional transport channels or changes in the transmission of single channels, there might be a change in the excess noise above the excitation energy of the phonon. Kumar *et al.* figured out that this influence leads to a kink in the excess noise at the phonon energy [[Kum+12](#)]. The new slope of the excess noise is either steeper or flatter than the original one, depending on the conductance of the contact. The exact reason for the change in the slope is still under debate [[Bah+19](#)], but up to now, one finds negative changes for $G < 0.95 G_0$ and positive changes above this threshold.

For the analysis, the lower part is fitted as already described by $Y = (X - 1) \cdot F$. Above the first and below a rarely occurring second kink, a linear fit is performed on the data. The phonon energy is calculated from the intersection of the two lines. Four examples of the measurements with a kink in the excess noise are shown in figure 3.13 b). There, also the fitting of the two parts is depicted. The dependence of the change in slope from the conductance is visible as well: The two contacts with $G < 0.95 G_0$ show a negative change in slope and the two with $G > 0.95 G_0$ show a positive change. Over all samples only a third or even a quarter of all contacts show nice kinks, which are usable for determine of the phonon energy. Most contacts show either no kink, exponential growth of the excess noise, or maxima in the excess noise. Nonetheless, the usable contacts have been analyzed and the results are presented for each material separately.

3.5 Results

In the following the results on the different materials and samples are presented. An overview over the samples is given in table 3.1. There, the samples are sorted by the material. This section is structured as followed: First, the reference measurements on gold and cobalt are presented. Gold is a good reference, since it has a single channel and is well investigated. Cobalt is a ferromagnet, which shows spin-polarized transport in STM studies on a gold surface [Bur+15; Bur+16]. Then, data on the strong paramagnets palladium and platinum are presented. For all samples one or more histograms are recorded before the actual noise measurements are performed. This histogram is used to confirm the material and to train the contact. This training is necessary to get reliable atomic contacts [Sab+12]. At the end a comparison between the three strong paramagnets platinum, palladium and iridium is made.

material	sample ID	electromigration	comment
gold	Simon_Test_2		test samples to check the setup and different amplifiers
	Simon_Test_3		
	MS3-II-13		
cobalt	34-III-13	yes	
	34-III-16	yes	
palladium	34-I-14		
	34-I-15	yes	
platinum	26-I-07	yes	

Table 3.1: Overview over the different measured samples.

3.5.1 Gold – Reference Material

Gold is a material which is used as a model for atomic contacts. Due to the single transport channel it is easy to understand the results of different experiments. Therefore, one can use gold as a testbed for the setup and the data analysis. The results here originate mainly from such test measurements.

For all presented samples the histograms show clear peaks at $1 G_0$, $2 G_0$, and $3 G_0$ as one may identify exemplary in [figure 3.13](#). This is a clear indication for the pure material we are using. The absence of peaks between $0 G_0$ to $1 G_0$ indicates the fact, that we do not have residues from the sample preparation left.

Gold is known to have a single channel transport in atomic contacts and is well characterized in many different studies on transport in atomic contacts (see [section 3.1.1](#)). Thus, gold samples are used to check the setup. In [figure 3.13](#) a typical distribution of the Fano factor in the measured gold samples is depicted. There, one sees that most of the contacts nicely follow the theory curve for a single channel as it is known from literature [BR99; Kum+12]. Additionally, one can analyze the excess noise in more detail and one can detect kinks at certain voltages. The energy at the kink correlates with the phonon energy as already pointed out by Kumar *et al.* [Kum+12]. Four examples for such kinks are shown in [figure 3.13 c\)](#). Out of the 374 measured contacts only 124 show a distinct kink, which allows for further analysis. The resulting voltages show a broad maximum in their distribution, with the maximum between 10 mV to 20 mV. This energy range is in agreement with previous shot noise measurements [Kum+12]. Agraït *et al.* investigated the shift of the phonon energy while stretching an atomic chain and found similar values via IETS [Agr+02]. It is an open question, why only a third of the investigated contacts shows a clear kink. Two explanations are given now: First, not all contacts show undisturbed noise up to high energies, but shows artifacts, which might superimpose the kink. Second, for other contacts the kink might not be visible, related to the zero crossing of the change of the Fano factor between $0.9 G_0$ and $0.95 G_0$ [Bah+19]. Contacts which are subject to one of the two features in excess noise curve may have a kink, but it is not detectable. Thus these contacts are not recorded in the statistics.

Both, the good agreement with the theory for spin-degenerate transport and the possibility for detecting the change in the Fano factor if an additional phonon is excited, is a good corroboration for setup and analysis.

3.5.2 Cobalt – Ferromagnetic Reference

As cobalt is a ferromagnet, it should show spin-polarized transport and is therefore a good material to check the setup. Additionally, I am unaware of any studies, which investigated

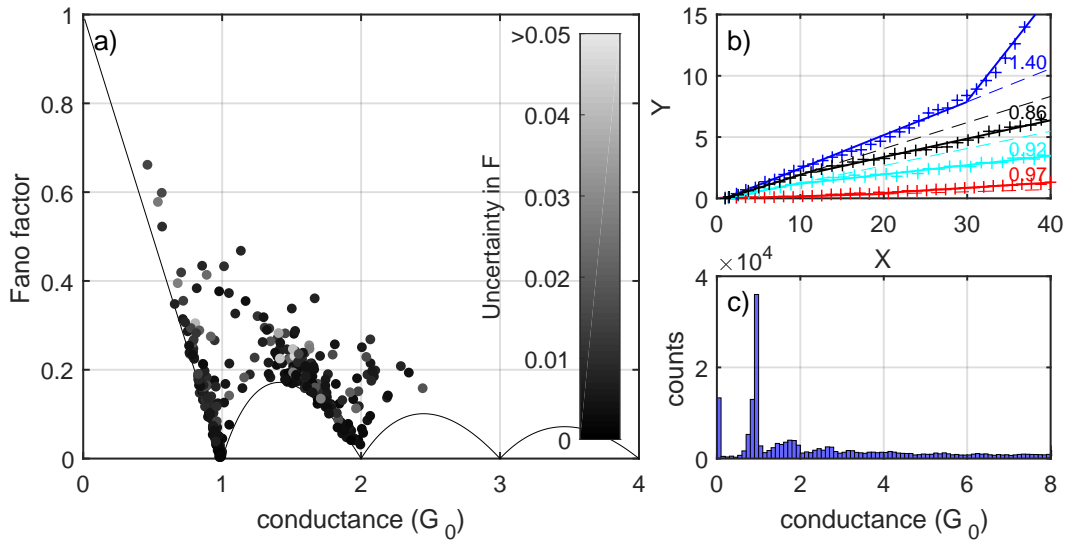


Figure 3.13: Conclusion of the measurements made on gold: All data shown here was recorded at the sample MS3-II-13. Both other samples support the presented data. **a)** The Fano factor of gold follows the theoretical, spin-degenerate curve for single channel transport well. The data points above that line can be attributed to a second channel contributing to the transport. **b)** Some measurements of excess noise, which show a kink due to phonon excitations: X and Y are defined as in equations (3.6) and (3.7). The numbers inside the graph give the conductance of the contact in G_0 . **c)** A typical histogram, showing pronounced maxima at $1 G_0$, $1.9 G_0$, $\sim 2.8 G_0$, indicating clean contacts. The other samples show similar histograms.

shot noise in atomic contacts of cobalt formed between leads of cobalt. There are measurements on single atoms on a Au(111) surface [Bur+15; Bur+16], which show spin-polarization for contacts which $G < 0.8 G_0$. This value is well below the single-atom regime. In line with Egle *et al.* [Egl+10] the single atomic contact found is at $1.0 G_0$ for both measured samples (see figure 3.14).

To cover a wide range of resistances, the noise measurement are carried out between $0.25 G_0$ ($50 \text{ k}\Omega$) and $3.25 G_0$ ($4 \text{ k}\Omega$). All measurements without applied field of the two samples are presented in figure 3.15. For both samples, there are contacts which can only be explained by some spin-polarized transport. Even though there are many contacts in the singe atom regime, most of the contacts showing spin-polarization are in the region below $1 G_0$. First the sample 34-III-13 (a) in figure 3.15) is discussed, the differences for 34-III-16 are addressed later.

Most of the data lies in the area of low to moderate spin-polarization up to about 50 %. This is comparable to the data presented by Burtzlaff *et al.* [Bur+15; Bur+16]. But here we are able to cover nearly the full range below $1 G_0$, whereas Burtzlaff *et al.* only show data around $0.6 G_0$. Additionally, there are a few data points around $1.5 G_0$, the single-atom contact regime, which might show a small amount of spin-polarization. But in comparison with the sheer amount

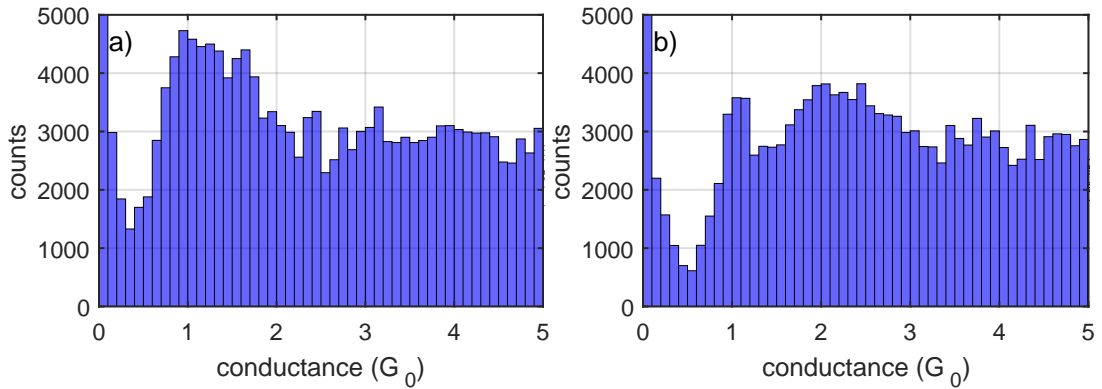


Figure 3.14: Conductance histograms for both cobalt samples: Only opening traces have been evaluated to calculate the histograms, which show a clear peak at $\approx 1.3 G_0$. **a)** Histogram of sample Co_34-I-15 and **b)** of sample Co_34-I-16: The last plateau which leads to the peak at $1.3 G_0$ is assumed to be the single-atom contact.

of data points well above the limit of spin-degenerate transport, these data points showing spin-polarization around $1.5 G_0$ are negligible.

The spin-polarization of roughly 50 % is comparable with results of calculations for atomic dimer by Häfner *et al.* showing a polarization of about 40 % [Häf+08] as well as results of measurements on point contacts by Soulen *et al.* leading to a polarization of 42(2) % [Sou+98].

However, there are differences between the two samples. For sample Co_34-III-16 the data points are more scattered. This sample even shows contacts with spin-polarization up to nearly 100 %. Also for the single-atom regime, there are data points which lie well in the spin-polarized regime. But for this sample also the uncertainty of the Fano factors is higher than expected. Especially in the spin-polarized regime there are many points with an uncertainty of 0.1 and more for the Fano factor. Up to now, there is no clear explanation for the high scattering and the high uncertainty. But one may think of defects and contamination, which spoils the signal of this sample. Even though the samples are prepared the same way, sample Co_34-III-16 may have suffered from additional oxidation due to slightly longer times between preparation and measurement. On the other hand, both samples underwent an electromigration process, which should have removed defects and contamination. But to measure the effect of this process is nearly impossible, since every sample behaves differently during electromigration.

Furthermore, some measurements with an applied field of 5 T and 8 T have been carried out on sample Co_34-III-13. This leads to the data shown in figure 3.16. External constraints prevented the measurement of a higher number of contacts. As a result, there are only about 100 points recorded per field value. This reduces the statistical significance of the presented data.

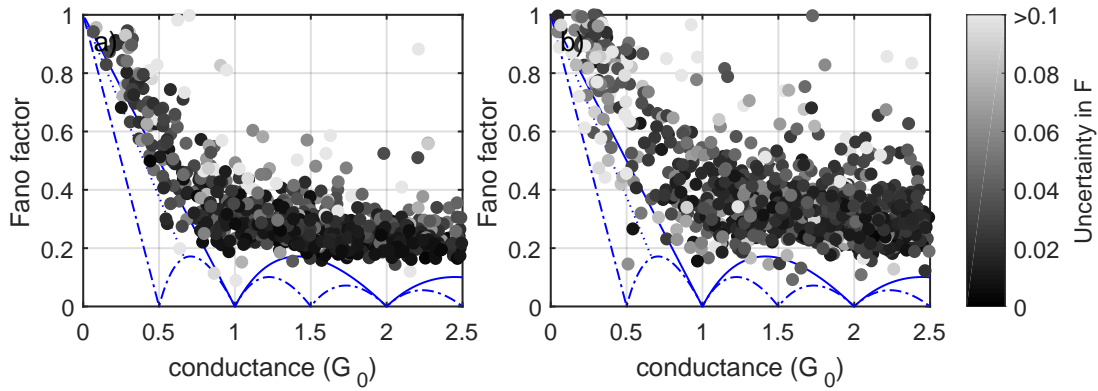


Figure 3.15: The excess noise for both cobalt samples including the uncertainty of the Fano factor encoded in the color of the data points: The colorbar on the right matches the color with the uncertainty. In **a)** sample Co_34-III-13 is depicted and sample Co_34-III-16 in **b)**. In both plots the minimal lines for spin-degenerate and full spin-polarization are displayed in full and dash-dotted lines, respectively. The dotted line indicates the 50 % line of spin-polarization for two channels. The scattering of the data points is bigger for the second sample.

At a field of 5 T, there are still some points at the border to the spin-polarized area, especially for low-conductive contacts. In addition to the tendency of more “spin-degenerate” transport, the data for 8 T shows a clear gap to the spin-polarized area. Up to now, there is no good explanation for this behavior. A shift to higher conductances is not expected, since there is no or only a small change in the overall conductance in a magnetic field (cf. [Egl+10] for measurement at 5 T). Burtzlaff *et al.* calculated the transport for cobalt ad-atoms on Au(111) in a STM configuration. They stated, that there is only one transport channel contributing for each spin direction [Bur+15]. One may argue, that with increasing field one adds additional channels of one (major) spin-direction. Normally this leads to an increase of shot noise. However, one may also argue that both applied fields are well above the saturation field for cobalt. Therefore, additional measurements with lower fields in the scale of some hundred mT would be more conclusive.

For both samples, the phonon energy has been evaluated and the distribution of the energies is depicted in figure 3.17. It shows a peak around 10 meV with a tail up to >30 meV. Both samples have a yield of about 25 % in the analysis of the phonon kink. The exact numbers are given in the upper right corner of figure 3.17. Interestingly, the distribution of Co_34-III-16 is more pronounced and less noisy, compared to sample Co_34-III-13. For the Fano factor, the behavior is inverted and the peak is at even lower energies for Co_34-III-16. Since the determination of the phonon energy is not the main part of this work and only a small fraction of the contacts could be evaluated, I will not concentrate too much on the exact reasons for the results of the phonon energies. However, Haefner *et al.* reported at least four contributing channels for the transport in atomic contacts of cobalt [Häf+08]. Thus, the simple

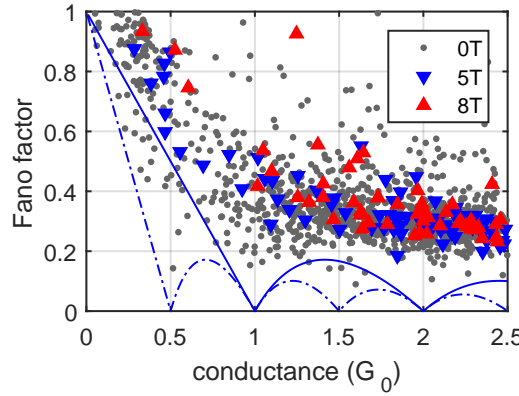


Figure 3.16: The influence of the magnetic field onto the excess noise. The data in gray is the same as already shown in figure 3.15 b). The data in blue (red) represent the measurements at 5 T (8 T). For clearness the uncertainty is not depicted. The excess noise seem to increase with increasing field, but there are less than 10 % of data points for the measurements in field (each) as for 0 T.

explanation, presented for gold, will not be applicable.

The measurement of atomic contacts of cobalt demonstrates, that it is possible to measure the spin-polarization in this setup. I was able to reproduce the data of Burtzlaff *et al.* and to measure the spin-polarization even in a broader conductance range. Additionally, the phonon energy in atomic contacts of cobalt could be determined to be around 10 meV.

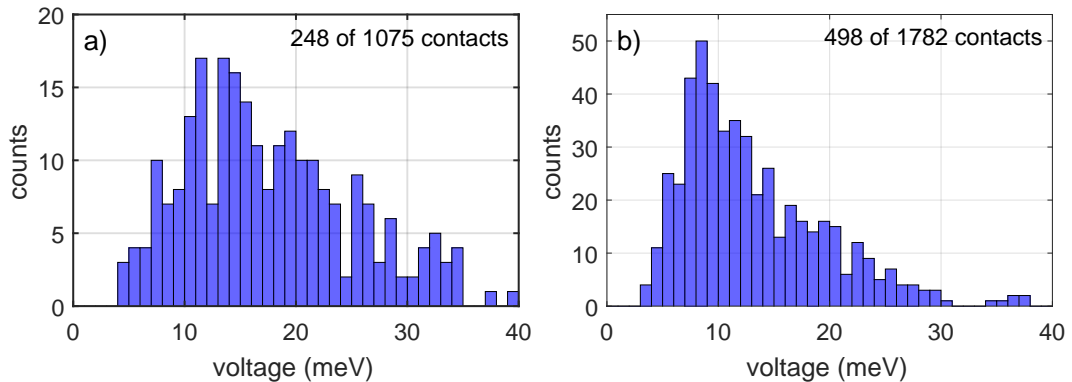


Figure 3.17: The distribution for the phonon energy, given in meV, for both samples **a)** Co_34-III-13 and **b)** Co_34-III-16 is depicted. In the upper right corner the number of contacts, for which the evaluation of the phonon kink was possible, is given in relation to all measured contacts.

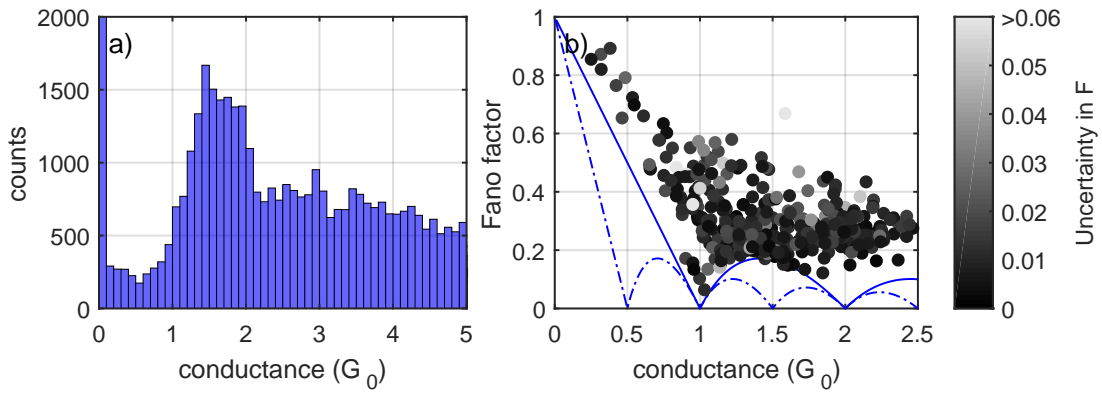


Figure 3.18: Results of the platinum sample: In a) the histogram of 205 opening traces is shown. The peak at $1.5 G_0$ is in good agreement with other publications. The excess noise is shown for 516 contacts in b). The data points accumulate at the line for spin-degenerate transport for the atomic contact regime. The color indicates the uncertainty of the Fano factor. For contacts below $1 G_0$ the points are clearly in the spin-degenerate regime.

3.5.3 Platinum

For platinum, Strohmeier reported only a few stable contacts below $1 G_0$ [Str19], where one would expect to measure the effects of spin-polarization. Also the sample presented here, shows the same problem. The results are summarized in figure 3.18. The histogram for this electromigrated sample shows a clear peak above $1.5 G_0$, as already reported by [Smi+01; Str10; Str19]. Below this conductance a dip develops, which is an indication for a clean break junction on the one hand, but makes it quite challenging to establish the wanted contacts below $1 G_0$.

The measurement of the Fano factor has been carried out at 585 contacts, out of which the Fano factor could be determined for 516. Those are depicted in figure 3.18, with the uncertainty in the determination of the Fano factor encoded in the color of the corresponding data point. It was possible to measure contacts down to about $0.5 G_0$, but all points below $1 G_0$ are well above the line for spin-degenerate transport. Only for contacts around $1.5 G_0$, the data points accumulate at the border to spin-polarization, as already found by Kumar *et al.* and Strohmeier [Kum+13a; Str19]. This result is not in agreement with the findings of Strigl *et al.*, who found a strong, non-monotonous magneto-conductance, which they explain with a selective scattering of electrons, due to their spin [Str+15]. Kumar *et al.* performed their own DFT calculations on atomic chains with four atoms, while varying the inter-atomic distance. They find a model with three different kinds of channels, two of which are non-magnetic and either full transmitting or medium transmitting. Especially the medium transmitting channels contribute to the noise. The third kind drives the magnetism, but is only low transmitting and, therefore, does not lead to a large contribution to the noise signal. Hence, one would not

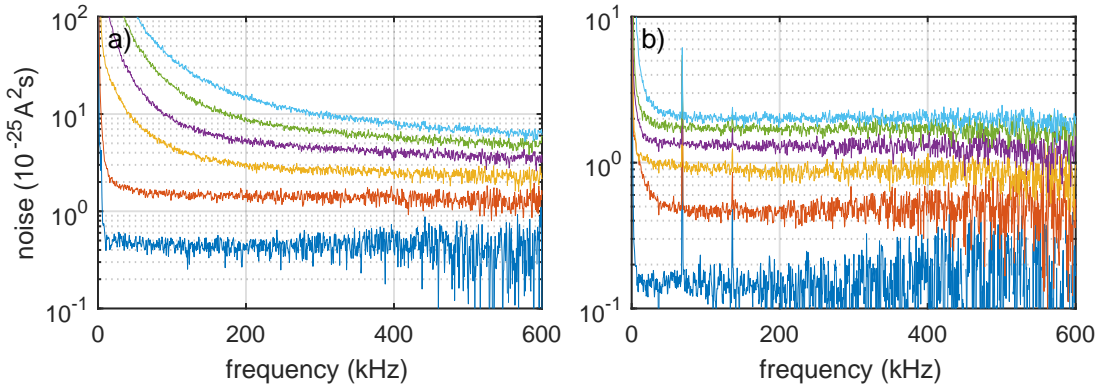


Figure 3.19: The spectra for platinum **a)** and gold **b)** differ at higher voltages, caused by $1/f$ -noise contributions to the noise. The two shown contacts also have different resistances and Fano factors, so the noise density is for high frequencies also not comparable.

expect a measurable effect of magnetism to the noise.

The spectra for higher voltages, or more precisely higher currents, show a strong $1/f$ -noise, which depends on the exact contact. Kumar *et al.* also mention a slight rise at low frequencies for higher currents [Kum+13a], they measure only up to voltages which are a factor of 3 to 4 smaller than the voltages used in this work. As already written in section 3.4.4, $1/f$ -noise contribution has been canceled out by the $1/f$ fitting procedure. Nonetheless, it is worth to keep it in mind. A typical series of spectra was already shown in figure 3.12, another is depicted in figure 3.19 together with some spectra of gold for comparison. As already mentioned, the reason for this $1/f$ -noise stays unclear, but of all investigated materials, platinum shows the biggest contribution. Kumar *et al.* noted defect fluctuations in the leads as one possible reason, which might explain the high contribution in platinum. Since the samples made from platinum are produced by sputtering, which might introduce additional defects into the structure, this might explain the additional $1/f$ -noise contribution.

The analysis of the phonon energy was successful for 148 of the 585 measured contacts. The results show a broad distribution of energies with its maximum somewhere between 10 meV to 25 meV. The small amount of data points makes any further analysis or discussion complicated, since it is unclear, if this is a real effect or just an effect of the small sample size.

3.5.4 Palladium

For palladium, two samples were measured. For both the results are similar, so both samples are discussed together. A clear atomic contact between $1 G_0$ and $2 G_0$ was found regardless of electromigration. The dip at conductances below the single-atom contact regime is deeper

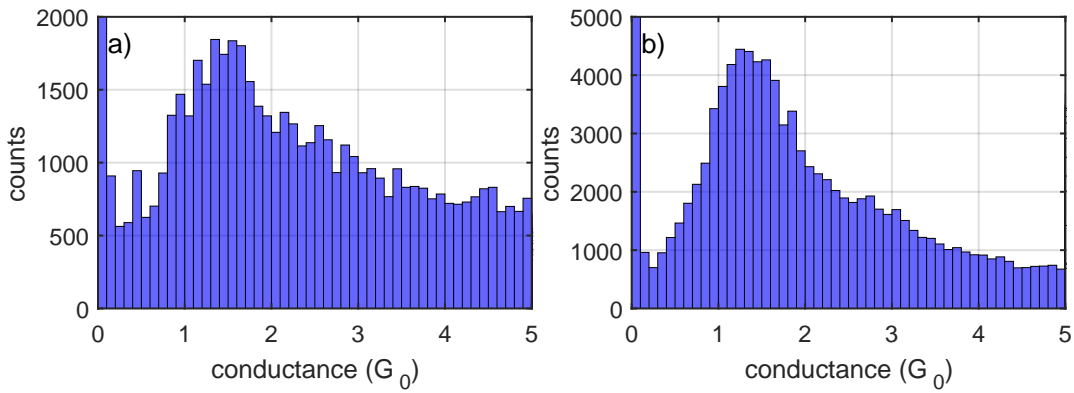


Figure 3.20: Histograms of both palladium samples, **a)** of sample Pd_34-I-14, which was not electromigrated and **b)** of Pd_34-I-15, which was electromigrated: Both show a peak between $1 G_0$ and $2 G_0$, which is characteristic for palladium. The dip below that peak indicates a clean sample.

for the electromigrated sample. This leads to the conclusion, that the electromigration removes unwanted contamination by molecules, left over from sample production, or heals out defects. Histograms of both samples are shown in [figure 3.20](#) and are in agreement with [Cso+04; Str+16], but the peak is at a bit lower conductance. The notch below $1 G_0$ makes it difficult to establish stable contacts in the regime, where in cobalt ([section 3.5.2](#)) most of the contacts with spin-polarization were found.

For both samples many contacts have been investigated with respect to the occurrence of spin-polarization. Overall, 1269 contacts have been measured and evaluated successfully. None of these contacts showed a Fano factor below the line for spin-degenerate transport. But for single-atom contacts and contacts with $0.7 G_0$ to $1 G_0$, the Fano factor seems to get close to this line. It is not clear, if this is just an effect of many contacts for the single-atom contact regime or an effect of one well conducting and the absence of other contributing channels. The results for both samples are displayed separately in [figure 3.21](#). For each data point the confidence interval was calculated for a value of 99 % of all possible values of F . This uncertainty of the Fano factor is encoded by the color of the data points. The lighter a point is, the bigger is the error bar. Prominent is the scattering of the data points for Pd_34-I-14 (left sample), which is not electromigrated. The reduction of the number of impurities near the constriction by electromigration, might explain this difference in scattering. Often impurities and imperfections in the lattice lead to two-level fluctuations which may increase the noise, especially at higher voltages [VZ83].

The reason why Strigl *et al.* found strong magneto-resistive effect [Str+16], but one does not find any indication for a spin-polarization with shot noise measurement is not clear. But my result is in agreement with findings of Kumar *et al.* on platinum. In contrast to platinum, however, there is no gap between the spin-degenerate line and the data points. This might

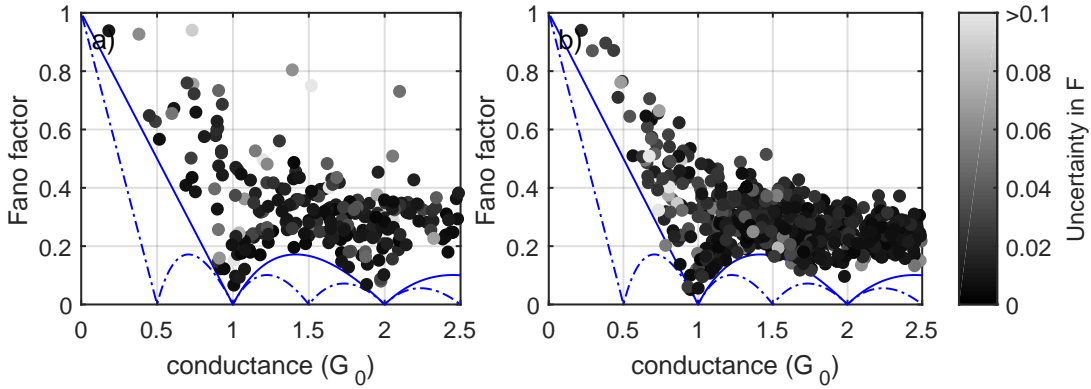


Figure 3.21: The Fano factor for both palladium samples: The measurement is shown in markers, whereas the uncertainty is depicted with different gray scales. Black for low uncertainty and nearly white for big uncertainty. The minimal lines for spin-degenerate and fully spin-polarized transport are shown in blue. The Fano factors scatter for the non-electromigrated sample Pd_34-I-14 **a)** and accumulate around 0.25 for sample Pd_34-I-15 **b)** for $G > 1.5 G_0$.

also be a result of the more extensive measurements. A further analysis of this gap is done in section 3.5.5.

Also for palladium, the evaluation of the phonon energy was performed and the distribution of the results is shown in figure 3.22. But since the number of the measured and, therefore, evaluable contacts is low, only the general trend and no exact numbers can be discussed. The overall yield is a bit higher, than for cobalt and platinum, since about 30 % of the contacts show a clear kink in the excess noise. The energy distribution shows a maximum around 10 meV, with a tendency to higher energies for sample Pd_34-I-14 and a bit lower energies for sample Pd_34-I-15. This energy is comparable with the assumptions of Keller, who estimated a possible phonon energy to be around 10 meV to 12 meV [Kel15]. For bulk palladium, the first phonons are excited around 14 meV [DSS81]. As already mentioned, Agraït *et al.* figured out, that the phonon energy lowers with additional tension in a contact [Agr+02]. Therefore, the presented values are reasonable.

3.5.5 Comparison between strong paramagnets

Using the results of Strohmeier [Str19] for iridium, one is able to compare the results of the three strong paramagnets platinum, palladium and iridium. All data are plotted in figure 3.23 without their uncertainty. Considering only the data points below 1 G_0 , a trend in the distance of the data points to the spin-degenerate single channel limit is visible. Some data points for palladium lie on that line, those of platinum leave a little spacing in between, and the bulk of the data points of iridium are clearly separated from the single channel line.

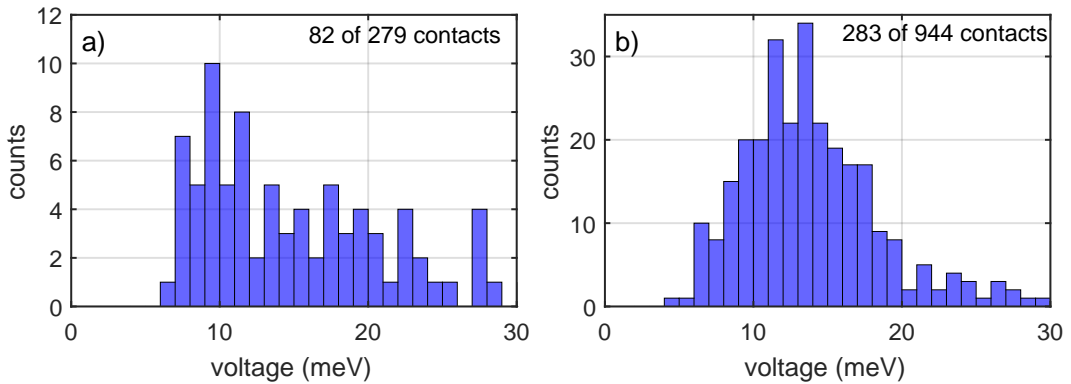


Figure 3.22: The distributions of the phonon energies for both palladium samples **a)** Pd_34-I-14 and **b)** Pd_31-I-15 are shown. The number of evaluable out of the measured contacts is given in the upper right corner. The overall number of contacts is low, so the significance is questionable.

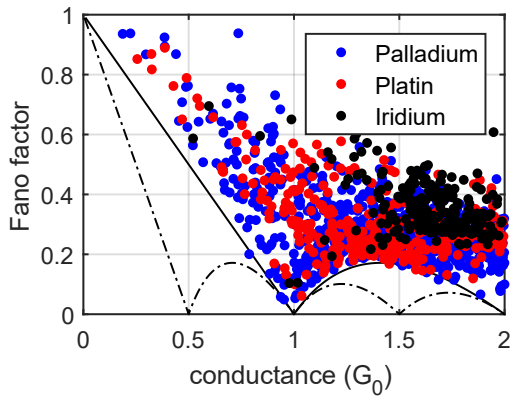


Figure 3.23: Comparison between the three strong paramagnets: The data points of palladium lie on the single channel line, those of platinum have only a little space and those of iridium show a clear gap.

One can note that the same order (palladium, platinum and then iridium) is also present in the Stoner enhancement $\frac{1}{2}UD(E_F)$ for these three metals. This parameter is already noted in [table 2.2](#) has the value 0.775 to 0.86 for palladium, 0.57 for platinum and 0.27 for iridium. These numbers are calculated from the parameters given in [\[And70; And+77; Jan77\]](#). There is no direct link between the Stoner enhancement and the magnitude of the shot noise. Especially the fact, that the shot noise is dominated by the number and the transmission of the channels, which are linked to the valence of the metal, makes a direct connection impossible. However, the Stoner enhancement as well as the shot noise are measures of the strength of magnetic correlations and may thus hint towards a connection between these properties.

3.6 Summary

The analysis of the shot noise leads to somewhat contradicting results. The measurements on gold show, that it is possible to measure shot noise of a single conducting channel, leading to a suppression of the shot noise for integer multiples of the conductance quantum $G = \frac{2e^2}{h}$. It was also possible to detect the characteristic kinks in the excess noise at the energy of the phonons. By fitting the data points with energy higher than the kink with a linear dependence, it is possible to extract the phonon energy. For gold the received values agree with older measurements and other methods [Kum+12; Agr+02]. Both results confirm, that the used system has the required precision.

The results for cobalt show a clear indication of spin-polarization in the range below $1 G_0$ as well as for single-atom contacts with a conductance of about $1.5 G_0$. But both measured samples differ in the maximum size of spin-polarization. Sample Co_34-III-13 show values up to 50 %, agreeing with calculation [Häf+08] as well as findings in STM configuration [Bur+15] and point contacts [Sou+98]. In contrast, sample Co_34-III-16 shows even higher values of up to nearly 100 % spin-polarization. Also the results for the phonon energy differ a lot for the two samples, here sample Co_34-III-16 shows the more defined value for the phonon energy of about 10 mV. The results of the measurements of shot noise in magnetic fields, showing less spin-polarization as without any applied magnetic field, are not intuitive at the first glimpse, where one would expect a higher spin-polarization in magnetic field. One explanation is the size of the applied field, which is well above the saturation field of cobalt.

The measurements for platinum and palladium show accumulated data points at the boundary to the spin-polarized transport, but no clear data points below the line for spin-degenerate transport. In platinum this result was already reported by Kumar *et al.* who had difficulties to establish stable contacts below the single-atom regime [Kum+13a]. But for the iso-electric palladium, it is easier to establish a broader range of stable contacts. Therefore, one also finds data points of the single-atom contact regime, which lie on the line between spin-polarized and -degenerate transport. But even for palladium it was not possible to find clear indication for spin-polarized transport. One possible explanation is given in [Kum+13a]: They argue with different contributions to the magnetism and the transport. This argumentation contrasts the findings of [Str+16], who reported a strong magnto-conductance in palladium. Up to now it is unclear, why nearly all atomic contacts show strong non-monotonous behavior of the conductance in magnetic fields, but the shot noise shows no spin-polarization. A comparison between the distance between the single channel line and the data points of the three strong paramagnets platinum, palladium and iridium shows the same trend as the stoner enhancement of the three metals.

The phonon energies for platinum lie in a reasonable interval but show a broad distribution. Therefore, one should perform further measurements to draw conclusive statements from

the data. The results for palladium lead to energies, which are a bit smaller than the bulk value, and are in the same range as those estimated by other methods.

Chapter 4

Spin Polarization Investigated by Multiple Andreev Reflection

This chapter deals with a different approach to investigate the existence of magnetic order in atomic contacts of strong paramagnets. The idea is based on transmission dependence of the shape of a superconducting IV curve of an atomic contact. Therefore, I will first introduce the relevant theory of superconductivity and the so called Multiple Andreev Reflections (MAR) in section 4.1. Since palladium, the strong paramagnet which I want to investigate, does not show superconductivity¹, one has to use the proximity effect, to render it superconducting. The sample preparation to achieve this goal is described in section 4.2. In section 4.3 the cryostat, the breaking mechanics, and the electronic setup are described. The results are presented in section 4.4 and discussed in section 4.5.

4.1 Theoretical Background

Superconductivity is a phenomenon, which was discovered by Kamerlingh Onnes in 1911. The main features of superconductivity are vanishing electrical resistance and perfect diamagnetism below a critical temperature T_c and a critical field B_c . There are two main theoretical models, which describe the phenomena. The phenomenological model by Ginzburg and Landau explains the superconducting state via an order parameter Ψ [GL50]. The microscopic model, developed by Bardeen, Cooper and Schrieffer in 1957, called BCS theory, is based on phonon mediated interaction between two electrons. This interaction leads to

¹Palladium has a strong electron-phonon coupling, and should therefore show superconductivity at “a reasonable high [...] transition temperature” [BR04], but is suppressed due to spin-fluctuations, thus, no superconductivity has been measured down to 1.7 mK [Web+78]. Palladium does, however, get superconducting below 3.2 K after irradiation with He^+ ions, since this introduces disorder, which prevents the spin fluctuations [Str79].

a pairing of two electrons with opposite momentum [BCS57]. An overview over the field of superconductivity is given in many textbooks like [BK13; Tin04; Poo+07]. Section 4.1.1 will be a short summary about the BCS theory, followed by an introduction to the channel analysis with MAR in section 4.1.3 and the effects of magnetism on the transport in section 4.1.4.

4.1.1 BCS Theory

Following [Tin04] one can show, by adding two additional electrons to the Fermi sea at zero temperature, that these two electrons with opposite momentum and spin, will form a so called Cooper pair. For the weak coupling approximation the energy for adding the two electrons can be written as

$$E \approx 2E_F - 2\hbar\omega_c \exp\left(\frac{-2}{N(E_F)V}\right) \quad (4.1)$$

with a small interaction V between the electrons and a frequency scale ω_c . E_F is the Fermi energy of the material and $N(E_F)$ is the density of states at the Fermi energy. The frequency ω_c can be assigned to the Debye frequency ω_D , as phonon mediate the interaction between the electrons. The second part of this equation is the binding energy of the Cooper pair.

To split the two electrons of a Cooper pair, one has to provide the energy Δ_0 at zero temperature:

$$\Delta_0 \approx 2\hbar\omega_c \exp\left(\frac{-1}{N(E_F)V}\right). \quad (4.2)$$

This energy is equal to the gap in the density of states. The critical temperature T_c is the point where the gap closes. If one compares Δ_0 and T_c one obtains

$$\frac{\Delta_0}{k_B T_c} = \frac{\pi}{e^\gamma} \approx 1.764 \quad (4.3)$$

for weak-coupling superconductors. Here $\gamma = 0.577$ is the Euler constant. In the case of non-zero temperature, the effective gap $\Delta = \Delta(T)$ is reduced. For weak-coupling superconductors Δ is almost constant for low T and drops sharply approaching T_c according to

$$\frac{\Delta}{\Delta_0} \approx 1.74 \sqrt{1 - \frac{T}{T_c}}. \quad (4.4)$$

To calculate the transport characteristics, one needs the quasiparticle² density of states N_S in the superconducting state:

$$\frac{N_S(\epsilon)}{N(E_F)} = \begin{cases} \frac{|\epsilon|}{\sqrt{\epsilon^2 - \Delta_0^2}} & |\epsilon| > \Delta_0 \\ 0 & |\epsilon| < \Delta_0 \end{cases}. \quad (4.5)$$

Here $\epsilon = E - E_F$ is the energy relative to the Fermi level and $N(E_F)$ is the normal conducting density of states at the Fermi energy. The density of states is depicted schematically in figure 4.1 for each side of the shown weak link.

4.1.2 Weakly Coupled Superconductors

In this work, we deal with weakly coupled superconductors. There are two main effects to account for: the Josephson effect and the tunneling of quasiparticles. There are many ways to establish a weak link. Common techniques are tunnel barriers (e.g. oxides), constrictions and (short) normal conductors, as well as suppression of the superconductivity with normal conductors or ferromagnets.

First, the Josephson effect is discussed briefly. This effect was predicted by Josephson in 1962 and describes the coupling between the superconducting order parameter of two superconductors over a transparent barrier [Jos62]. Since the density of states for the quasiparticles is left unchanged, one also speaks about tunneling of Cooper pairs. Since the two wave function may have a phase difference $\Delta\varphi$ over the barrier, the supercurrent can be calculated by

$$I_s = I_c \sin \Delta\varphi \quad (4.6)$$

with the critical current I_c . If one applies a voltage over the weak link, $\Delta\varphi$ will change with time and the supercurrent

$$I_s = I_c \sin \omega_J t \quad (4.7)$$

begins to oscillate with the Josephson frequency $\omega_J = 2eV/\hbar$.

For this work, the transport of quasiparticles over the weak link, with negligible Cooper pair tunneling, is the dominant process. To understand the following, it is useful to change to the so called semiconductor picture. There, one has a gap with no allowed states in $[E_F - \Delta, E_F + \Delta]$ for zero temperature and allowed states outside the gap according to equation (4.5) on each side of the tunnel barrier. In the easiest case, there is no voltage applied and, therefore, no current flows. If the voltage is sufficient ($eV \geq 2\Delta$) to align the occupied states (below $E_F - \Delta$)

²Quasiparticles are electrons and holes in the semiconductor picture.

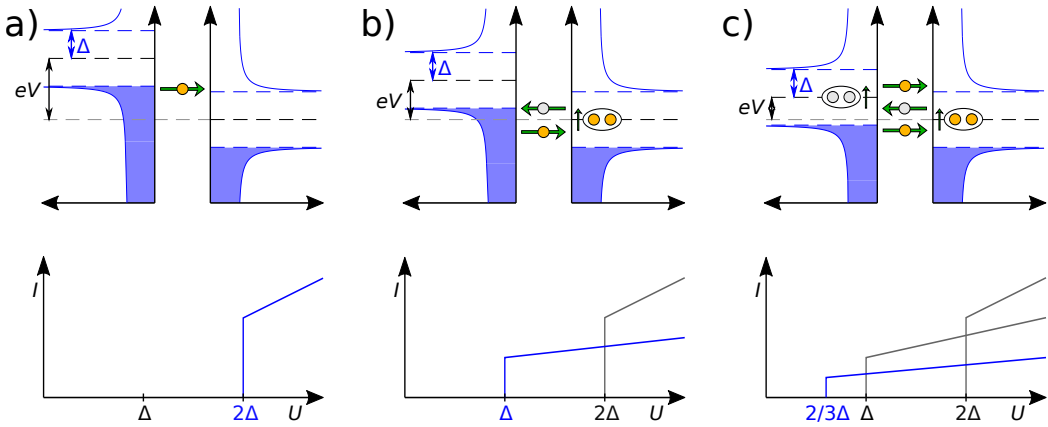


Figure 4.1: Transport between two superconductors at a voltage difference V : **a)** For $eV \geq 2\Delta$ quasiparticles can tunnel from one side to the other. **b)** For $\Delta \geq eV \geq 2\Delta$ a quasiparticle is transported, a Cooper pair formed and a second quasiparticle is transported back. Since two quasiparticles are transported, the probability is proportional to τ^2 . **c)** Including more quasiparticles reduces the needed difference between the Fermi energies and the probability for the process, shown here for three quasiparticles. The lower panels depict the simplified contributions of these processes to the transport.

on the left side with the unoccupied states (above $E_F + \Delta$) on the right side, quasiparticles may tunnel with the corresponding probability τ . This case is depicted in figure 4.1 a) together with a simplified IV trace for this process.

For lower voltages ($eV < 2\Delta$), there are no allowed states on the right side. But according to Andreev, there is the possibility of transport for $eV > \Delta$ [And64]. A first comprehensive explanation was given by Blonder *et al.* in 1982 for a superconducting - normal conducting contact [BTK82]. One year later also the superconducting case was covered by Octavio *et al.* [Oct+83]. They assume an electron tunneling from left to right and forming a Cooper pair there, while sending a hole back to the left superconductor. The probability for that process is lower than for single electron transport, since two quasiparticles have transferred and a Cooper pair was created (cf. figure 4.1 b)). So the overall probability is proportional to $\tau^2 \cdot |a_i|^2$, where τ is the transmission probability and a_i the Andreev reflection coefficient. Including further quasiparticles into the process allows transport at even lower energy differences between the two sides of the junction. This is depicted in figure 4.1 c).

4.1.3 Channel Analysis with MAR

The energies at which the processes occur are defined by the number of transported quasiparticles. But calculating the transported current for a given voltage and transparency of

the barrier, was only possible with the work of Blonder *et al.* [BTK82]. The first calculations were made for contacts between a superconductor and a normal-conductor (SN) with variable transparencies of the barrier between the two metals. Developing a theory to connect the somehow arbitrary transparency with the transmission of a contact in the sense of Landauer (see [section 2.1](#)) took some time. Using MCBJs and STMs creates adjustable SIS contacts, which lead to different approaches for that problem. Solutions have been presented by Averin and Bardas [AB95], Bratus *et al.* [BSW95] and Cuevas *et al.* [CMY96] using these different approaches. Here only the latter will be discussed in detail.

The model of Cuevas *et al.* is based on a Hamiltonian, which describes the contact region including the two leads. To calculate the transmission through the contact, they use non-equilibrium Keldysh Green's function theory. In the case of two superconducting leads, one has to use a recursive relation. It is possible to solve this recursion analytically for $eV \ll \Delta$ and $eV > \Delta$. For intermediate states one has to use a numerical solution. At zero temperature the exact current corresponding to a transmission at a given voltage can be calculated.

In [figure 4.2](#) the blue lines show the *IV* curves calculated with this model for selected single channel transmissions. For a perfect transmission the *IV* features a supercurrent. For contacts with a high transmission $\tau \geq 0.8$, a steep increase of the current for low voltage is expected, lowering the transmission increases the voltage at which the increase in current occurs. Furthermore, distinct features start to appear at certain voltages. At a transmission of 0.7 and lower, the structure changes into a step-like behavior, with the steps at voltages of $V = \frac{2\Delta}{n \cdot e}$ with an integer n . Summing up the contributions of two channels results in significant deviations from a single channel with the same overall transmission. Two examples are depicted by the dashed lines. For low voltages $eV < 1/2 \cdot \Delta$ it is hard to distinguish between the major channel and a sum. But the behavior for $eV > \Delta$ allows the distinction between the addition and a single channel.

The accuracy in assigning the correct transmission is limited by the resolvable difference between two curves with similar transmission. This problem limits the method to a certain number of participating channels. The same holds true when broadening effects due to non-zero temperature or otherwise disturbed BCS spectra occur.

4.1.4 Effect of Magnetic Impurities on MAR

A first theoretical approach to explain the effect of ferromagnetic materials in superconducting junctions has been published by Eschrig [Esc00]. This theory was soon generalized by Fogelström [Fog00]. For the case of atomic contacts including ferromagnetic effects, two pioneering articles are important. Martín-Rodero *et al.* investigated the effects of spin-filtering on the superconducting *IV* curves [MLC01] and Andersson *et al.* investigated the spin-mixing in such contacts [ACF02]. In the following, both articles will be discussed.

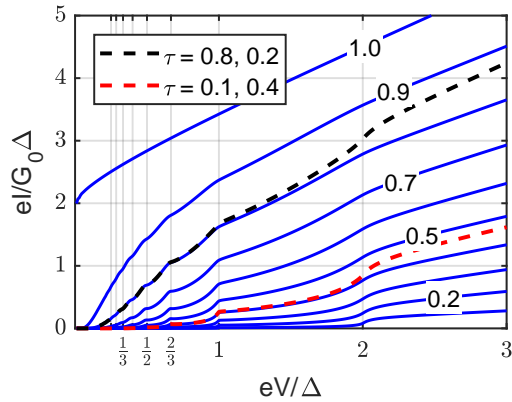


Figure 4.2: The current, calculated with [CMY96], for different single channels with the indicated transmissions is shown. The two dashed lines indicate the superposition of two channels with the given transmissions. Both axis are normalized.

Martín-Rodero *et al.* model the contact region by semi-infinite superconducting leads connected via a idealized atomic contact [MLC01]. For a normal conducting metal between the two superconducting leads, they obtain the results already presented in section 4.1.3. However, using magnetic materials, like cobalt, one has to account for the different transmission probabilities for spin-up and spin-down. In [MLC01], they present the energy dependent transmission for their idealized constriction made of cobalt leading to a ratio of approximately 0.5 : 3 for spin-up : spin-down. They used a time-dependent tight-binding Hamiltonian together with the Keldysh Green's function formalism to calculate the *IV* curves and the subgap structure. In figure 4.3 possible traces for a fully transmitting up-channel and various transmissions for the down-channel are shown. There are two effects visible in the presented curves: First, the step like structure has changed to a structure including peaks at low voltages, which get more pronounced at lower transmissions of the spin-down channel T_\downarrow . The second effect is the energy where the key features occur. These energies are mainly shifted to lower values. The authors give the relation

$$\epsilon(\phi) = \pm \frac{\Delta}{\sqrt{2}} \sqrt{1 + \bar{R} + \bar{T} \cos(\phi)} \quad (4.8)$$

for the Andreev bound state energy. This formula includes the superconducting gap Δ , the average transmission $\bar{T} = \sqrt{T_\uparrow T_\downarrow}$ and reflection $\bar{R} = \sqrt{R_\uparrow R_\downarrow}$ with $R = 1 - T$. ϕ is a constant phase difference equal to $2eV\tau/\hbar$. For the case of negligible T_\downarrow and full T_\uparrow the bound state energy reduces to $\epsilon(\phi) = \pm\Delta/\sqrt{2}$, which leads to subgap features located at $eV = \Delta/(\sqrt{2}n)$ compared to $eV = 2\Delta/n$ in the non-magnetic case.

Andersson *et al.* follow a different idea. They connect the two leads by a small magnetic dot with a magnetic moment $\vec{\mu}$ and size $d \ll \chi_0$, the superconducting coherence length. For their

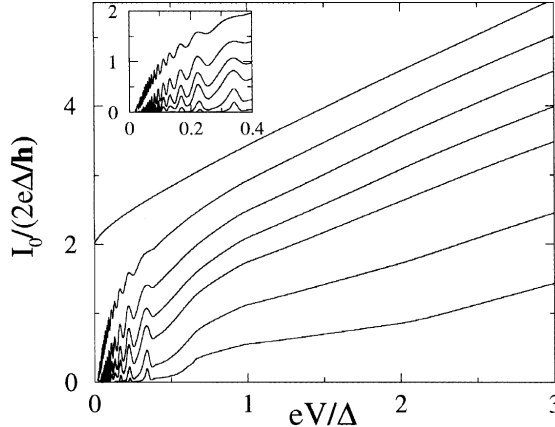


Figure 4.3: Some *IV* curves for a superconductor-ferromagnet-superconductor contact, as described by [MLC01], for $T_\downarrow = 1$ and $T_\downarrow = 1.0, 0.9, 0.8, 0.7, 0.6, 0.4, 0.2$ from top to bottom are shown. The inset is a zoom to the low voltage part. Taken from [MLC01].

calculations, they use a quasiclassical theory with a \hat{S} -matrix, including an additional term $\exp(i\frac{\Theta}{2}\hat{\sigma}_\mu)$. This leads to a rotation of the spin by Θ around the axis of the magnetic dot $\hat{\sigma}_\mu$. In the simplest case, they neglect any phase difference between the two leads³. This leads to an Andreev bound state at

$$\epsilon(\Theta) = \pm\Delta \cos\left(\frac{\Theta}{2}\right). \quad (4.9)$$

The energies of the current onsets are at

$$|eV|_n = \left(1 + \cos\left(\frac{\Theta}{2}\right)\right) \frac{\Delta}{n}. \quad (4.10)$$

Andersson *et al.* also give an example for possible transport processes as an explanation for the different onsets. The resulting *IV* characteristics for $\Theta = \pi/2$ are depicted in figure 4.4. There, the current onsets are already at decreased energies. The first onset is at $eV = 1.71\Delta$. Additionally, shallow maxima develop at the edges above the onset. These peaks get more pronounced for bigger Θ .

Both theories are limited to zero-temperature and to simplified cases only including one effect, spin-mixing or spin-filtering. Nonetheless, the effects on the *IV* traces are comparable. For both theories, the energies for the current onset shift to lower values and the step-like behavior morphs into a peak like structure, when including magnetic effects. The formation of peaks is no intrinsic property of magnetic contacts, but also present in proximitized contacts

³In their publication also Andreev bound states and a Josephson current for non-zero phase difference is calculated [ACF02]. In the present work it is not possible to apply any phase difference, hence, this case will not be explained.

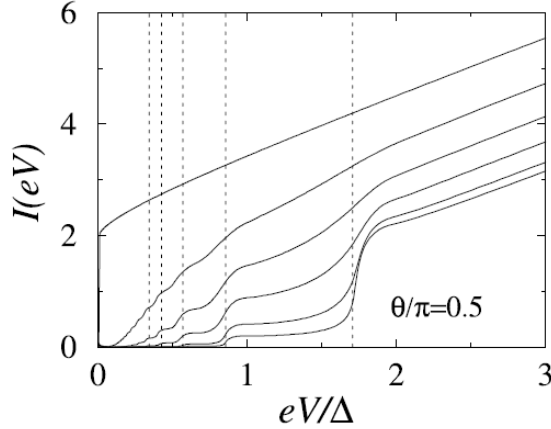


Figure 4.4: IV curves for the transparencies $D = 1.0, 0.8, 0.6, 0.4, 0.2, 0.1$ (from top to bottom) for a spin-mixing angle of $\Theta = \pi/2$ calculated with the theory by Andersson *et al.* Taken from [ACF02].

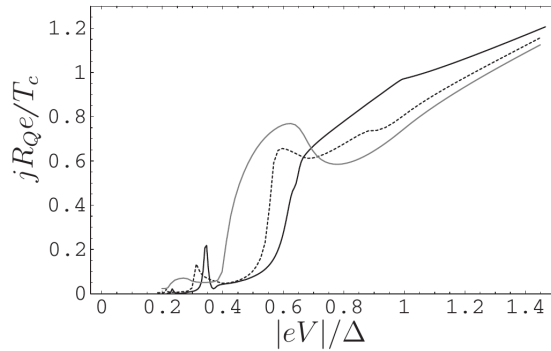


Figure 4.5: The combination of spin-filtering and spin-mixing leads to complex subgap features. The presented curves are calculated for $T = 0$, $T_\uparrow = 1$, $T_\downarrow = 0.1$ and $\Theta = 0, \pi/4, \pi/2$ (solid, dotted and solid gray line). Current and voltage are given in reduced units. Taken from [BB07].

(cf. [Sch+02]).

Calculations which include both aspects are more interesting, since both effects can occur. These calculations have been performed by Bobkova *et al.* In a first paper the results are limited to low transparencies, which make a experimental implementation difficult [Bob06]. But in a follow up paper, they also deal with high transparencies as well as increased temperature [BB07]. Due to the complexity of the problem, only selected cases are presented. In figure 4.5 one combination of spin-filtering and spin-mixing from the article is presented. With increasing spin-mixing, the peaks get broadened and the current onsets shift to lower energies. A general trend or easy description of the calculated curves is not possible anymore, but they feature the same trend as the simplified calculations by Martín-Rodero *et al.* and Andersson *et al.*

4.2 Sample Preparation

The aim of the sample preparation is to produce samples in which the actual break junction, meaning the constriction, consists of the metal of interest. However, the leads should be made of a superconductor to make the constriction superconducting through the inverse proximity effect. To ensure that the whole constriction and, therefore, the atomic contact is superconducting, a small gap between the superconducting leads is required. But there must not be a direct connection within the superconductor. To achieve this, first test structures demonstrate a reproducible gap size of 20 nm in a metal film (in this case aluminium) on polyimide. In principle, there are two different possibilities for the lithography. The first one is shadow evaporation, which was already used in [Sch+01] to measure atomic gold contacts and is described in [section 4.2.1](#). The second method is the usage of multiple lithography steps to arrange the different metal films in the right alignment to each other. This method is described in [section 4.2.2](#). The principle process for both methods is similar to the one already described in [section 3.2.1](#). Here, I will focus on the differences and difficulties. Both methods have their pros and cons which are discussed in the particular sections.

4.2.1 Shadow Evaporation

The shadow evaporation was already used by Scheer *et al.* to measure the channel configuration of atomic gold contacts [Sch+01]. The samples are designed similar to the one described for the noise measurements in [section 3.2.1](#). The main difference is a gap inside the constriction. This gap is designed to be 25 nm to 40 nm wide, which is limited by the used resist. For this resolution, I used a 950 PMMA A2 on top of a 600 nm thick MMA-MAA EL11, both by MicroChemicals. The layout of the constriction area is shown in [figure 4.6 a\)](#). To fill this gap the sample is evaporated at different angles along the sample axis. Here, three different angles, as indicated in [figure 4.6 b\)](#), are used. The aluminium is evaporated perpendicular to the sample surface and the palladium is evaporated in two consecutive steps with an angle of $\pm 8^\circ$ with respect to the normal. A rendered picture of a perfect structure is shown in [figure 4.6 c\)](#). A SEM picture of the sample, made of aluminium and palladium, is shown in [figure 4.6 d\)](#). Two additional samples are depicted in [figure 4.17](#). Using this procedure one achieves a constriction made of one metal and the leads made of another metal.

For the first samples made with this technique, I used gold and aluminium in both orders (Au-Al and Al-Au). Due to the different heights of the metals, only the order Au-Al produces conductive samples. These samples have been used as reference samples, the results are discussed in [section 4.4.2](#). The sample preparation with the desired combination aluminium and palladium was more unreliable. The favorable order, first palladium and then

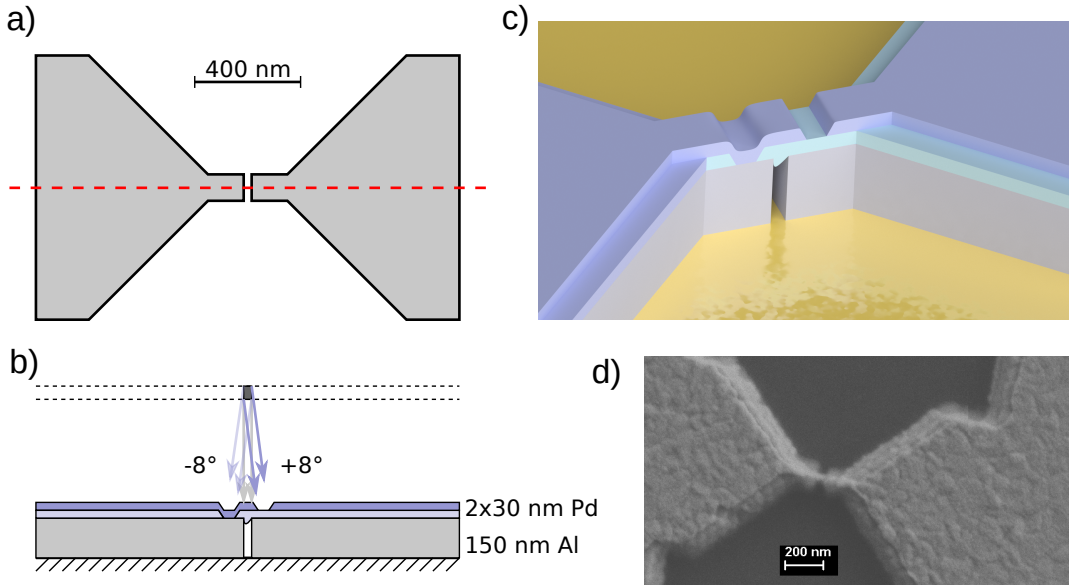


Figure 4.6: **a)** The layout of the mask for the inner part of the constriction, including the gap with variable width is shown. The red dashed line indicates the position of the cut in **b)** showing the cross-section through the constriction area, including the angles for the shadow evaporation and the resolved structure. **c)** A artistic representation of the finished constriction: The two layers of palladium are indicated with different colors. **d)** A SEM picture of the produced structure of sample 29-II-10, discussed in section 4.4.3.

aluminium, was not possible, since the palladium film has intrinsic strain. This strain destroys the small resist bridge, which should form the gap between the aluminium leads. The other layer order leads to the problem, that the thin palladium films < 25 nm did not lead to continuous metal film over the thick aluminium step. Therefore, the thickness of the film was increased to 40 nm. This leads to working samples, but due to the high amount of palladium on top of the superconducting aluminium, the superconducting properties are reduced. This behavior is described in detail in section 4.4.3. To improve these properties again, one should decrease the amount of normal conducting metal on top of the superconductor. One possibility is a multi-step lithography, which is described in the next section.

4.2.2 Multi-Step Lithography

The second method to produce samples with different metals in different shapes is to carry out multiple consecutive lithography steps. To this end, one performs one step, consisting of lithography, development, evaporation and lift-off. To add another step afterwards, one has to apply another coat of resist. In this case we used three steps of e-beam lithography. To

achieve the desired resolution, a 950 PMMA A2 on top of a thin spun MAA-MMA EL11 was used in the second and third step.

Similar to the shadow evaporation two different layer orders are possible. The preferred order would be first the palladium, and the aluminium on top. This attempt was tried first and is discussed in the next paragraph. The other order, depositing first the aluminium and then the palladium on top, is discussed afterwards.

Multi-Step Lithography: Palladium – Aluminium

There are two reasons going for this layer order: First, the palladium does not form oxides at room temperature, in contrast to aluminium, which forms a native oxide barrier of about 5 nm thickness. The second reason is the thickness of the metals. One expects no contact problems if a thick metal is evaporated on top of a thin one. The other way round, one may run into problems due to the shadowing effect of the first layer.

Because of the thin layer and moderate density of palladium, the alignment markers were hardly visible below the resist. Therefore, another step before patterning the palladium was introduced. This step creates the markers made of 80 nm gold on the sample. Some considerations of also making parts of the leads out of gold have been rejected after some tests, which led to unreliable contact between gold and aluminium.

After some dose tests, it became clear, that with the standard 10 kV lithography the structures are extremely sensitive to the dose and, therefore, unreliable. Even on the same chip with the same dose one gets totally underexposed and totally overexposed structures side by side. Hence, I switched to 30 kV, which makes it impossible to see the contamination dots on the resist for focusing the electron beam. Thus, a focusing sample was produced and used to adjust the focus of the electron beam accurately.

All these improvements lead to the following three steps:

1. Markers: 80 nm gold (MAA-MMA EL11 and 950 PMMA A4; 10kV),
2. Constriction: 20 nm to 40 nm palladium (MAA-MMA EL11 and 950 PMMA A2; 10kV) and
3. Leads: \geq 150 nm aluminium (MAA-MMA EL11 and 950 PMMA A2; 30kV).

The thickness of the gold layer was mainly needed for the visibility of the markers, especially at the high acceleration voltages up to 30 kV. The palladium layer should be thin to reduce the influence of the inverse proximity effect on the superconducting properties. The resist system should be thin for good visibility of the markers. Therefore, the copolymer and the PMMA were spun at 5000 rpm in two consecutive steps. The aluminium, instead, should be thick enough not to be influenced by the underlying palladium. Here thicknesses in excess

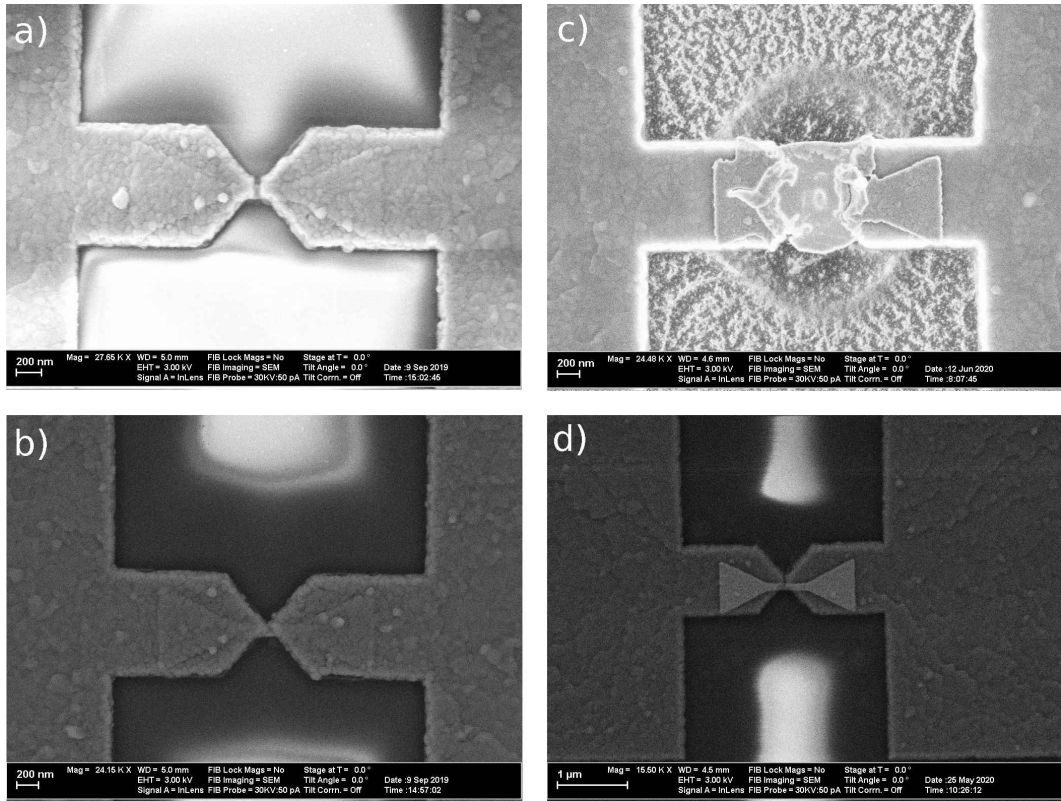


Figure 4.7: SEM pictures of four samples produced with multi-step lithography. **a)** and **b)**: Two samples with the order palladium – aluminium. The palladium is only visible as a shallow structure below the aluminium. The gap in **a)** was measured at 52 nm, but the sample was not conducting. The sample shown in **b)** was measured in the setup, the results are discussed in section 4.4.4. **c)** and **d)**: Samples produced with the order aluminium – palladium. The sample in **c)** shows damage produced by an electric discharge, which probably happened during the second lithography step. Parts of the aluminium are deformed and a circular part of the resist has been exposed or even disrupted. An example for a good looking, but not conducting sample is given in **d)**.

of 180 nm have been tried, but due to the small thickness of the copolymer problems during lift-off appeared. Additionally, the gap between the aluminium leads vanished.

Many samples have been produced using this recipe. Two SEM pictures of well formed samples are shown in figure 4.7 a)-b). Some of them were cooled down, but all of them seemed to have formed the atomic contacts within the aluminium. One sample, showing interesting features leading to proximity superconductivity, is discussed in section 4.4.4. One of the main issues with these samples is the remaining problem while focusing, even with the focusing aid next to the sample, the structures are not reproducible due to focus problems. Therefore, the reverse process, putting first the aluminium and then the palladium was tried. The exact conditions are given in the next paragraph.

Multi-Step Lithography: Aluminium – Palladium

The idea of this order has two reasons: First the separation of the aluminium leads is the critical point in this sample preparation. If it is too large, the superconducting properties are suppressed, if it is too small, the gap is filled with aluminium leading to an aluminium atomic contact. The second reason is, that the exact shape of the palladium does not matter too much, hence it is possible to increase the dose a bit resulting in a more reliable constriction. Additionally, one can change the resist system for the last step, since only a small amount of metal is evaporated onto the sample. Luckily this allows to replace the markers in gold by ones made of aluminium, eliminating one lithography step. The two steps for these samples are:

1. Aluminium: main structure and markers (175 nm; MAA-MMA EL11 and 950 PMMA A2; 10kV) and
2. Palladium: constriction (20 nm to 40 nm; MAA-MMA EL6 and 950 PMMA A2; 10kV).

These two steps allow for a faster sample preparation as well as a good focus for both steps. But also this process has its challenges. The copolymer of the second step varies in thickness over the sample leading to lift-off problems. Probably this problem is caused by the low viscosity of the copolymer and the small chip size. Letting the copolymer and also the PMMA rest for 30 s before spinning, limits that problem to the edges. Another problem, that occurred regularly during the sample preparation, is generated by electric discharges inside the gap. This leads to a big roundish palladium disk bridging the aluminium as shown in figure 4.7 c). Sometimes also parts of the aluminium are destroyed due to that discharge.

Beside this problem, even samples which look good in the SEM (cf. figure 4.7 d)), do not conduct. The exact reason for this problem could not be resolved so far. Either the palladium is not continuous at the edge of the aluminium or there is a thin oxide barrier between the aluminium and the palladium. Possible oxide barriers are the native oxide of aluminium, residues of the resist system or an isolating alloy of aluminium and palladium. The latter is not very likely, since literature [HO85] does not report it and test samples with big interfaces between aluminium and palladium are not isolating. But these test samples have an overlap area of $5\text{ }\mu\text{m} \times 20\text{ }\mu\text{m}$, which is much bigger than in the original samples. Therefore, the possibility of conductive pinholes in the native oxide of aluminium or in the residue resist layer is enhanced.

4.3 The Setup

In this section first the cooling system ([section 4.3.1](#)) and then the mechanical setup for the breaking mechanics ([section 4.3.2](#)) are briefly described, followed by the cabling ([section 4.3.3](#)) as well as the devices used for the measurement ([section 4.3.4](#)). The last paragraph will briefly sketch a typical measurement procedure ([section 4.3.5](#)).

4.3.1 The Cooling System

For measuring superconductivity, one needs low temperatures. To exclude thermal rounding of the features in the *IVs* one tries to measure below a tenth of the critical temperature T_c of the sample. Using aluminium as a superconductor with $T_c \approx 1.2\text{ K}$ one wants to reach temperatures below 100 mK. Additionally, one assumes, that the critical temperature of proximitized metals is even lower. The only way to get these low temperatures is using a dilution refrigerator. For this experiment a commercial dilution refrigerator LD-400 by BlueFors is used [[BF13](#)]. The working principle of dilution refrigerators is explained in many textbooks (e.g. [[Pob96](#)]). The LD-400 uses a pulse tube for precooling the system to about 4 K and is equipped with a superconducting magnet up to 7 T from American Magnetics, Inc. The base temperature of the system was 7 mK without breaking mechanics and wiring. After adding them, the base temperature was measured to be 10 mK to 12 mK. This temperature is well below a tenth of T_c and, therefore, one expects sharp superconducting *IV* characteristics.

To understand the following sections better, I will introduce the main parts of the cryostat. The 60 K and the 4 K stage are cooled by a pulse tube and provide cooling power for the magnet and the dilution system. In the Still the ^3He is evaporated from one phase. The provided cooling power is used to condense the incoming gas (in continuous operation mainly ^3He) and works at a temperature of 700 mK to 900 mK. Mounted to the heat exchangers below the Still is the Cold Plate (CP). This is a good place to thermalize different parts. The CP is at a temperature of about 200 mK. The coldest part of the system is the mixing chamber (MXC) at the base temperature of 10 mK.

4.3.2 Breaking Mechanics

For the BF-LD400 a new breaking mechanics was developed. This mechanics is described here. To reduce the heat load to the MXC, the driving rod has to be coupled to the different stages of the system. For better decoupling, from room temperature to the MXC, I decided to

mechanically interrupt the driving rod. Therefore, I use four gearboxes with a transmission of 3.1:1. These gearboxes are commercial ones by Faulhaber⁴ which were tested to run at low temperature without any lubrication. The lubricant, which was originally in the gear, was removed with acetone prior to mounting them on the 60 K-plate, 4 K-plate, the Still, and the MXC. The gears are connected with stainless-steel tubes with a diameter of 4 mm and a wall thickness of 0.1 mm. At the upper end a plug is soldered into the tube, to connect it to the gear using a bushing. To the lower end the socket for a cog and the cog itself are soldered. This cog reaches into the next (lower) gear.

The mechanics is driven by a DC motor⁵ outside the cryostat. The movement is fed into the vacuum by a feedthrough of Pfeiffer⁶. The connection to the uppermost driving rod is implemented via a bellow⁷, which eliminates tiny misalignment due to the rubber seal at the feedthrough.

Below the MXC, the actual breaking mechanics is installed to reach into the center field of the superconducting magnet. This mechanics has been designed by A. Fischer and myself. It was realized by the workshop of the university. Due to a second experiment installed in the cryostat and reaching into the magnet bore, the available space was limited to a 40 mm diameter. Therefore, we opted for a differential screw conversion from circular to linear motion. The linear motion drives a pushing rod made of copper, which bends the sample. The pushing rod is guided in a bronze part using five sapphire balls with a diameter of 2 mm. A 3D view of the mechanics is shown in figure 4.8.

4.3.3 Wiring and Filters

The wiring inside the cryostat has to fulfill two purposes. The first is to conduct only little heat from room temperature (RT) to the sample. The second is to filter high frequency components of the electrical signals. The whole wiring concept inside the cryostat is depicted in figure 4.9. For the measurement of the sample, three pairs are used. One for biasing the

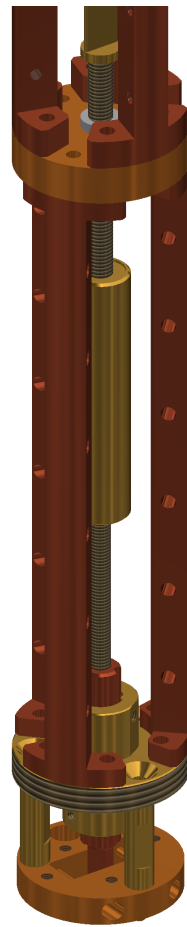


Figure 4.8: 3D view of the lower part of the breaking mechanics.

⁴Faulhaber Spur Gearhead Series 22/2 with ball bearing

⁵Faulhaber DC-Micromotor 2232R024SR with a 97.3:1 Spur Gearhead

⁶Pfeiffer Vacuum DD 016 A, rotary feedthrough, DN 16 ISO-KF

⁷GMT GLOBAL INC. Full stainless steel bellows coupling with set screw; FSMB16-4-5

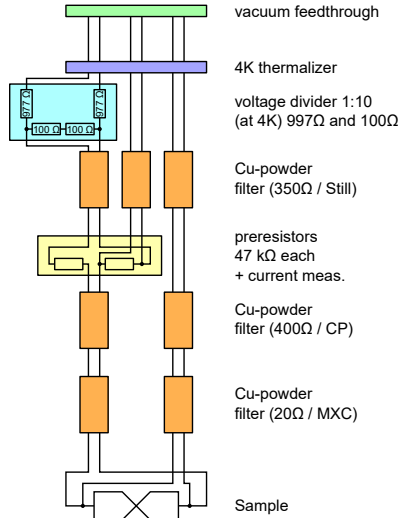


Figure 4.9: Schematic of the wiring inside the cryostat: The individual components are labeled with their resistances. The wiring is realized in twisted pairs, for better visibility they are shown as parallel lines. From RT to the 4 K-plate simple shielded twisted pairs are used. From there to the MXC twisted pairs inside of a capillary filled with EccoShield (see text) are used. Two additional passive components are used. One is a 1:10 voltage divider at 4 K. This is used to reduce noise and parasitic signals as well as allowing higher voltages outside the cryostat in the bias lines. At the Still the two $47\text{ k}\Omega$ resistors in the bias line provide a current bias instead of a voltage bias. One of them is also used for the current measurement. At different temperatures copper powder filters are included to filter high-frequency noise and thermalize the wires.

sample, one for the current measurement, and one for the voltage measurement across the sample depicted left, middle, and right in figure 4.9 respectively.

The big temperature difference between room temperature and 4 K is bridged with commercial twisted pair cabling⁸. These cables are thermalized at 60 K and 4 K. At 4 K also a passive voltage divider with a 1:10 ratio is built in to reduce noise and to allow for bigger signals in the bias line outside the cryostat. From there on, home-built twisted pairs in stainless steel tubes filled with EccoShield⁹ are used. These capillary wires provide a good attenuation above 1 GHz [Tha+17]. For additional filtering and thermalization of the lines, copper powder filters are used at the Still, the Cold Plate, and the Mixing Chamber. Information about the filtering properties and thermalization can be found in [Tha+17; Lor18]. The additional π -filters, as used by Lorenz [Lor18], together with the voltage divider and the preresistors created a strong filtering effect down to 1 kHz. Since this affected the signal of the lock-in amplifier, they were exchanged by some copper powder filters with high resistivity Manganin¹⁰ wires. At the Still, two resistors with $47\text{ k}\Omega$ are mounted into the bias line. They are used to convert the voltage bias provided outside the cryostat into a current bias. One of them is also used to measure the current through the sample via the voltage drop over it. To implement the voltage to current conversion correctly, the temperature dependence of this resistor was measured in a 4-point configuration.

⁸GVL Cryoengineering: Low Temperature Coax Cable - Twisted Pair - Brass, CuNi shield

⁹EccoShield ES 100 GR (ES) from Emerson & Cuming Microwave Ltd.

¹⁰50 μm diameter, 220 Ω/m

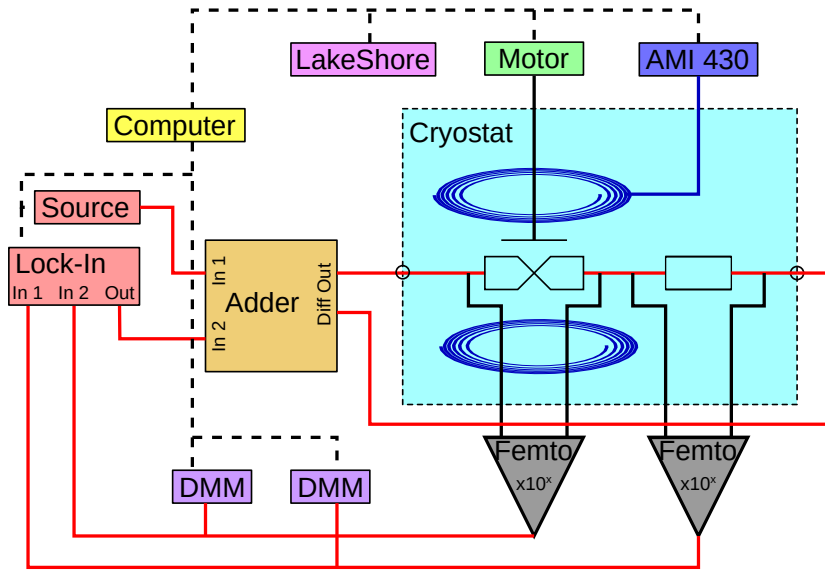


Figure 4.10: In this schematic all measurement devices are depicted. The cabling inside the cryostat is shown in a simplified way. All devices are described in the text.

4.3.4 Measurement Electronics

In this paragraph the measurement electronics and how it is used is described. All devices are depicted in [figure 4.10](#) and will be described in the following. Some of the devices only serve for controlling the state of the sample. These include the motor controller¹¹, the temperature controller¹², and the magnet power supply¹³. They are connected via a serial adapter or Ethernet to the computer.

More effort was dedicated to the electronics for measuring the signal of the sample. Here, only the parts outside the cryostat are described. For the filtering and thermalization concept please see [section 4.3.3](#). One can split the measurement devices into a DC part and an AC part. The AC part is used for dI/dV measurements using a commercial lock-in amplifier¹⁴. The DC voltage is supplied by a low-noise power source¹⁵. This signal is filtered by a low-pass filter to reduce the parasitic chirp noise from the supply. This noise and the filter is described in [appendix A.2.2](#). The DC voltage and the reference signal are added in a home-built adder described in [appendix A.2.1](#). There, the AC voltage of the lock-in is high-

¹¹Faulhaber Motion Controller MCDC 3002 S

¹²LakeShore Model 370

¹³American Magnetics Inc. Model 430 Power Supply Programmer

¹⁴Zurich Instruments HF2

¹⁵Agilent B2962A

pass filtered and attenuated by 20 dB. The added voltages are fed to the cryostat. The output may be shorted, to measure the amplifier offsets, by applying 5 V to an auxiliary input. Inside the cryostat, the voltage over the sample and the voltage over a $47\text{ k}\Omega$ resistor are picked up. The voltage over the resistor is used to measure the current. Both voltages are amplified by voltage amplifiers¹⁶. The DC part of the amplified voltages is measured with a digital multimeter¹⁷. The AC part is first high pass filtered¹⁸ and then fed to the lock-in amplifier. All devices are connected via USB to the computer. The power source and the multimeters use an isolated USB interface. The lock-in connects the analog ground with the USB ground. For decoupling these two potentials (avoiding ground loops), a ground lift¹⁹ and a USB cable with disconnected shield is used. For the grounding scheme of the lock-in, please refer to [Zur18, p. 621].

4.3.5 Measurement Procedure and Data Storage

The measurement procedure is built up in different stages. After cooldown to 4 K, the sample is checked regarding the metal building the atomic contact by performing one or more histogram measurements. This step is necessary, since the first opening needs a lot of bending, which generates too much heat for the mixing system to cope with. Additionally, one is able to separate samples which break in the palladium region, from those breaking in the aluminium. The latter is unwanted and, therefore, these samples not investigated further.

If the sample shows a clean histogram with no peaks below 1 G_0 , meaning no aluminium in the contact, the sample is closed to below $100\text{ }\Omega$ and the system is cooled to lower temperature. While condensing, the resistance and the temperature are monitored to extract the critical temperature T_c . After reaching base temperature, the critical field B_c is examined. The critical current I_c is often not available, since the preresistors with nearly $100\text{ k}\Omega$ in the cold state, and the voltage divider limit the maximum current in the system to about $10\text{ }\mu\text{A}$. Then the sample is opened to a tunnel contact in the $100\text{ k}\Omega$ to $200\text{ k}\Omega$ regime to measure the superconducting gap Δ .

After these characterization measurements, contacts are established repeatedly in a magnetic field $B > B_c$, by opening (and closing) the break junction. The magnetic field is necessary to exclude superconducting effects while establishing a contact. A contact is classified as stable and good if the conductance lies in the desired range ($\approx 0.2\text{ G}_0 - 3\text{ G}_0$) and its resistance changes by less than 10 % while letting the system cool down. Depending on the desired action, at each contact dI/dV , magnetic field sweep, or even BIV measurements are performed.

¹⁶Femto DLPVA with true differential input

¹⁷Keysight DMM 34461A

¹⁸passive RC filters with $f_c = 82.9\text{ Hz}$

¹⁹Range Extender

In the simplest case only two dI/dV traces are recorded, one with increasing and one with decreasing bias voltage.

In the second case, the magnetic field is ramped in a saw-tooth like shape. The measurement starts at zero field, goes to $-B_{\max}, B_{\max}, -B_{\max}$, and back to zero field. This sequence allows to differentiate between history-dependent and asymmetric features in the traces. The maximum field B_{\max} depends on the measurements, often $B_{\max} > B_c$ is chosen to check for changes in the exact critical field. In rare cases B_{\max} is chosen in the order of several Tesla to check for similarities with the findings of Strigl *et al.* [Str+16]. But since these features start at 5 T and the maximum field rate is limited to 0.1 T/min the measurements take a long time. For each magnetic sweep, dI/dV traces are collected before and after the magnetic sweep to double check for changes.

The third possibility, the so called BIV maps, perform dI/dV measurements at certain fields, to study the effects of the magnetic field on the contacts. This measurement scheme requires a lot of time due to cooling times and the many collected dI/dVs . The cooling times between the dI/dVs are necessary, since the changing the magnetic field heats up the system slightly.

All data is gathered by LabVIEW programs and saved in TDMS files. Each file contains multiple groups named for the part of the measurement, which it contains. Depending on the measurement mode, one file contains only a single contact or many contacts. Single contacts in a file are often measurements with magnetic sweep or BIV or even both of them. Data of multiple contacts in one file are stored if only dI/dVs are recorded for each contact. This might be of interest, to check the influence of the exact contact parameters on the superconducting features.

4.3.6 Fitting Procedure of the Superconducting IV Curves

To extract the exact channel configuration from the measured *IV* curves, a special analysis scheme was used. This paragraph is divided into two parts: First the preparation of the data for the fitting is described and then the actual fitting to the theory will be explained.

For each contact, two *IV* curves have been recorded, one with increasing bias and one with decreasing bias. To decrease the noise, the current I is binned to fixed voltage values. These fixed voltage values are calculated by 1000 equally spaced points between -5Δ and 5Δ . Then, the current values are defined at the same sampling points on the voltage axis, so that it is possible to derive the mean value between increasing and decreasing bias.

Then, the *IV* curve is checked for point-symmetry with respect to $(0|0)$. This is important since the hardware offsets leave a small, but finite shift in the curves. This shift influences the fitting procedure and has to be eliminated. A residual offset in the voltage might be found by checking the position of the peaks in the dI/dV for symmetry around 0 V. If one has not

recorded the dI/dV , a numerical dI/dV is calculated. After removing the shift in V , the shift in I is removed. To do so, one assumes again the symmetry around $I = 0A$. The shift in I is set to the mean value of the current between -1.5Δ and 1.5Δ . Now one has an offset-corrected IV curve. For contacts with one channel close to transmission $\tau = 1$, this leads to wrong shifts in some cases. So, each curve is checked for correctness and may be corrected by hand.

For each curve the conductance of the contact is determined by using a linear fit for $V > 1\text{mV}$. Using a voltage well above 2Δ ensures the absence of any non-linearities caused by superconductivity. The conductance is important as a starting point for the fitting in later stages of the analysis and as a measure for the sum of all transmissions. All ingredients are now available to start the actual fitting.

Prior to the fitting, one has to generate the theoretical IV curves for a single channel with a specific transmission. This is done using a FORTRAN script written by Cuevas [CMY96]. For the analysis, the calculations were done at zero temperature and for transmissions from 0 to 1 in steps of 0.001. The script creates a file for each transmission containing an IV curve from 0V to 5.5Δ .

The fitting is done using a Monte Carlo approach. To this end, one generates a random set of transmissions with $[3G + 3]$ independent channels. The sum of the transmissions is coerced to the interval $[0.9G, 1.1G]$ for speeding up the fitting. Then, the resulting IV curve is calculated using the previously calculated transmission files. This theory curve is compared to the measured IV by calculating the least squares between the two curves. Then, a random change in the transmissions is done and after coercing to the normal conducting conductance, the curves are compared again. If the difference is less than in the step before, it is accepted, otherwise it is rejected with a probability of $1 - \alpha$. α is a small number, which allows totally new configurations. The whole fitting procedure is terminated, if the difference between the calculated and the measured curve is small enough or 10^6 iterations are complete.

Since the positive and the negative branch contain the same information, each IV curve is cut in two halves and the calculations are performed twice, one time for each branch. The outcomes of the two calculations are compared and if, the sum of the transmission or one transmission differ by more than 5 %, the whole process is repeated with a increased number of channels. As a last check, the calculated and the measured curves are plotted for both branches and compared for consistency. If everything matches, one probable configuration for the channel transmissions of that contact is found.

4.4 Results

The results of the measurements of the superconducting samples are presented for each material separately. First, the setup was checked with the BCS superconductor aluminium ([section 4.4.1](#)) and proximitized gold ([section 4.4.2](#)). Both, aluminium and gold, lead to smaller changes of the setup. Then the system of interest, proximitized palladium, is presented. First, the results of the samples made by shadow evaporation ([section 4.4.3](#)) and in [section 4.4.4](#) the results of the samples produced with multi-step lithography are shown. An overview over all measurements is given in [table 4.1](#).

sample ID	materials	fabrication method	comment
Al_31-II-06	Al	-	without chirp filter
Al_23-I-11	Al	-	
AlAu_29-I-09	Al, Au	shadow	
AlAu_29-I-14	Al, Au	shadow	
PdAl_29-II-10	Al,Pd	shadow	good measurement
PdAl_29-II-13	Al,Pd	shadow	only cooldown
PdAl_30-II-18	Au, Al, Pd	multi-step litho	

Table 4.1: Overview over the different measured samples investigating the multiple Andreev reflections.

4.4.1 Aluminium

To check the filtering and thermalization concept, as well as the fitting procedure, two samples made of aluminium were measured. The first sample was measured without the chirp filter described in [appendix A.2.2](#) leading to rounded spectra. Therefore, this sample Al_31-II-06 will not be discussed in detail. Before measuring atomic contacts, the critical field, critical temperature, and a histogram were recorded. The results of these measurements are depicted in [figure 4.11](#). All measured magnetic traces are asymmetric with respect to 0 T of the power supply. This behavior was investigated in detail and is discussed in [appendix A.2.3](#). For all following measurements, this fact is taken into account and the magnetic field is shifted accordingly. For aluminium, one gets a peak in conductance at $0.7 G_0$, which is in good agreement with other measurements [YR97; Sch10]. The two key features to check with a closed sample are the critical temperature T_c and the critical field B_c . For both samples $T_c \approx 1.21\text{ K}$. This value is slightly higher than the bulk value $T_c^{\text{bulk}} = 1.18\text{ K}$ [BR04], but inside the reported span of T_c . The transition shows a plateau at around $70\text{ }\Omega$. B_c is not the same for the two samples. Al_23-I-11 has $B_c = 10.4\text{ mT}$ and for Al_31-II-06 one gets only 8 mT , which is a bit lower than the bulk $B_c^{\text{bulk}} \approx 10\text{ mT}$ [Eis54]. The superconducting gap was measured to be $\Delta = 181\mu\text{eV}$,

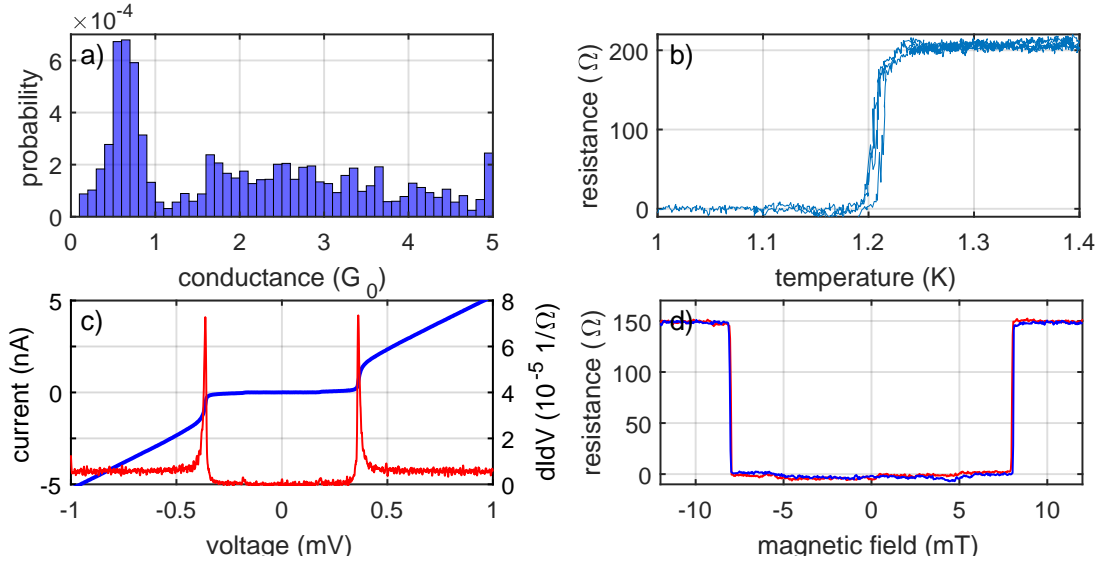


Figure 4.11: Overview over the pre-measurements of the aluminium samples: A histogram is depicted in a) showing a clear peak at $0.7 G_0$. The measurements of T_c b) and B_c d) show a steep transition at 1.21 K and 8 mT . The temperature measurement consists of one heating and one cooling curve revealing a small hysteresis and an intermediate state with $\approx 70\ \Omega$. The tunnel spectrum shown in c) reveals a BCS like gap with coherence peaks at $2\Delta = 362\ \mu\text{eV}$. Additionally, one can resolve a tiny peak at $\Delta = 181\ \mu\text{eV}$.

which is the known gap for aluminium [GM12]. All this indicates clean superconductivity, at least for the sample Al_23-I-11, where atomic contacts were measured.

In the following, only the results of the sample Al_23-I-11 are discussed, since the other sample did not show full critical field and was measured without the filtered output of the voltage source. Over 200 contacts were measured in the interval $0.5 G_0$ to $2.3 G_0$ and were analyzed with the method described in section 4.3.6. The IVs of four contacts and the corresponding channel configurations are shown in figure 4.12. These contacts are taken from the whole conductance range and show good agreement between experiment and theory. For better visibility, the voltage as well as the current is normalized to the gap and the conductance in the normal-conducting regime. For single-atom contacts one normally finds three contributing channels. This is in good agreement with measurements by Scheer *et al.* who also found three contributing channels for aluminium [Sch+97]. The fitting procedure becomes more complicated for contacts above $2 G_0$, since they have at least one rather high transmitting channel, which makes the IVs rather featureless. One contact, where this is the case, is curve (a) in figure 4.12. These contacts also reveal more than three or four contributing channels. The contact (a) needs at least four channels to be described. All these contacts also show non-linearities in the superconducting IV curves, which are bit broadened as a result of the ac-excitation of the lock-in amplifier.

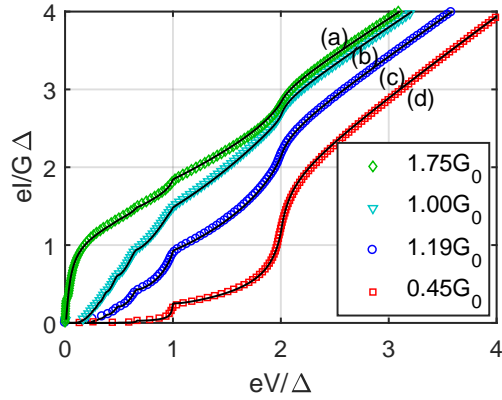


Figure 4.12: The positive branch of four *IV* curves with different conductance showing MAR in aluminium are depicted. The symbols are the experimental data and the lines are the best fits to the experiment, using the theory of Cuevas *et al.* [CMY96]. The corresponding transmissions of channels are: □: 0.22, 0.20, 0.03; ○: 0.68, 0.30, 0.19, 0.02; ▼: 0.78, 0.09, 0.07, 0.06; ◇: 0.99, 0.44, 0.27, 0.05.

The results demonstrate that both, the experimental setup, as well as the fitting procedure, are usable to determine the exact channel configuration of atomic contacts. Thus, a next step is to measure proximitized junctions made of a normal metal without any magnetic moment in the constriction. One standard metal, which is already well understood, is gold.

4.4.2 Proximity Superconductivity: Aluminium and Gold

Since the proximity effect will have an influence on the superconducting parameters, B_c , T_c and Δ , it is worth checking the setup with a normal metal without any magnetic moment in the constriction. This also serves as a reference, that the obtained results for the proximitized palladium are not only a result of the proximity effect. The metal of choice is gold, which is well understood and reveals a single conducting channel [Sch+01]. Two samples produced by shadow evaporation have been measured. The thicknesses are 130 nm aluminium and 2×10 nm gold and 125 nm aluminium and 2×12 nm gold, respectively. The results are discussed in two separate sections, since the superconducting properties differ a bit for the two samples.

AlAu_29-I-09

An overview over the properties of the first proximity sample (AlAu_29-I-09) is shown in figure 4.13. The histogram shows a clear peak at $1 G_0$ with a smaller peak at $0.7 G_0$, which often arises from disordered contacts. The second maximum is around $1.9 G_0$, a common value

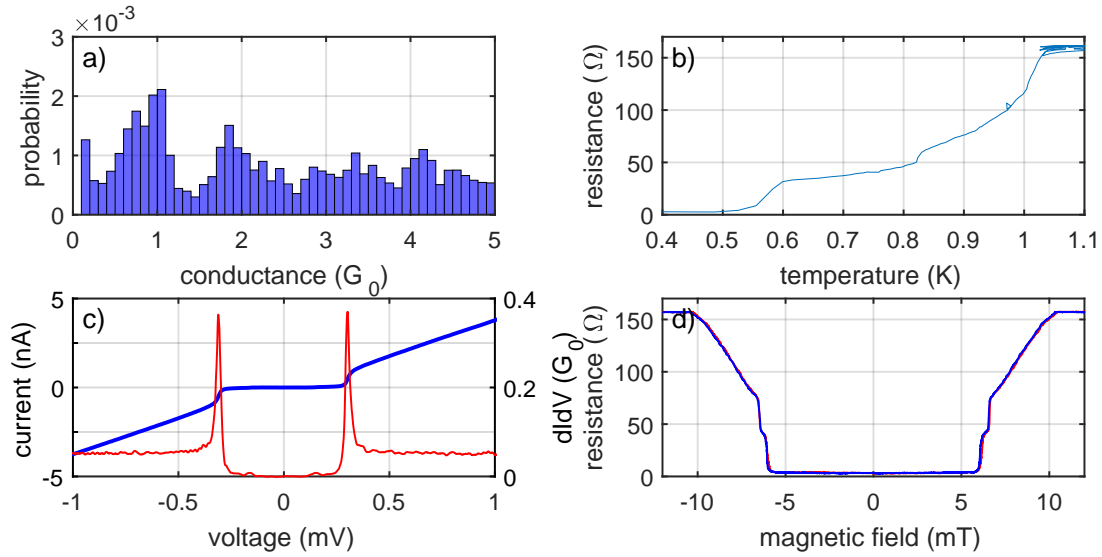


Figure 4.13: Overview over the properties of sample AlAu_29-I-09: The histogram is shown in a), and has a first maximum at $1 G_0$. One tunnel contact is shown in c) and has a gap of $153 \mu\text{eV}$. Both the critical temperature b) and the critical field d) reveal multiple transitions at different values. These transitions might refer to different parts of the sample, like the constriction or the leads. The details are described in the text.

for gold. This histogram is built up from opening traces. In the corresponding histogram of the closing traces the peak at $0.7 G_0$ is missing. These histograms have been recorded at 4 K. So one may conclude, that the sample forms the atomic contacts inside the gold. One has clear suppression of the superconducting properties like the critical temperature T_c and the critical field B_c . These two show multiple steps and continuous transitions. The lowest one at 0.56 K and 6.06 mT, respectively. These values are both well below the bulk values for aluminium, which is an indication for proximity superconductivity. The gap has been measured with a tunneling contact and is determined to be $\Delta = 153 \mu\text{eV}$. Also that value is below the bulk value of aluminium. But the coherence peaks are a factor of 7.5 higher than the conductance far outside the gap, which one can interpret as an indication for well formed proximity superconductivity.

Due to the already mentioned chirp noise (appendix A.2.2), the spectra are rounded, which makes the fitting challenging. Nonetheless, four contacts and the corresponding fits are shown in figure 4.14 a). The deviation between the theory and experiment remains clearly visible, especially for the low voltage regime. After adding the filter, the features got more pronounced and the fits agree better with the experimental data. Three curves with similar conductances as without the filter are shown in figure 4.14 b). The remaining broadening is caused by the proximity effect. Both, measurements with and without the filter, show mainly one to two partially open channels. This is a known feature of the monovalent metal gold

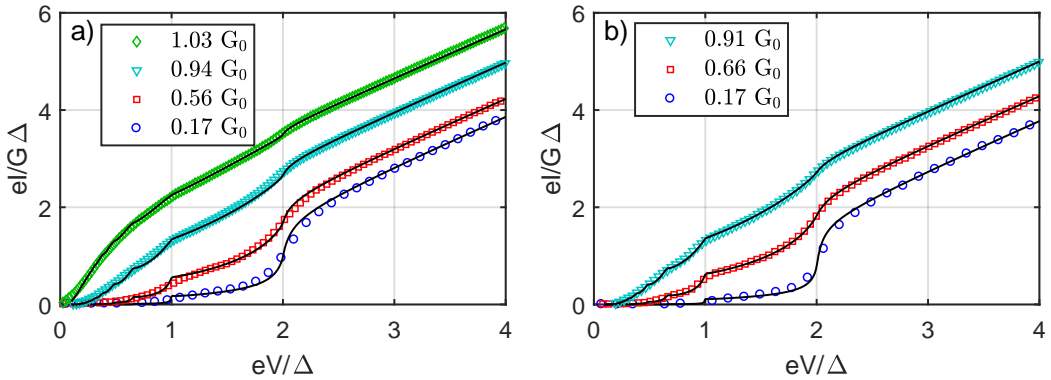


Figure 4.14: Different contacts of the sample AlAu_29-I-09 without **a)** and with **b)** the chirp noise filter: The traces without the filter show rounded features, which are prominent for the $0.94 G_0$ (black triangular) and the $0.56 G_0$ (red square) traces. Traces with similar conductances are sharper with the filter. The transmissions for the curves with filter are \circ : 0.12, 0.04, 0; \square : 0.47, 0.17, 0; \triangledown : 0.72, 0.18, 0.

[Sch+01].

The software for the *IV* curves applied a voltage bias with the same voltage span for each contact. This leads, caused by the the preresistors, to a difference in voltage drop over the sample and, therefore, the number of data points per traces varies. Since the number of usable points is low for tunnel-like contacts, the software was changed after that sample to keep the number of data points per *IV* curve constant.

AlAu_29-I-14

This sample was cooled down to the base temperature before breaking it. Thus, the resistance of the sample in the non-broken, normal-conducting state is only $\approx 5\Omega$. The results of the measurements for determine the critical temperature and field are shown in figure 4.15. T_c reveal a broad transition range of 1.02 K to 1.12 K. This range is caused by the fact, that T_c was measured while condensing the mixture. The condensing is done in a pulsed way, so that the temperature is oscillating rather quickly, which leads to a hysteresis between cooling down and heating up. The critical field B_c shows two transitions, one continuous transition in the region 8.74 mT to 9.76 mT and a step at 6.88 mT. These two fields correspond to two different parts of the sample, most probably the leads and the constriction. Both measurements show a residual resistance of 2Ω , which comes from the copper wires for contacting the sample.

The first histogram, depicted in blue in figure 4.15, shows a maximum at $0.6 G_0$ to $0.9 G_0$, which is might be caused by a aluminium contact or a disordered gold contact. The second maximum lies at $2 G_0$, which is clear hint for gold. A consecutive histogram, depicted in red,

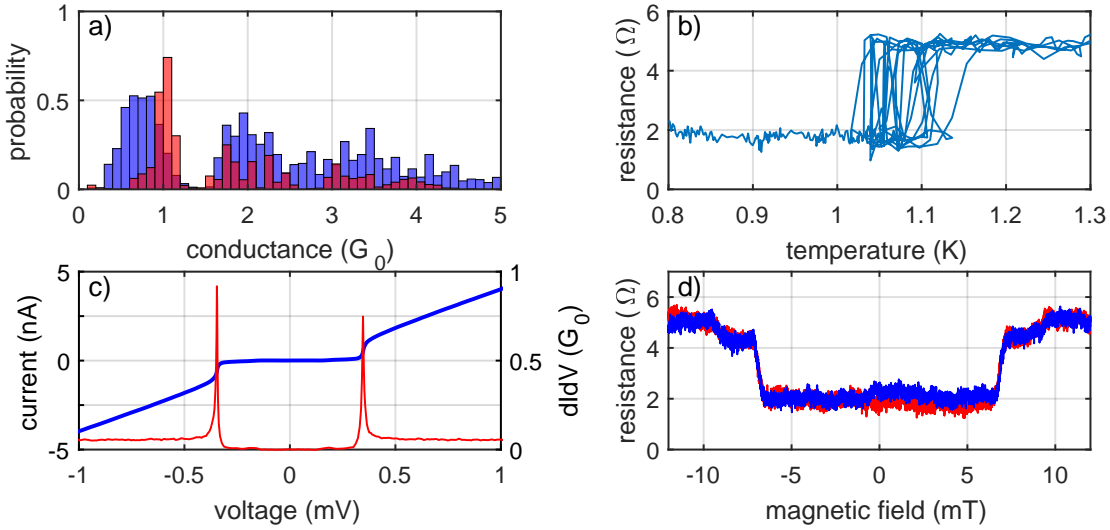


Figure 4.15: Overview over the properties of sample AlAu_29-I-14: In a) two histograms with a first peak at $0.6 G_0$ to $0.9 G_0$ (blue) or $1 G_0$ (red) and a second peak around $2 G_0$ are shown. The blue histogram was recorded first, the red one after several opening traces. A tunnel contact revealing $\Delta = 172.5 \mu\text{eV}$ is shown in c). The critical temperature and the critical field were measured on the unbroken sample and show a residual resistance of 2Ω . T_c was gathered while condensing b). Due to the pulsed gas input, the temperature went across T_c multiple times. The measurement of B_c is shown in d) and includes two transitions.

shows peaks at $1 G_0$ and $2 G_0$, which are clear indications for the atomic contact forming inside the gold. The value for the superconducting gap $\Delta = 172.5 \mu\text{eV}$, which is only slightly below the value of break junction made of aluminium (see section 4.4.1).

All four pre-characterizations point to gold atomic contacts, which are well coupled to the aluminium and, therefore, show good proximity superconductivity.

About 70 contacts of this sample have been measured and analyzed. An overview of four contacts is shown in figure 4.16 including the best fits. For most of the contacts, the best fits show at least two contributing channels. One channel has a high transmission, the second one has lower transmission, mostly a factor of three to four lower. If the conductance of a contact exceeds about $1.3 G_0$ to $1.4 G_0$, one needs at least three contributing channels. One of these channels has a high transmission above 0.95, corresponding to one nearly perfect transmission. The second and the third channel have a lower transmission, but are still separated by a factor of two or more from each other. This justifies the assumption of one main contributing channel with a second minor channel. Additionally, one finds one nearly perfect transmitting channel for contacts above $1 G_0$.

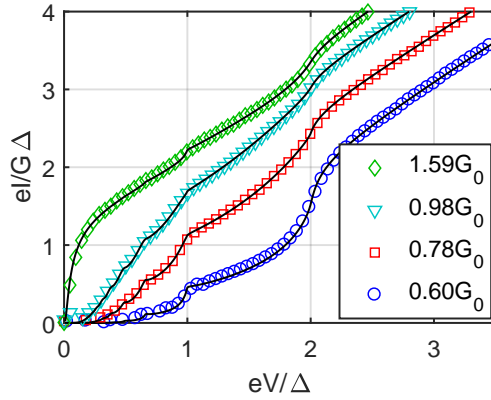


Figure 4.16: Four contacts of sample AlAu_29-I-14: The symbols are the experimental data and the black lines are the corresponding fits. The transmissions are: \circ : 0.39, 0.22, 0, \square : 0.64, 0.14, 0, \triangledown : 0.79, 0.19, 0 and \diamond : 0.99, 0.38, 0.18, 0.05.

Comparison with Theory

Both samples show similar results, which differ remarkably from the reported proximity MAR in gold [Sch+01]. For both samples, one finds at least two channels, which contrasts the perfect transmission expected for the monovalent metal gold. Theoretical calculations predicted mainly one channel [BSJ97], which was also reported by Scheer *et al.* But they also reported the possibility of two or more channels for atomic contacts with $G < G_0$. They assume an imperfection in the contact geometry, which only arises for non-trained samples. A training of the atomic contact was not possible for them. Also in this work, it is hard to perform many opening cycles. Sabater *et al.* reported a high probability to obtain same opening curves, if the contact gets only closed to $5 G_0$ [Sab+12]. To avoid this behavior, the break junction was closed far beyond $5 G_0$, which might have introduced disorder, which lead to gold contacts below $1 G_0$.

A second difference to the results of Scheer *et al.* is, that both samples in this work show BCS like structures and do not have the peaks in the spectra, which Scheer *et al.* saw and assigned to the proximity effect [Sch+01]. One possible explanation for the absence of this peak might be a smaller length between the superconducting leads. The values for this work are in the range of 20 nm to 30 nm (cf. section 4.2.1 and figure 4.17) and the separation in the samples of Scheer *et al.* is up to 60 nm [Sch+01; Sch+02]. A second explanation might be related to the position of the first peak in the histograms, which is lower than expected for well trained gold and more in the range of aluminium. This can be a hint, that the constriction is frequently at the interface between aluminium and gold. This would lead to an asymmetric S-c-N-S contact rather than a S-N-c-N-S contact²⁰.

²⁰S: superconductor, N: normal conductor, c: constriction

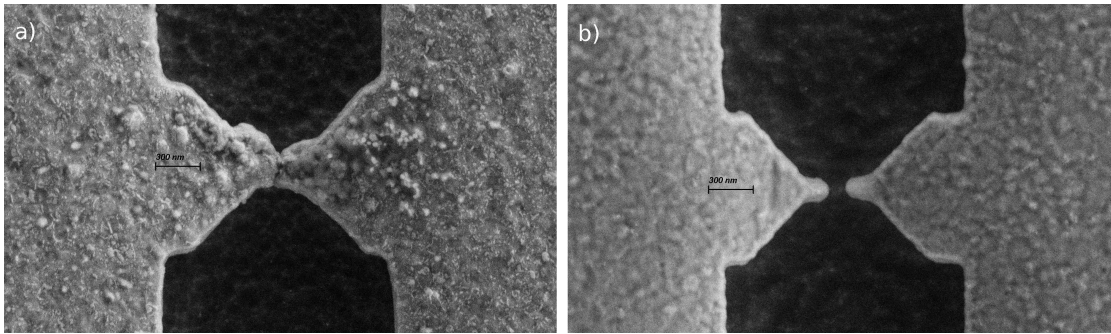


Figure 4.17: SEM micrographs of the two measured proximity samples with aluminium and gold: In **a)** AlAu_29-I-09 reveals a gap between the aluminium of 35 nm, for sample AlAu_29-I-14 **b)** this length is not measurable, since the sample got destroyed after measurement, leaving two separated tips.

Nonetheless, one also gets sharp spectra in the proximity system, which are clearly explainable with the theory of multiple Andreev reflections. This is a good starting point to search for spin-polarized transport in atomic contacts of palladium and the effect of magnetic moments on multiple Andreev reflections.

4.4.3 Aluminium – Palladium: Shadow Evaporation

Since the measurements of shadow evaporated gold on aluminium were straightforward, the first attempt was to use this method for palladium as well. The difficulties in sample preparation of this system are presented in section 4.2.1. Here, the results of the only working sample PdAl_29-II-10 are presented.

The thicknesses of the films are 150 nm aluminium and two consecutive layers of 30 nm palladium each. Therefore, the overall thickness of the palladium is about 60 nm. After the cooldown to 4 K, the sample was broken and a histogram was recorded to check, if a palladium contact is formed. After confirmation of a good palladium contact, as shown in figure 4.18, the junction is closed again and the cryostat is cooled down to base temperature. While cooling down the critical temperature was recorded. After reaching the base temperature, the critical field and the gap were measured: The critical field in the unbroken state, for the gap first a tunnel contact with $R = 173 \text{ k}\Omega$ was established. All three measurements are shown in figure 4.18.

Both, the critical temperature and the critical field, show two transitions. One continuous from 35Ω to 20Ω and one steep, almost step-like, from 20Ω to 0Ω . This leads to the conclusion that there are two parts of the sample, which differ in geometry. Most likely this is the junction itself and the leads including the triangular shaped parts of the sample. The tunnel contact shows rounded coherence peaks at $2\Delta = 68 \mu\text{eV}$. But the dI/dV does not vanish com-

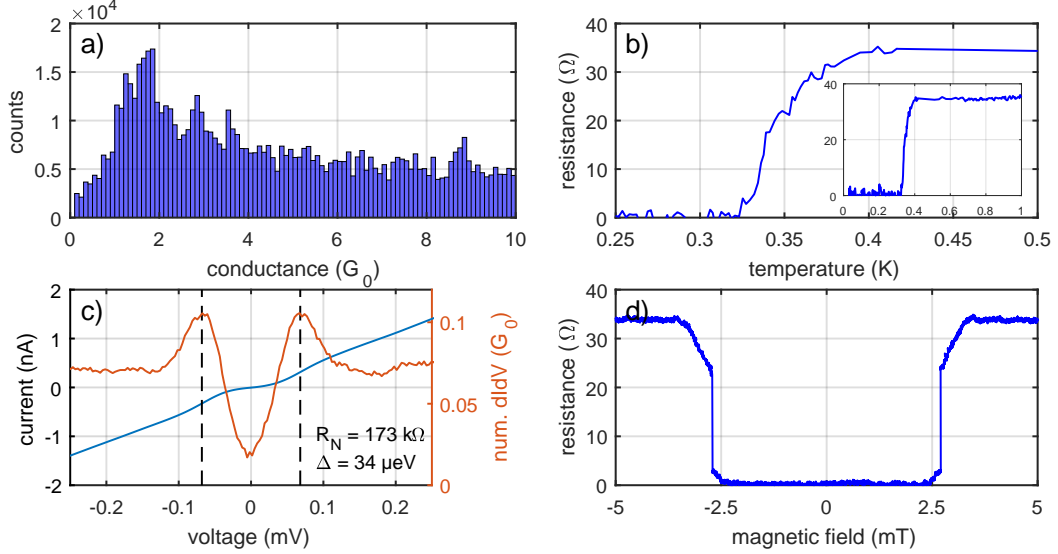


Figure 4.18: For pre-characterizing the aluminium – palladium sample, different measurements were done. The histogram **a)** shows a clear peak for palladium and no signal around $0.8 G_0$, which would be characteristic for aluminium. The measurements for the critical temperature **b)** and field **d)** show values of about 0.34 K and 2.7 mT . The inset in **b)** shows no further step in the resistance at higher temperatures. The gap of $34 \mu\text{eV}$ is measured with an *IV* curve at $173 \text{ k}\Omega$ **c)**.

pletely in the gap. This might be an effect of the strong inverse proximity effect, which also reduces T_c and B_c .

After these pre-characterizations, about 50 contacts with different resistances were measured. For 15 of them, the dependence of the conductance from the magnetic field was investigated to check for similarities with [Str+16]. Also, the behavior of the critical field was analyzed. Typical magnetic field dependencies are shown in figure 4.19 b). These measurements are comparable to the curves found by Strigl *et al.*, but have a smaller effect size. Since the superconducting magnet only allows for a rate of 0.1 T/min , the available field range is at the limit to detect the first finite field extremum around 5 T . Nonetheless, an agreement with the published curves is present.

The critical field B_c might also change with the contact resistance, since the aspect ratio of the smallest part of the sample changes. The results of the measurements are shown in figure 4.19 a). There, the direct resistance $R = U/I$, measured at $U \approx \Delta = 34 \mu\text{eV}$, is depicted. Depending on the resistance of the contact, a reduction or an enhancement of the resistance below B_c is found. This depends on the shape of the *IV* curve of the contact. For a tunnel-like *IV* curve, one expects an increase in resistance, whereas for an *IV* curve with some well transmitting channels, one expects a reduction in resistance. Additionally, the size of the effect also depends on the applied bias, thus, on the voltage drop over the sample. The critical field was measured at 3.3 mT for all contacts. This value corresponds to the field, at which a

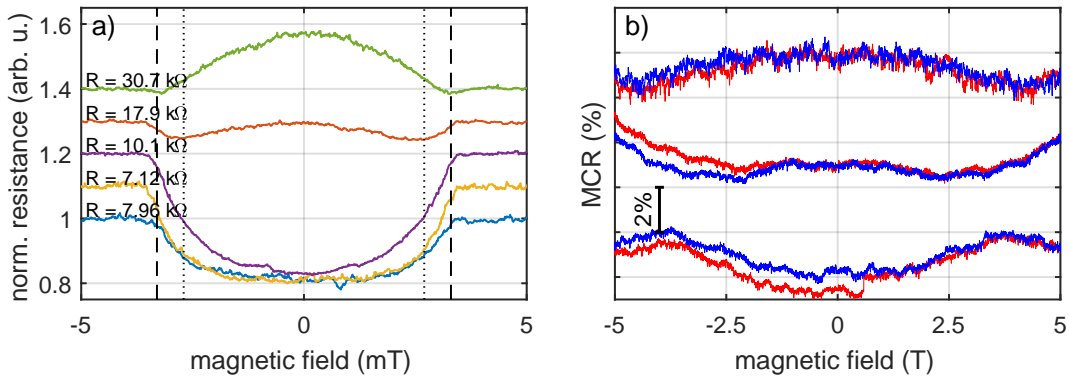


Figure 4.19: The dependence of the resistance on two different field scales. To check the dependence of the critical field B_c from the resistance some contacts are displayed in **a)** up to 5 mT. Depending on the resistance one gets a reduction or an enhancement of the resistance below B_c . The critical field is around 3.3 mT indicated by the black dashed line. The dotted line at 2.7 mT indicates the critical field of the unbroken sample. In **b)** three contacts are shown in the field range to ± 5 T to check the similarity with curves from [Str+16].

first reduction in resistance for the closed sample is present. The different transitions in the T_c and B_c curves might be caused by different demagnetization factors due to the changes in the cross-sections. A second explanation is a change in the strength of the (inverse) proximity effect for different parts of the sample. Therefore, one can conclude, that the leads already transition at 2.7 mT and the constriction may stand a field of 3.3 mT before turning normal conducting.

Most interesting are *IV* curves, since they include information about the exact channel configuration (cf. section 4.1.3) or even about the presence of spin-polarization (cf. section 4.1.4). Normally, the *IV* curves are displayed in reduced units for comparison, here the traces are displayed in non-reduced units, since the superconducting gap Δ is not the same for all contacts. An overview over the different *IV* curves is given in figure 4.20 a). These curves already show the challenge of the measurement principle. The gap measured with the dI/dV of a tunnel contact is $34\mu\text{eV}$. For a contact with a magnetic dot or constriction theory predicts the non-linearities to be shifted to even lower energies (cf. section 4.1.4). Thus one reaches the energy resolution of the setup, which makes it impossible to recognize the shape of the features in the *IV* curves. For an estimation of the energy scale, the numerical dI/dV is calculated and plotted in figure 4.20 b).

For all four presented curves in figure 4.20 one can clearly see, that all the non-linearities in the *IVs* are below 2Δ . Except for the blue curve, they also lie below Δ . All curves show oscillations above $50\mu\text{eV}$ with varying amplitude. The most probable reason for these oscillations is the small signal combined with a numerical dI/dV . Nonetheless, one may observe

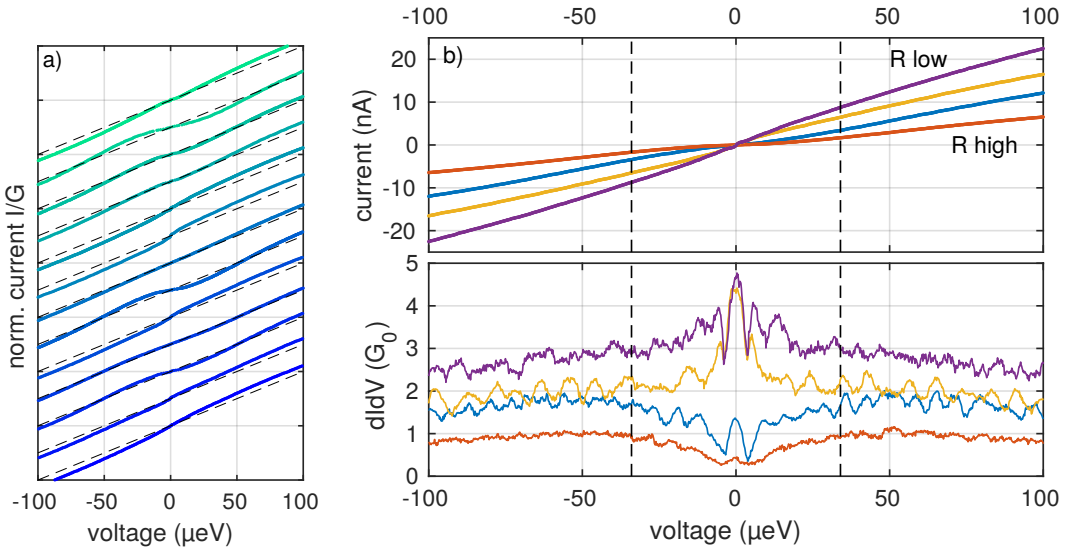


Figure 4.20: **a)** Exemplary IV curves for sample PdAl_29-II-10 are shown. The current is normalized to the conductance. **b)** shows IVs and numerical dI/dV s for selected contacts of sample PdAl_29-II-10. For comparison, the measured gap of $34\text{ }\mu\text{eV}$ is displayed with black dashed line.

non-linearities at energies below Δ . For the two contacts with higher resistance, there is a reduction in the dI/dV , for the other two it is an increase. All four curves show a maximum at $V = 0\text{ V}$, which one might interpret as a signature for a supercurrent. Together with the non-linearities, one can conclude that superconductivity is also present in atomic contacts of this sample. The reduction of the energy of the features in the IV curves, compared to the gap energy measured by a tunnel spectrum, is a hint for magnetic properties of these contacts (cf. section 4.1.4). Unfortunately, the features are extremely shallow, so that it is not possible to draw any further conclusions on the exact size or shape.

However, we do see an effect of the magnetic order, which makes it interesting to analyze that system in more detail. To increase the energy resolution, the sample preparation was modified from shadow evaporation to a multi-step lithography. The outcome of the samples from that fabrication process are discussed in the next section.

4.4.4 Aluminium – Palladium: Multi-Step Lithography

As already stated in section 4.2.2, the sample preparation using multi-step lithography was not successful, since all samples show an indication of aluminium in the histogram. Nonetheless, the sample PdAl_30-II-18 was measured, since the histogram shows a peak around 0.8 G_0 , as it is characteristic for aluminium, but there is no pronounced minimum around 1.2 G_0 (cf. figure 4.21 a)). Since this could be an indication for a contact including palladium, the sam-

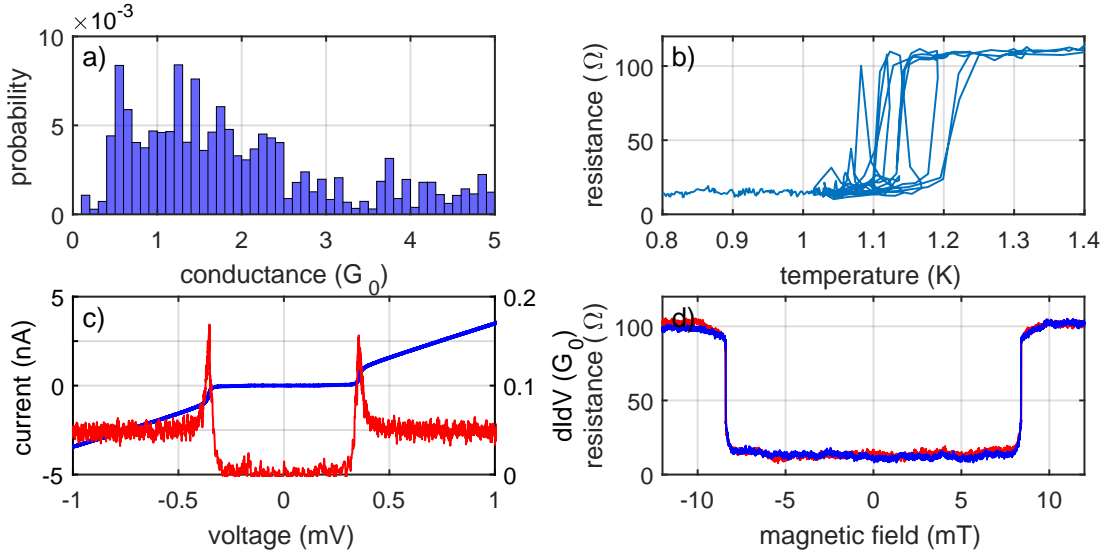


Figure 4.21: Overview over the pre-measurements of sample PdAl_30-II-18: **a)** The histogram of 50 opening traces shows a broad plateau at $0.8 G_0$ to $2.5 G_0$. This plateau is not common for aluminium or palladium. **b)** The temperature dependence of the resistance while condensing shows multiple curves due to the fast cycles. The most probable transition temperature is around 1.14 K. **c)** The tunnel curve of a contact with $269 \text{ k}\Omega$ reveals a gap of $176 \mu\text{eV}$. **d)** Measurement of the critical field: The transition takes place at 8.39 mT .

ple was measured in more detail. Before investigating atomic contacts, the superconducting properties were measured. The corresponding plots are shown in figure 4.21. The key features are $T_c = 1.14 \text{ K}$, $B_c = 8.39 \text{ mT}$ and $\Delta = 176 \mu\text{eV}$. Both, T_c and B_c , are reduced compared to the properties of bulk aluminium. Also the gap Δ is slightly reduced. All three properties might be hints for proximity superconductivity or at least a reduction of the superconductivity due to the inverse proximity effect.

To judge the zone of contact in more detail, one also can have a look at the SEM pictures taken before and after measurement. Both are shown in figure 4.22. The picture taken before cooldown (and before underetching) shows a tiny separation between the two aluminium leads. The broad first peak in the histogram and the only slightly reduced superconducting parameters, together with the SEM picture, lead to the conclusion, that most probably the atomic contacts formed between aluminium and palladium. Taking the picture after measurement into account as well, the conclusion is not so clear anymore. Here, it is hard to distinguish if there is still a separation between the aluminium leads or not.

Even though it was not clear, if the sample breaks in aluminium or in palladium, atomic contacts have been measured. For the 200 measured contacts no significant changes compared to pure aluminium in the non-linearities in the IV curves have been recorded (cf. figure 4.23), but the number of participating channels differs from the findings in pure aluminium. For

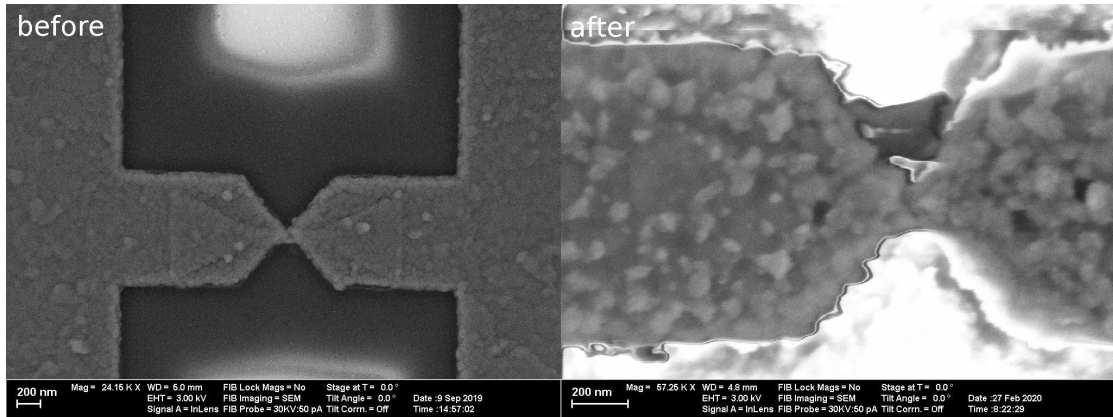


Figure 4.22: SEM pictures of the sample PdAl_30-II-18 before (left) and after (right) measurement: The picture before the measurement shows a tiny gap in the aluminium. This gap is not visible anymore after the measurement, caused by contamination or local modification of the constriction, due to energy deposition during measurement or inspection in the SEM.

contacts with a conductance of about $< 0.85 G_0$, one gets three contributing channels, with one dominating the conductance and two additional minor ones (see [figure 4.23 a\)](#)). In the regime of $0.85 G_0$ to $1.0 G_0$, the number of contributing channels reduces to only two. Mostly one dominating channel with $\tau > 0.9$ and one minor channel (see [figure 4.23 b\)](#)). Above $1.1 G_0$, the three-channel behavior appears again. With increasing conductance also the number of channels increases with at least four channels for contacts with $1.6 G_0$ and for contacts with a conductance above $2 G_0$, one needs at least five channels to describe the *IV* curves. But the fitting procedure is not reliable for such high conductance (cf. [section 4.4.1](#)). Often only the minimal number of channels can be determined by fitting with an increasing number of channels, and resolving the number at which the fit converges first. Contacts having a conductance of more than $1.6 G_0$ and needing at least five channels to be described are depicted in [figure 4.23 c\)](#).

The behavior for contacts around $1 G_0$ and the need of four channels for contacts with $1.6 G_0$ to $2.0 G_0$ indicate a difference in the contact in comparison with pure aluminium samples, but none of the contacts showed a reduction of the energy for the non-linearities as it was measured in the shadow evaporated sample (cf. [section 4.4.3](#)). This leaves the discussion open for the exact configuration of the constriction. Most probable contact formation is at the interface between aluminium and palladium.

The development of the *IV* curves in magnetic fields, can reveal more information about the exact configuration of the constriction [[Sch+02](#)]. The measurements of two contacts are depicted in [figure 4.24](#). For zero applied field, the quasiparticle onset is at the measured gap of $2\Delta = 325 \mu\text{eV}$ and the multiple Andreev reflections are clearly distinguishable, but the quasi-particle onsets start to round quickly with increasing field (green curves). Also the position

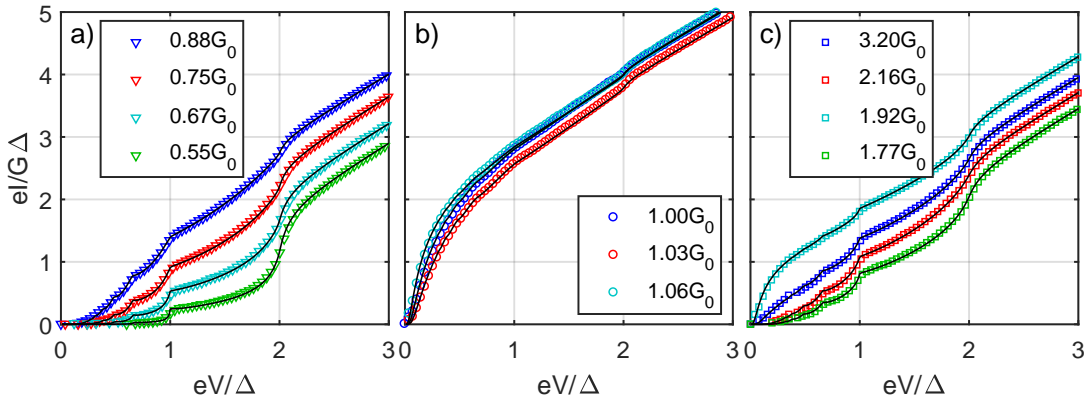


Figure 4.23: Three groups of contacts with different conductance:

- a) Contacts with $G < 0.9G_0$ show three channels as known from aluminium. The transmissions are ∇ : 0.73, 0.14, 0.02; ∇ : 0.59, 0.10, 0.08; ∇ : 0.44, 0.14, 0.08 and ∇ : 0.23, 0.20, 0.11.
- b) Three contacts around $1G_0$ show only two contributing channels: \circ : 0.95 and 0.06; \circ : 0.93 and 0.10 and \circ : 0.96 and 0.10.
- c) Four contacts above $1.6G_0$ show at least four contributing channels: \square : 0.93, 0.62, 0.56, 0.31, 0.30, 0.29, 0.10, 0.08; \square : 0.78, 0.46, 0.46, 0.25, 0.20; \square : 0.97, 0.47, 0.28, 0.15, 0.04 and \square : 0.67, 0.32, 0.30, 0.24, 0.21.

of the current onsets decreases with increasing field. If one concentrates on the quasiparticle onset, one finds a sudden decrease of the voltage to roughly $125\mu\text{eV}$ at a field of about 8 mT . Finally, the IV curve gets linear for $B > 9.6\text{ mT}$. When decreasing the magnetic field again, the field and the voltage, where the first non-linearities occur, are not always the same as with increasing field. A similar, but somehow more reproducible behavior, has been reported by Scheer *et al.* in the system aluminium-gold-aluminium [Sch+02]. Their findings and explanation are discussed in the next paragraph, followed by a detailed description of the measurements of this sample.

Scheer *et al.* investigated the proximity system aluminium-gold-aluminium with the constriction located inside the gold. They also examined the evolution of the IV curves with magnetic fields and found similar behavior of the quasiparticle onset as reported here. First, I will briefly introduce their model and then summarize their findings. They assume a proximity system with the constriction asymmetric with respect to the superconducting aluminium. A sketch of their model is depicted in figure 4.25 a). In proximity superconductivity, the response to an external field is not like in standard superconductors, but they feature a so-called breakdown field. For low temperatures, the transition becomes first order, like for Type 1 superconductors. So one can have the effects of supercooling and superheating, with the corresponding field scales $B_{sc} \approx \Phi_0/\lambda_N^2$ and $B_{sh} \approx \Phi_0/\xi(L_N)^2$. With the London penetration depth λ_N and $\xi(L_N)$ the effective coherence length for a proximitized normal conductor with length L_N . Since one has two different sized normal conductors, one can expect to have

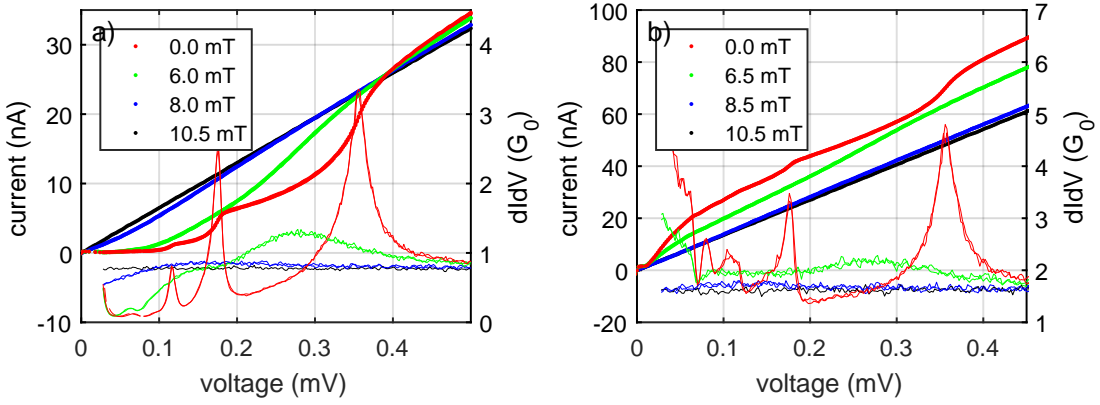


Figure 4.24: The evolution of the IV curves with in-/decreasing magnetic field is shown for two contacts with $G = 0.85 G_0$ **a)** and $G = 1.75 G_0$ **b)**. Only selected curves are depicted. Additionally, the corresponding dI/dV traces are shown. For clarity the dI/dVs are only shown for $V > 25 \mu V$. The blue curves show a shallow peak around $125 \mu V$ corresponding roughly to the minigap E_g .

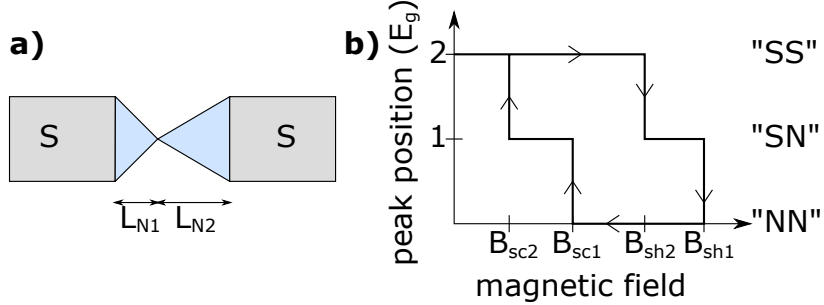


Figure 4.25: **a)** Model of an asymmetric proximity constriction, with different proximity length L_{N1}/L_{N2} is depicted. **b)** One possible evolution of the quasiparticle onset with in-/decreasing field: The possible states of each side of the constriction are indicated in the picture. Reproduced from [Sch+02].

also two fields for supercooling and superheating. One possible measure of the state of the sides of the constriction is the position or better voltage of the quasiparticle onset. For a contact between two superconductors (“SS”) one expects the quasiparticle onset at an energy of $2E_g$ ²¹, for an “SN” contact, between on superconducting and a normal conducting side, one expects it to be at E_g , for two normal conductors (“NN”) there are no quasiparticle onsets. One possible scheme of the progress of the quasiparticle onset is depicted in figure 4.25 b). In their experiment Scheer *et al.* were able to localize all four fields ($B_{sh1}, B_{sh2}, B_{sc1}, B_{sc2}$). In their sample the two superheating fields are close together, but there is a distinct difference of about 0.5 mT between the two supercooling fields. So they measure an open loop in the E_g

²¹To distinguish between pure and proximity superconductivity, literature talks about the gap Δ for pure superconducting systems and the minigap E_g for proximity superconductivity.

over B diagram for contacts from the tunneling up to $1.7 G_0$. Their second finding concerns the subgap structure, which vanishes at moderate fields.

For the sample PdAl_30-II-18, which is discussed here, one does not find one clear master curve in the E_g vs. B diagram. Instead, there are about five to six different shapes. These shapes are discussed now and are depicted in [figure 4.26](#).

1. No difference between superheating and supercooling, leading to $B_{sh1} = B_{sc1} \approx 9.6 \text{ mT}$ and $B_{sh2} = B_{sc2} \approx 7.4 \text{ mT}$ (cf. [figure 4.26 a](#)), 5 contacts)
2. Loop in the upper field, $B_{sh2} = B_{sc2} = 7.4 \text{ mT}$ but $B_{sh1} = 9.6 \text{ mT} > B_{sc1} = 9.0 \text{ mT}$ (cf. [figure 4.26 b](#)), 3 contacts)
3. The fields for superheating and cooling are the same and comparable to item 1, but the voltages for the “SN” case are not the same for increasing and decreasing field: $E_g^{\text{inc}} > E_g^{\text{dec}}$ (cf. [figure 4.26 c](#)), 2 contacts)
4. Same as item 3, but with $E_g^{\text{inc}} < E_g^{\text{dec}}$ (cf. [figure 4.26 d](#)), 2 contacts)
5. These two curves reveal small differences for both field pairs: $B_{sh1} > B_{sc1}$ and $B_{sh2} < B_{sc1}$ (cf. [figure 4.26 e](#)), 2 contacts)

The effects of item 3 to 5 are not very pronounced and hard to distinguish from case 1. Nonetheless, one finds a clear intermediate state in all contacts, which probably corresponds to the “SN” state Scheer *et al.* introduced. This “SN” state is mostly located at a field between 7.4 mT and 9.6 mT . Slight deviations might be interpreted as an effect of different degrees of disorder, since disorder has an effect on both, the penetration depth λ_N and the effective coherence length $\xi(L_N)$ [[Sch+02](#)]. This changed disorder might arise from opening curves performed in between the measurements to establish a fresh contact. No correlation between the shape and the conductance of the contacts is present.

4.5 Discussion

As already discussed throughout this chapter, the measurement of superconducting atomic contacts made of palladium is not easy. Here two different approaches have been introduced. The samples made with shadow evaporation showed a strong reduction of the superconductivity due to the inverse proximity effect. Even though one is able to recognize a further reduction of the voltages of the non-linearities, an exact study of the reduction and the resulting *IV* curves is not possible. The main reason is the limited resolution in energy. A better energy resolution is either possible with an advanced amplifier chain, as used by Lorenz and Sprenger [[Lor18](#); [LSS18](#); [Spr20](#)], or one uses so called cryogenic amplifiers. These amplifiers

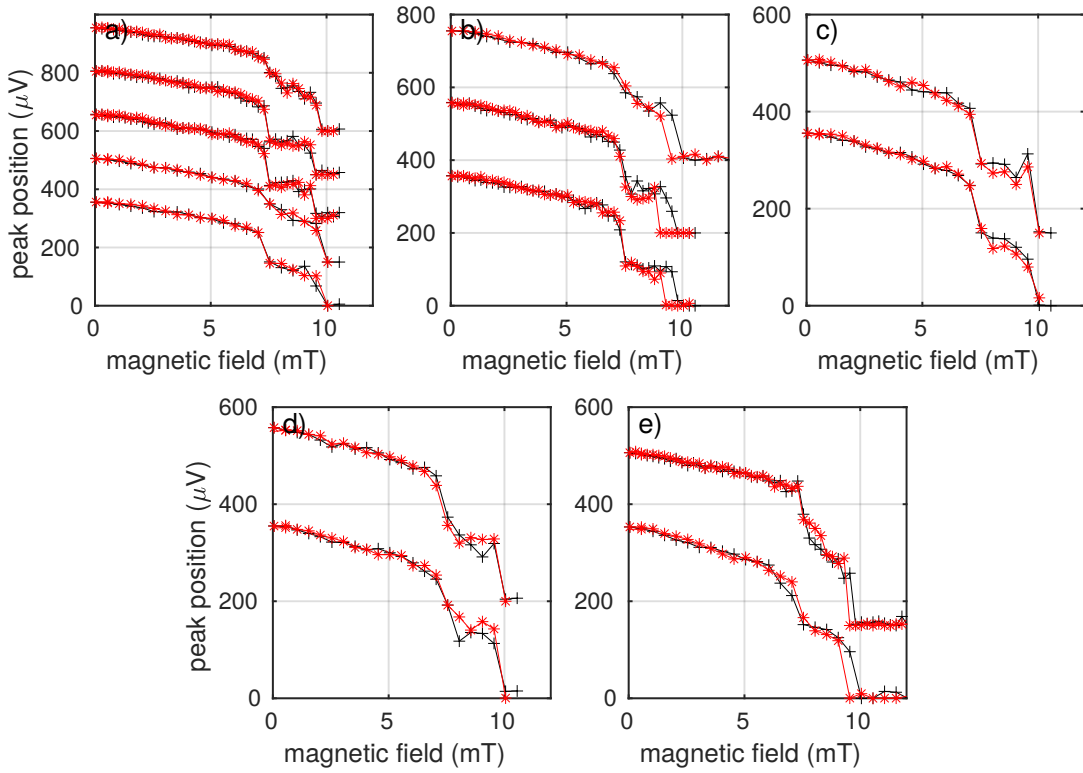


Figure 4.26: Different measurements of the position of the quasiparticle onset: The panels correspond to the different cases discussed in the text. The curves are shifted for clarity. The black data points were recorded with increasing magnetic fields and red data points with decreasing magnetic field. The loops in panels c)-e) are small and, therefore, hard to detect. It is not possible to correlate the cases with the conductance of the contacts. The difference between the contacts are only a fresh established contacts.

have two advantages: First, they are closer to the sample and so the pick-up of noise is reduced, second the electronics themselves is at low-temperature, e.g. 60 K, and, therefore, the noise contribution of the amplifier is reduced.

A second approach to increase the visibility of the features is to try to enhance the signal itself. This was tried using multi-step lithography to reduce the amount of palladium and, therefore, the expected inverse proximity effect. The sample preparation of these samples is quite challenging (cf. section 4.2), hence it was not possible to create a sample showing only palladium in the histogram, e.g. having only a peak at $1.6 G_0$ and no peak at $0.8 G_0$. But one sample revealed a broad plateau between $0.8 G_0$ and $2.2 G_0$. Further investigation revealed an unexpected behavior at $1 G_0$ with only two contributing channels. Also the dependence of the IVs in magnetic fields indicates an atomic contact forming at the interface between alu-

minium and palladium. Thus, one would expect the formation of a magnetic moment. But no evidence was found for the presence of a magnetic moment. Therefore, also the question for the presence of any spin-polarization in atomic contacts of strong paramagnets remains unanswered.

There are additional steps, one can think about to improve the sample preparation for both presented ways. The shadow evaporation suffers from the need to evaporate the palladium last, since the tensions during the evaporation rips off the tiny resist bridge, which forms the separation in the aluminium. To overcome this problem, one might use a metal mask during evaporation, which should withstand the tension. This would offer the possibility of shadow evaporation with palladium as a first metal, which would allow to use a thinner layer of palladium and, hence, reduce the influence of the inverse proximity effect.

But also the two-step lithography might benefit from two modifications: In the last version of the sample preparation, most of the samples died from a local discharge over the small separation between the aluminium leads. One might try to protect the aluminium leads by designing a metal shortcut between the two leads. After finishing the sample preparation one can break the shortcut by FIB or simple scratching, depending on the size of the shortcut. Another possibility is the use of a conductive resist, like Electra 92 [All16], instead or additional to the PMMA. Such a layer should prevent the sample from local accumulation of charge on one side of the separation in the aluminium.

Chapter 5

Conclusion

In this thesis, the properties of atomic contacts of strong paramagnets have been investigated. Strong paramagnets are metals which feature a high Stoner enhancement. Thus, a change in the density of states leads to an emergence of a magnetic order. This local magnetic order is a good testbed to investigate the effects of magnetism on the atomic scale. There are different approaches to examine this magnetic order: Transport measurement with and without magnetic fields, shot noise measurements, and measurements with superconducting leads. All three approaches have been used in this thesis.

The magneto-transport measurements have been performed on iridium. The magneto-conductance (MC) and anisotropic magneto-conductance (AMC) measurements showed similar results as the already published metals palladium and platinum. The key features are a big, non-monotonous magneto-conductance in magnetic fields perpendicular to the contact direction. Additionally, these curves feature a hysteresis around zero field. Both, the MC and the AMC curves, show a rich variety of shapes, which depends on the exact configuration of the atomic contact. For the two most frequent shapes of the MC a model could be applied and proven during the elongation of an atomic contact. Such elongation leads to a transition from collinear to non-collinear alignment of the magnetic moments in the contact, as proposed by theory.

The dI/dV curves show two kinds of zero-bias anomalies (ZBA). A Kondo-resonance-like behavior and an oscillatory behavior known from conductance fluctuations. The continuous transition between these two results in two possible Kondo temperatures: 26 K and 125 K. For palladium, similar values have been published. The lower value was proposed to arise from two-level fluctuations due to fast openings of the contact. Control measurement for iridium with low opening speed show indeed only resonances with the higher Kondo temperature of 125 K.

For the two other approaches, the corresponding setups have been equipped and characterized. The characterization measurement of the shot noise setup showed single channel, spin-

degenerate transport for gold and spin-polarized transport for the bulk ferromagnet cobalt. Measurements on the strong paramagnets platinum, palladium, and iridium do not show clear signs of spin-polarization. But all three metals show an accumulation of data points at the border to the spin-polarized regime. These findings are in contrast to simulations, but in line with older measurements on platinum. One possible explanation is the separation of the transport and the magnetic order in different orbitals. Thus, the conduction electrons interact only little with the electrons forming the magnetic moments and no or only little spin-polarization is detectable in direct transport measurements.

The sample preparation for measurements with superconducting leads was challenging. Two different techniques were used: Shadow evaporation and multi-step lithography. Both had their own drawbacks. Nonetheless, two samples made of palladium and aluminium were measured. One of them showed a strong reduction of the expected non-linearities in the *IV* curves. This reduction is a clear hint for the presence of a magnetic moment inside the atomic contact of palladium.

For the second sample, it remains unclear if the atomic contact was formed inside the palladium or the aluminium. A third option is the interface between the two metals, which is the most probable position. This sample did not show clear signature of magnetic moments. Therefore, further measurements have to be carried out to reveal the origin of the reduction seen in the first sample.

Concluding, one can say that in atomic contacts of strong paramagnets a local magnetic order emerges. But the shot noise measurements point to a separation of magnetism and transport. Therefore, no spin-polarization could be measured in atomic contacts of strong paramagnets. The measurements with superconducting leads did not give conclusive results, but show signs of magnetic order.

Bibliography

- [AB95] D. Averin and A. Bardas: “ac Josephson Effect in a Single Quantum Channel”, *Phys. Rev. Lett.* **75**, 1831 (1995) DOI: [10.1103/PhysRevLett.75.1831](https://doi.org/10.1103/PhysRevLett.75.1831).
- [ACF02] M. Andersson, J. C. Cuevas and M. Fogelström: “Transport through superconductor/magnetic dot/superconductor structures”, *Physica C* **367**, 117 (2002) DOI: [10.1016/S0921-4534\(01\)00977-7](https://doi.org/10.1016/S0921-4534(01)00977-7).
- [Agr+02] N. Agrait, C. Untiedt, G. Rubio-Bollinger and S. Vieira: “Onset of Energy Dissipation in Ballistic Atomic Wires”, *Phys. Rev. Lett.* **88**, 216803 (2002) DOI: [10.1103/PhysRevLett.88.216803](https://doi.org/10.1103/PhysRevLett.88.216803).
- [Agu+07] F. Aguilera-Granja, A. Vega, J. Rogan, W. Orellana and G. García: “Magnetic properties of Pd atomic clusters from different theoretical approaches”, *Eur. Phys. J. D* **44**, 125 (2007) DOI: [10.1140/epjd/e2007-00174-9](https://doi.org/10.1140/epjd/e2007-00174-9).
- [All16] Allresist GmbH: *Protective Coating PMMA Electra 92 (AR-PC 5090)* (2016).
- [And+77] O. K. Andersen, J. Madsen, U. K. Poulsen, O. Jepsen and J. Kollár: “Magnetic ground state properties of transition metals”, *Physica B+C* **86**, 249 (1977) DOI: [10.1016/0378-4363\(77\)90303-5](https://doi.org/10.1016/0378-4363(77)90303-5).
- [And61] P. W. Anderson: “Localized Magnetic States in Metals”, *Phys. Rev.* **124**, 41 (1961) DOI: [10.1103/PhysRev.124.41](https://doi.org/10.1103/PhysRev.124.41).
- [And64] A. F. Andreev: “The Thermal Conductivity of the Intermediate State in Superconductors”, *Sov. Phys. JETP* **19**, 1823 (1964).
- [And70] O. K. Andersen: “Electronic Structure of the fcc Transition Metals Ir, Rh, Pt, and Pd”, *Phys. Rev. B* **2**, 883 (1970) DOI: [10.1103/PhysRevB.2.883](https://doi.org/10.1103/PhysRevB.2.883).
- [And80] N. Andrei: “Diagonalization of the Kondo Hamiltonian”, *Phys. Rev. Lett.* **45**, 379 (1980) DOI: [10.1103/PhysRevLett.45.379](https://doi.org/10.1103/PhysRevLett.45.379).
- [ARV93] N. Agrait, J. G. Rodrigo and S. Vieira: “Conductance steps and quantization in atomic-size contacts”, *Phys. Rev. B* **47**, 12345 (1993) DOI: [10.1103/PhysRevB.47.12345](https://doi.org/10.1103/PhysRevB.47.12345).
- [Aut+08] G. Autès, C. Barreteau, M. C. Desjonquères, D. Spanjaard and M. Viret: “Giant orbital moments are responsible for the anisotropic magnetoresistance of atomic contacts”, *EPL* **83**, 17010 (2008) DOI: [10.1209/0295-5075/83/17010](https://doi.org/10.1209/0295-5075/83/17010).

- [AYR03] N. Agrait, A. L. Yeyati and J. M. van Ruitenbeek: “Quantum Properties of Atomic-Sized Conductors”, *Phys. Rep.* **377**, 81 (2003) DOI: [10.1016/S0370-1573\(02\)00633-6](https://doi.org/10.1016/S0370-1573(02)00633-6).
- [Bah+19] S. G. Bahoosh, M. A. Karimi, W. Belzig, E. Scheer and F. Pauly: “Influence of electron-vibration interactions on electronic current noise of atomic and molecular junctions”, *arXiv*, 1912.13496 (2019).
- [BB00] Y. M. Blanter and M. Büttiker: “Shot noise in mesoscopic conductors”, *Phys. Rep.* **336**, 1 (2000) DOI: [10.1016/S0370-1573\(99\)00123-4](https://doi.org/10.1016/S0370-1573(99)00123-4).
- [BB07] I. M. Bobkova and A. M. Bobkov: “Influence of spin filtering and spin mixing on the subgap structure of $I-V$ characteristics in a superconducting quantum point contact”, *Phys. Rev. B* **76**, 094517 (2007) DOI: [10.1103/PhysRevB.76.094517](https://doi.org/10.1103/PhysRevB.76.094517).
- [BCS57] J. Bardeen, J. N. Cooper and J. R. Schrieffer: “Theory of Superconductivity”, *Phys. Rev.* **108**, 1175 (1957) DOI: [10.1103/PhysRev.108.1175](https://doi.org/10.1103/PhysRev.108.1175).
- [BF13] BlueFors Cryogenics: *BF-LD400 - Cryogen-Free Dilution Refrigerator System* (2013).
- [BJ01] S. R. Bahn and K. W. Jacobsen: “Chain Formation of Metal Atoms”, *Phys. Rev. Lett.* **87**, 266101 (2001) DOI: [10.1103/PhysRevLett.87.266101](https://doi.org/10.1103/PhysRevLett.87.266101).
- [BK13] W. Buckel and R. Kleiner: *Supraleitung: Grundlagen und Anwendungen*, John Wiley & Sons (2013).
- [BKR06] K. I. Bolotin, F. Kuemmeth and D. C. Ralph: “Anisotropic Magnetoresistance and Anisotropic Tunneling Magnetoresistance due to Quantum Interference in Ferromagnetic Metal Break Junctions”, *Phys. Rev. Lett.* **97**, 127202 (2006) DOI: [10.1103/PhysRevLett.97.127202](https://doi.org/10.1103/PhysRevLett.97.127202).
- [Blu01] S. Blundell: *Magnetism in Condensed Matter*, Oxford University Press (2001).
- [Bob06] I. M. Bobkova: “Subharmonic gap structure in superconductor/ferromagnet/superconductor junctions”, *Phys. Rev. B* **73**, 012506 (2006) DOI: [10.1103/PhysRevB.73.012506](https://doi.org/10.1103/PhysRevB.73.012506).
- [BR04] C. Buzea and K. Robbie: “Assembling the puzzle of superconducting elements: a review”, *Supercond. Sci. Technol.* **18**, R1 (2004) DOI: [10.1088/0953-2048/18/1/R01](https://doi.org/10.1088/0953-2048/18/1/R01).
- [BR99] H. E. van den Brom and J. M. van Ruitenbeek: “Quantum Suppression of Shot Noise in Atom-Size Metallic Contacts”, *Phys. Rev. Lett.* **82**, 1526 (1999) DOI: [10.1103/PhysRevLett.82.1526](https://doi.org/10.1103/PhysRevLett.82.1526).
- [BRK05] T. Bechtold, E. V. Rudnyi and J. G. Korvink: “Dynamic electro-thermal simulation of microsystems—a review”, *J. Micromech. Microeng.* **15**, R17 (2005) DOI: [10.1088/0960-1317/15/11/R01](https://doi.org/10.1088/0960-1317/15/11/R01).

- [BS71] H. Bittel and L. Strom: *Rauschen. Eine Einführung zum Verständnis elektrischer Schwankungserscheinungen*, Springer-Verlag (1971).
- [BSJ97] M. Brandbyge, M. R. Sørensen and K. W. Jacobsen: “Conductance eigenchannels in nanocontacts”, *Phys. Rev. B* **56**, 14956 (1997) DOI: [10.1103/PhysRevB.56.14956](https://doi.org/10.1103/PhysRevB.56.14956).
- [BSW95] E. N. Bratus’, V. S. Shumeiko and G. Wendin: “Theory of Subharmonic Gap Structure in Superconducting Mesoscopic Tunnel Contacts”, *Phys. Rev. Lett.* **74**, 2110 (1995) DOI: [10.1103/PhysRevLett.74.2110](https://doi.org/10.1103/PhysRevLett.74.2110).
- [BTK82] G. E. Blonder, M. Tinkham and T. M. Klapwijk: “Transition from metallic to tunneling regimes in superconducting microconstrictions: Excess current, charge imbalance, and supercurrent conversion”, *Phys. Rev. B* **25**, 4515 (1982) DOI: [10.1103/PhysRevB.25.4515](https://doi.org/10.1103/PhysRevB.25.4515).
- [Bur+15] A. Burtzlaff, A. Weismann, M. Brandbyge and R. Berndt: “Shot Noise as a Probe of Spin-Polarized Transport through Single Atoms”, *Phys. Rev. Lett.* **114**, 016602 (2015) DOI: [10.1103/PhysRevLett.114.016602](https://doi.org/10.1103/PhysRevLett.114.016602).
- [Bur+16] A. Burtzlaff, N. L. Schneider, A. Weismann and R. Berndt: “Shot noise from single atom contacts in a scanning tunneling microscope”, *Surface Science* **643**, 10 (2016) DOI: [10.1016/j.susc.2015.07.006](https://doi.org/10.1016/j.susc.2015.07.006).
- [Bur17] A. Burtzlaff: “Shot noise measurements at single atom contacts in a low-temperature Scanning Tunneling Microscope”, Christian-Albrechts-Universität zu Kiel (2017).
- [Cal+09] M. R. Calvo, J. Fernández-Rossier, J. J. Palacios, D. Jacob, D. Natelson and C. Untiedt: “The Kondo effect in ferromagnetic atomic contacts”, *Nature* **458**, 1150 (2009) DOI: [10.1038/nature07878](https://doi.org/10.1038/nature07878).
- [CH15] H. D. Chopra and S. Z. Hua: “Ballistic magnetoresistance over 3000% in Ni nanocontacts at room temperature”, *Phys. Rev. B* **66**, 020403 (2015) DOI: [10.1103/PhysRevB.66.020403](https://doi.org/10.1103/PhysRevB.66.020403).
- [Che+15] R. Chen, P. J. Wheeler, M. Di Ventra and D. Natelson: “Enhanced noise at high bias in atomic-scale Au break junctions”, *Sci. Rep.* **4**, 4221 (2015) DOI: [10.1038/srep04221](https://doi.org/10.1038/srep04221).
- [Chu+02] S. H. Chung, M. Muñoz, N. García, W. F. Egelhoff and R. D. Gomez: “Universal Scaling of Ballistic Magnetoresistance in Magnetic Nanocontacts”, *Phys. Rev. Lett.* **89**, 287203 (2002) DOI: [10.1103/PhysRevLett.89.287203](https://doi.org/10.1103/PhysRevLett.89.287203).
- [CJU12] M. R. Calvo, D. Jacob and C. Untiedt: “Analysis of Kondo effect in ferromagnetic atomic-sized contacts”, *Phys. Rev. B* **86**, 075447 (2012) DOI: [10.1103/PhysRevB.86.075447](https://doi.org/10.1103/PhysRevB.86.075447).

- [CM19] S. Cocklin and D. K. Morr: “Scanning tunneling shot-noise spectroscopy in Kondo systems”, *Phys. Rev. B* **100**, 125146 (2019) DOI: [10.1103/PhysRevB.100.125146](https://doi.org/10.1103/PhysRevB.100.125146).
- [CMY96] J. C. Cuevas, A. Martín-Rodero and A. L. Yeyati: “Hamiltonian approach to the transport properties of superconducting quantum point contacts”, *Phys. Rev. B* **54**, 7366 (1996) DOI: [10.1103/PhysRevB.54.7366](https://doi.org/10.1103/PhysRevB.54.7366).
- [COK98] S. M. Cronenwett, T. H. Oosterkamp and L. P. Kouwenhoven: “A Tunable Kondo Effect in Quantum Dots”, *Science* **281**, 540 (1998) DOI: [10.1126/science.281.5376.540](https://doi.org/10.1126/science.281.5376.540).
- [Cox+94] A. J. Cox, J. G. Louderback, S. E. Apsel and L. A. Bloomfield: “Magnetism in 4d-transition metal clusters”, *Phys. Rev. B* **49**, 12295 (1994) DOI: [10.1103/PhysRevB.49.12295](https://doi.org/10.1103/PhysRevB.49.12295).
- [Cro+01] R. Cron, M. F. Goffman, D. Esteve and C. Urbina: “Multiple-Charge-Quanta Shot Noise in Superconducting Atomic Contacts”, *Phys. Rev. Lett.* **86**, 4104 (2001) DOI: [10.1103/PhysRevLett.86.4104](https://doi.org/10.1103/PhysRevLett.86.4104).
- [Cro01] R. Cron: “Atomic Contacts: a Test-Bed for Mesoscopic Physics”, Université Paris 6 (2001).
- [CS10] J. C. Cuevas and E. Scheer: *Molecular Electronics: An Introduction to Theory and Experiment*, World Scientific (2010).
- [Cso+04] S. Csonka, A. Halbritter, G. Mihály, O. I. Shklyarevskii, S. Speller and H. van Kempen: “Conductance of Pd-H Nanojunctions”, *Phys. Rev. Lett.* **93**, 016802 (2004) DOI: [10.1103/PhysRevLett.93.016802](https://doi.org/10.1103/PhysRevLett.93.016802).
- [DSS81] P. H. Dederichs, H. Schober and D. J. Sellmyer: *Landolt-Börnstein - Group III Condensed Matter 13a (Phonon States of Elements. Electron States and Fermi Surfaces of Alloys)*, Springer (1981).
- [DT03] A. Delin and E. Tosatti: “Magnetic Phenomena in 5d Transition Metal Nanowires”, *Phys. Rev. B* **68**, 144434 (2003) DOI: [10.1103/PhysRevB.68.144434](https://doi.org/10.1103/PhysRevB.68.144434).
- [DT04a] A. Delin and E. Tosatti: “Emerging Magnetism in Platinum Nanowires”, *Surface Science* **566**, 262 (2004) DOI: [10.1016/j.susc.2004.05.055](https://doi.org/10.1016/j.susc.2004.05.055).
- [DT04b] A. Delin and E. Tosatti: “The electronic structure of 4d transition-metal monoatomic wires”, *J. Phys.: Condens. Matter* **16**, 8061 (2004) DOI: [10.1088/0953-8984/16/45/028](https://doi.org/10.1088/0953-8984/16/45/028).
- [Egl+10] S. Egle, C. Bacca, H.-F. Pernau, M. Huefner, D. Hinzke, U. Nowak and E. Scheer: “Magnetoresistance of atomic-size contacts realized with mechanically controllable break junctions”, *Phys. Rev. B* **81**, 134402 (2010) DOI: [10.1103/PhysRevB.81.134402](https://doi.org/10.1103/PhysRevB.81.134402).

- [Eis54] J. Eisenstein: “Superconducting Elements”, *Rev. Mod. Phys.* **26**, 277 (1954) DOI: [10.1103/RevModPhys.26.277](https://doi.org/10.1103/RevModPhys.26.277).
- [Esc00] M. Eschrig: “Distribution functions in nonequilibrium theory of superconductivity and Andreev spectroscopy in unconventional superconductors”, *Phys. Rev. B* **61**, 9061 (2000) DOI: [10.1103/PhysRevB.61.9061](https://doi.org/10.1103/PhysRevB.61.9061).
- [Fan61] U. Fano: “Effects of Configuration Interaction on Intensities and Phase Shifts”, *Phys. Rev.* **124**, 1866 (1961) DOI: [10.1103/PhysRev.124.1866](https://doi.org/10.1103/PhysRev.124.1866).
- [Fer+05] J. Fernández-Rossier, D. Jacob, C. Untiedt and J. J. Palacios: “Transport in magnetically ordered Pt nanocontacts”, *Phys. Rev. B* **72**, 224418 (2005) DOI: [10.1103/PhysRevB.72.224418](https://doi.org/10.1103/PhysRevB.72.224418).
- [FF07] L. Fernández-Seivane and J. J. Ferrer: “Magnetic Anisotropies of Late Transition Metal Atomic Clusters”, *Phys. Rev. Lett.* **99**, 183401 (2007) DOI: [10.1103/PhysRevLett.99.183401](https://doi.org/10.1103/PhysRevLett.99.183401).
- [FGF07] L. Fernández-Seivane, V. M. García-Suárez and J. J. Ferrer: “Predictions for the formation of atomic chains in mechanically controllable break-junction experiments”, *Phys. Rev. B* **75**, 075415 (2007) DOI: [10.1103/PhysRevB.75.075415](https://doi.org/10.1103/PhysRevB.75.075415).
- [Fog00] M. Fogelström: “Josephson currents through spin-active interfaces”, *Phys. Rev. B* **62**, 11812 (2000) DOI: [10.1103/PhysRevB.62.11812](https://doi.org/10.1103/PhysRevB.62.11812).
- [Fra17] Fralock: *Cirlex, 20mil* (2017).
- [Fuj19] Fujifilm Electronic Materials: *Durimide 115A* (2019).
- [Gab+04] M. Gabureac, M. Viret, F. Ott and C. Fermon: “Magnetoresistance in nanocontacts induced by magnetostrictive effects”, *Phys. Rev. B* **69**, 100401 (2004) DOI: [10.1103/PhysRevB.69.100401](https://doi.org/10.1103/PhysRevB.69.100401).
- [Gar+05] V. M. García-Suárez, A. R. Rocha, S. W. Bailey, C. J. Lambert, S. Sanvito and J. Ferrer: “Conductance Oscillations in Zigzag Platinum Chains”, *Phys. Rev. Lett.* **95**, 256804 (2005) DOI: [10.1103/PhysRevLett.95.256804](https://doi.org/10.1103/PhysRevLett.95.256804).
- [Gar+09] V. M. García-Suárez, D. Z. Manrique, C. J. Lambert and J. Ferrer: “Anisotropic Magnetoresistance in Atomic Chains of Iridium and Platinum from First Principles”, *Phys. Rev. B* **79**, 060408 (2009) DOI: [10.1103/PhysRevB.79.060408](https://doi.org/10.1103/PhysRevB.79.060408).
- [Gar18] R. T. Garreis: “Magnetotransport measurements in aluminium nano loop arrays”, Universität Konstanz (2018).
- [Gav+10] P. Gava, A. Dal Corso, A. Smogunov and E. Tosatti: “Magnetism-induced ballistic conductance changes in palladium nanocontacts”, *Eur. Phys. J. B* **75**, 57 (2010) DOI: [10.1140/epjb/e2010-00046-1](https://doi.org/10.1140/epjb/e2010-00046-1).

- [GE96] G. Ganteför and W. Eberhardt: “Localization of 3 d and 4 d Electrons in Small Clusters: The “Roots” of Magnetism”, *Phys. Rev. Lett.* **76**, 4975 (1996) DOI: [10.1103/PhysRevLett.76.4975](https://doi.org/10.1103/PhysRevLett.76.4975).
- [GL50] V. L. Ginzburg and L. D. Landau: “To the Theory of Superconductivity”, *J. Exp. Theor. Phys.* **20**, 1064 (1950).
- [GM12] R. Gross and A. Marx: *Festkörperphysik*, Oldenbourg (2012).
- [GM87] J. K. Gimzewski and R. Möller: “Transition from the tunneling regime to point contact studied using scanning tunneling microscopy”, *Phys. Rev. B* **36**, 1284 (1987) DOI: [10.1103/PhysRevB.36.1284](https://doi.org/10.1103/PhysRevB.36.1284).
- [Häf+08] M. Häfner, J. K. Vilja, D. Frustaglia, F. Pauly, M. Dreher, P. Nielaba and J. C. Cuevas: “Theoretical study of the conductance of ferromagnetic atomic-sized contacts”, *Phys. Rev. B* **77**, 104409 (2008) DOI: [10.1103/PhysRevB.77.104409](https://doi.org/10.1103/PhysRevB.77.104409).
- [Ham18] S. Hambach: “Elektronischer Transport durch Einzelmolekülkontakte mit magnetischen Molekülen”, Universität Konstanz (2018).
- [HBB34] W. J. de Haas, J. de Boer and G. J. van den Berg: “The electrical resistance of gold, copper and lead at low temperatures”, *Physica* **1**, 1115 (1934) DOI: [10.1016/S0031-8914\(34\)80310-2](https://doi.org/10.1016/S0031-8914(34)80310-2).
- [Her+13] M. Herz, S. Bouvron, E. Ćavar, M. Fonin, W. Belzig and E. Scheer: “Fundamental quantum noise mapping with tunnelling microscopes tested at surface structures of subatomic lateral size”, *Nanoscale* **5**, 9978 (2013) DOI: [10.1039/C3NR02216A](https://doi.org/10.1039/C3NR02216A).
- [Hew93] A. C. Hewson: *The Kondo Problem to Heavy Fermions*, Cambridge University Press (1993).
- [HO85] K.-H. Hellwege and J. L. Olsen: *Landolt-Börnstein - Group III Condensed Matter 15b (Metals: Electronic Transport Phenomena · Electrical Resistivity, Thermoelectrical Power and Optical Properties)*, Springer (1985).
- [Hof08] R. Hoffmann: “Conductance of gold nanojunctions thinned by electromigration”, *Appl. Phys. Rev.* **93**, 043118 (2008) DOI: [10.1063/1.2965121](https://doi.org/10.1063/1.2965121).
- [Hof17] R. Hoffmann-Vogel: “Electromigration and the structure of metallic nanocontacts”, *Appl. Phys. Rev.* **4**, 031302 (2017) DOI: [10.1063/1.4994691](https://doi.org/10.1063/1.4994691).
- [HVC09] M. Häfner, J. K. Vilja and J. C. Cuevas: “Theory of anisotropic magnetoresistance in atomic-sized ferromagnetic metal contacts”, *Phys. Rev. B* **79**, 140410 (2009) DOI: [10.1103/PhysRevB.79.140410](https://doi.org/10.1103/PhysRevB.79.140410).
- [Ien+12] K. Ienaga, N. Nakashima, Y. Inagaki, H. Tsujii, T. Kimura and T. Kawae: “Study of Ferromagnetic Transition in Pd Nanometer-Scale Constrictions Using a Mechanically Controllable Break Junction Technique”, *Appl. Phys. Lett.* **101**, 123114 (2012) DOI: [10.1063/1.4754565](https://doi.org/10.1063/1.4754565).

- [Isl+17] M. S. Islam, H. Takata, K. Ienaga, Y. Inagaki, H. Tsujii and T. Kawae: “Fano profiles in palladium nanoconstrictions”, *Solid State Comm.* **262**, 16 (2017) DOI: [10.1016/j.ssc.2017.06.004](https://doi.org/10.1016/j.ssc.2017.06.004).
- [Jan77] J. F. Janak: “Uniform susceptibilities of metallic elements”, *Phys. Rev. B* **16**, 255 (1977) DOI: [10.1103/PhysRevB.16.255](https://doi.org/10.1103/PhysRevB.16.255).
- [Jos62] B. D. Josephson: “Possible new effect in superconductive tunnelling”, *Phys. Lett.* **1**, 251 (1962) DOI: [10.1016/0031-9163\(62\)91369-0](https://doi.org/10.1016/0031-9163(62)91369-0).
- [Kel15] M. Keller: “Magnetsiche Ordnung und magnetische Anisotropie in Atomaren Ketten und Einatom-Kontakten” (2015).
- [KM09] T. Kizuka and K. Monna: “Atomic configuration, conductance, and tensile force of platinum wires of single-atom width”, *Phys. Rev. B* **80**, 205406 (2009) DOI: [10.1103/PhysRevB.80.205406](https://doi.org/10.1103/PhysRevB.80.205406).
- [Kog96] S. Kogan: *Electronic noise and fluctuations in solids*, Cambridge University Press (1996).
- [Kon64] J. Kondo: “Resistance Minimum in Dilute Magnetic Alloys”, *Prog. Theor. Phys.* **32**, 37 (1964) DOI: [10.1143/PTP.32.37](https://doi.org/10.1143/PTP.32.37).
- [KSK85] R. J. P. Keijser, O. I. Shklyarevskii and H. van Kempen: “Two-level-system-related zero-bias anomaly in point-contact spectra”, *Phys. Rev. B* **51**, 5628 (1985) DOI: [10.1103/PhysRevB.51.5628](https://doi.org/10.1103/PhysRevB.51.5628).
- [Kum+12] M. Kumar, R. Avriller, A. L. Yeyati and J. M. van Ruitenbeek: “Detection of Vibration-Mode Scattering in Electronic Shot Noise”, *Phys. Rev. Lett.* **108**, 146602 (2012) DOI: [10.1103/PhysRevLett.108.146602](https://doi.org/10.1103/PhysRevLett.108.146602).
- [Kum+13a] M. Kumar, O. Tal, R. H. M. Smit, A. Smogunov, E. Tosatti and J. M. van Ruitenbeek: “Shot noise and magnetism of Pt atomic chains: Accumulation of points at the boundary”, *Phys. Rev. B* **88**, 245431 (2013) DOI: [10.1103/PhysRevB.88.245431](https://doi.org/10.1103/PhysRevB.88.245431).
- [Kum+13b] P. Kumar, R. Skomski, P. Manchanda and A. Kashyap: “Ab-initio study of anisotropy and nonuniaxial anisotropy coefficients in Pd nanochains”, *Chem. Phys. Lett.* **583**, 109 (2013) DOI: [10.1016/j.cplett.2013.07.069](https://doi.org/10.1016/j.cplett.2013.07.069).
- [KYN06] Z. K. Keane, L. H. Yu and D. Natelson: “Magnetoresistance of atomic-scale electromigrated nickel nanocontacts”, *Appl. Phys. Lett.* **88**, 062514 (2006) DOI: [10.1063/1.2172232](https://doi.org/10.1063/1.2172232).
- [Lan70] R. Landauer: “Electrical resistance of disordered one-dimensional lattices”, *Phil. Mag.* **21**, 863 (1970) DOI: [10.1080/14786437008238472](https://doi.org/10.1080/14786437008238472).
- [Lee95] E. W. Lee: “Magnetostriction and Magnetomechanical Effects”, *Rep. Prog. Phys.* **18**, 184 (1995) DOI: [10.1088/0034-4885/18/1/305](https://doi.org/10.1088/0034-4885/18/1/305).

- [Li+98] J. Li, W.-D. Schneider, R. Berndt and B. Delley: "Kondo Scattering Observed at a Single Magnetic Impurity", *Phys. Rev. Lett.* **80**, 2893 (1998) DOI: [10.1103/PhysRevLett.80.2893](https://doi.org/10.1103/PhysRevLett.80.2893).
- [Lor18] T. Lorenz: "Wechselspiel von Vielteilchen-Transport und Ladungseffekten in supraleitenden Einzelelektronentransistoren", Universität Konstanz (2018).
- [LSS18] T. Lorenz, S. Sprenger and E. Scheer: "Coulomb Blockade and Multiple Andreev Reflection in a Superconducting Single-Electron Transistor", *J. Low Temp. Phys.* **191**, 301 (2018) DOI: [10.1007/s10909-017-1837-4](https://doi.org/10.1007/s10909-017-1837-4).
- [Lum+18] O. S. Lumbroso, L. Simine, A. Nitzan, D. Segal and O. Tal: "Electronic noise due to temperature differences in atomic-scale junctions", *Nature* **562**, 240 (2018) DOI: [10.1038/s41586-018-0592-2](https://doi.org/10.1038/s41586-018-0592-2).
- [Mad+98] V. Madhavan, W. Chen, T. Jamneala, M. F. Crommie and N. S. Wingreen: "Tunneling into a Single Magnetic Atom: Spectroscopic Evidence of the Kondo Resonance", *Science* **280**, 567 (1998) DOI: [10.1126/science.280.5363.567](https://doi.org/10.1126/science.280.5363.567).
- [Mil02] E. Milotti: "1/f noise: a pedagogical review", *arXiv*, 0204033 (2002).
- [MK06] T. Matsuda and T. Kizuka: "Palladium Wires of Single Atom Width as Mechanically Controlled Switching Devices", *Jpn. J. Appl. Phys.* **45**, L1337 (2006) DOI: [10.1143/JJAP.45.L1337](https://doi.org/10.1143/JJAP.45.L1337).
- [MLC01] A. Martín-Rodero, A. Levy-Yeyati and J. C. Cuevas: "Transport properties of normal and ferromagnetic atomic-size constrictions with superconducting electrodes", *Physica C* **352**, 67 (2001) DOI: [10.1016/S0921-4534\(00\)01679-8](https://doi.org/10.1016/S0921-4534(00)01679-8).
- [MM89] V. L. Moruzzi and P. M. Marcus: "Magnetism in fcc rhodium and palladium", *Phys. Rev. B* **39**, 471 (1989) DOI: [10.1103/PhysRevB.39.471](https://doi.org/10.1103/PhysRevB.39.471).
- [Mok+06] Y. Mokrousov, G. Bihlmayer, S. Heinze and S. Blügel: "Giant Magnetocrystalline Anisotropies of 4d Transition-Metal Monowires", *Phys. Rev. Lett.* **96**, 147201 (2006) DOI: [10.1103/PhysRevLett.96.147201](https://doi.org/10.1103/PhysRevLett.96.147201).
- [Moo65] G. E. Moore: "Cramming more components onto integrated circuits" **38**, 114 (1965).
- [Mu+19] A. Mu, O. S. Lumbroso, O. Tal and D. Segal: "Origin of the Anomalous Electronic Shot Noise in Atomic-Scale Junctions", *J. Phys. Chem. C* **123**, 23853 (2019) DOI: [10.1021/acs.jpcc.9b06766](https://doi.org/10.1021/acs.jpcc.9b06766).
- [Mül90] R. Müller: *Rauschen*, Springer (1990).
- [NCL00] J. Nygård, D. H. Cobden and P. E. Lindelof: "Kondo physics in carbon nanotubes", *Nature* **408**, 342 (2000) DOI: [10.1038/35042545](https://doi.org/10.1038/35042545).

- [NN00] K. Nakanishi and Y. O. Nakamura: “Effect of a domain wall on conductance quantization in a ferromagnetic nanowire”, *Phys. Rev. B* **61**, 11278 (2000) DOI: [10.1103/PhysRevB.61.11278](https://doi.org/10.1103/PhysRevB.61.11278).
- [NRK04] T. Nautiyal, T. H. Rho and K. S. Kim: “Nanowires for spintronics: A study of transition-metal elements of groups 8 - 10”, *Phys. Rev. B* **69**, 193404 (2004) DOI: [10.1103/PhysRevB.69.193404](https://doi.org/10.1103/PhysRevB.69.193404).
- [Oct+83] M. Octavio, M. Tinkham, G. E. Blonder and T. M. Klapwijk: “Subharmonic energy-gap structure in superconducting constrictions”, *Phys. Rev. B* **27**, 6739 (1983) DOI: [10.1103/PhysRevB.27.6739](https://doi.org/10.1103/PhysRevB.27.6739).
- [Ono+99] T. Ono, Y. Ooka, H. Miyajima and Y. Otani: “ $2e^2/h$ to e^2/h switching of quantum conductance associated with a change in nanoscale ferromagnetic domain structure”, *Appl. Phys. Lett.* **75**, 1622 (1999) DOI: [10.1063/1.124774](https://doi.org/10.1063/1.124774).
- [PF18] S. Pradhan and J. Fransson: “Shot noise as a probe of spin-correlated transport through single atoms”, *Phys. Rev. B* **97**, 115409 (2018) DOI: [10.1103/PhysRevB.97.115409](https://doi.org/10.1103/PhysRevB.97.115409).
- [Pob96] F. Pobell: *Matter and methods at low temperatures*, Springer (1996).
- [Poo+07] C. P. Poole, H. A. Farach, R. J. Creswick and R. Prozorov: *Superconductivity*, Academic Press (2007).
- [Pos+96] N. van der Post, F. L. Mettes, J. A. Mydosh, J. M. van Ruitenbeek and I. K. Yanson: “Size dependence of Kondo scattering in point contacts: Fe impurities in Cu”, *Phys. Rev. B* **53**, R476 (1996) DOI: [10.1103/PhysRevB.53.R476](https://doi.org/10.1103/PhysRevB.53.R476).
- [Pre+19] M. W. Prestel, M. F. Ritter, A. Di Bernardo, T. Pietsch and E. Scheer: “Tuning the magnetic anisotropy energy of atomic wires”, *Phys. Rev. B* **100**, 214439 (2019) DOI: [10.1103/PhysRevB.100.214439](https://doi.org/10.1103/PhysRevB.100.214439).
- [Qua+07] C. H. L. Quay, J. Cumings, S. J. Gamble, R. de Picciotto, H. Kataura and D. Goldhaber-Gordon: “Magnetic field dependence of the spin- $\frac{1}{2}$ and spin-1 Kondo effects in a quantum dot”, *Phys. Rev. B* **76**, 245311 (2007) DOI: [10.1103/PhysRevB.76.245311](https://doi.org/10.1103/PhysRevB.76.245311).
- [RB92] D. C. Ralph and R. A. Buhrman: “Observations of Kondo scattering without magnetic impurities: A point contact study of two-level tunneling systems in metals”, *Phys. Rev. Lett.* **69**, 2118 (1992) DOI: [10.1103/PhysRevLett.69.2118](https://doi.org/10.1103/PhysRevLett.69.2118).
- [RB94] D. C. Ralph and R. A. Buhrman: “Kondo-assisted and resonant tunneling via a single charge trap: A realization of the Anderson model out of equilibrium”, *Phys. Rev. Lett.* **72**, 3401 (1994) DOI: [10.1103/PhysRevLett.72.3401](https://doi.org/10.1103/PhysRevLett.72.3401).
- [Ree08] M. A. Reed: “Inelastic electron tunneling spectroscopy”, *Mater. Today* **11**, 46 (2008) DOI: [10.1016/S1369-7021\(08\)70238-4](https://doi.org/10.1016/S1369-7021(08)70238-4).

- [Req+16] R. Requist, P. P. Baruselli, A. Smogunov, M. Fabrizio, S. Modesti and E. Tosatti: “Metallic, magnetic and molecular nanocontacts”, *Nat. Nano.* **11**, 499 (2016) DOI: [10.1038/nano.2016.55](https://doi.org/10.1038/nano.2016.55).
- [Rit18] M. F. Ritter: “Transport Measurements on Atomic Contacts and Chains of Iridium”, Universität Konstanz (2018).
- [RK06] M. Ryu and T. Kizuka: “Structure, Conductance and Strength of Iridium Wires of Single Atom Width”, *Jpn. J. Appl. Phys.* **45**, 8952 (2006) DOI: [10.1143/JJAP.45.8952](https://doi.org/10.1143/JJAP.45.8952).
- [RKD93] B. V. Reddy, S. N. Khanna and B. I. Dunlap: “Giant magnetic moments in 4d clusters”, *Phys. Rev. Lett.* **70**, 3323 (1993) DOI: [10.1103/PhysRevLett.70.3323](https://doi.org/10.1103/PhysRevLett.70.3323).
- [Rom+09] M. A. Romero, S. C. Gómez-Carrillo, P. G. Bolcatto and E. C. Goldberg: “Spin Fluctuation Effects on the Conductance Through a Single Pd Atom Contact”, *J.Phys.: Condens. Matter* **21**, 215602 (2009) DOI: [10.1088/0953-8984/21/21/215602](https://doi.org/10.1088/0953-8984/21/21/215602).
- [RU01] V. Rodrigues and D. Ugarte: “Real-time imaging of atomistic process in one-atom-thick metal junctions”, *Phys. Rev. B* **63**, 073405 (2001) DOI: [10.1103/PhysRevB.63.073405](https://doi.org/10.1103/PhysRevB.63.073405).
- [Rub+01] G. Rubio-Bollinger, S. R. Bahn, N. Agrait, K. W. Jacobsen and S. Vieira: “Mechanical Properties and Formation Mechanisms of a Wire of Single Gold Atoms”, *Phys. Rev. Lett.* **87**, 026101 (2001) DOI: [10.1103/PhysRevLett.87.026101](https://doi.org/10.1103/PhysRevLett.87.026101).
- [Rui+96] J. M. van Ruitenbeek, A. Alvarez, I. Piñeyro, C. Graumann, P. Joyez, M. Devoret, D. Esteve and C. Urbina: “Adjustable nanofabricated atomic size contacts”, *Rev. Sci. Inst* **67**, 108 (1996) DOI: [10.1063/1.1146558](https://doi.org/10.1063/1.1146558).
- [Sab+12] C. Sabater, C. Untiedt, J. J. Palacios and M. J. Caturla: “Mechanical Annealing of Metallic Electrodes at the Atomic Scale”, *Phys. Rev. Lett.* **108**, 205502 (2012) DOI: [10.1103/PhysRevLett.108.205502](https://doi.org/10.1103/PhysRevLett.108.205502).
- [Sah+11] P. K. Sahota, R. Skomski, A. Enders, D. J. Sellmyer and A. Kashyap: “Anisotropy of zigzag chains of palladium”, *J. Appl. Phys.* **109**, 07E322 (2011) DOI: [10.1063/1.3559505](https://doi.org/10.1063/1.3559505).
- [Sam+03] B. Sampedro, P. Crespo, A. Hernando, R. Litrán, J. C. Sánchez López, A. Fernández, J. Ramírez, J. Fonzález Calbet and M. Vallet: “Ferromagnetism in fcc Twinned 2.4 nm Size Pd Nanoparticles”, *Phys. Rev. Lett.* **91**, 237203 (2003) DOI: [10.1103/PhysRevLett.91.237203](https://doi.org/10.1103/PhysRevLett.91.237203).
- [Sch+01] E. Scheer, W. Belzig, Y. Naveh, M. H. Devoret, D. Esteve and C. Urbina: “Proximity Effect and Multiple Andreev Reflections in Gold Atomic Contacts”, *Phys. Rev. Lett.* **86**, 284 (2001) DOI: [10.1103/PhysRevLett.86.284](https://doi.org/10.1103/PhysRevLett.86.284).

- [Sch+02] E. Scheer, W. Belzig, Y. Naveh and C. Urbina: “Probing the conduction channels of gold atomic-size contacts: proximity effect and multiple Andreev Reflections”, *Adv. Solid State Phys.* **42**, 107 (2002) DOI: [10.1007/3-540-45618-X_9](https://doi.org/10.1007/3-540-45618-X_9).
- [Sch+97] E. Scheer, P. Joyez, D. Esteve, C. Urbina and M. Devoret: “Conduction Channel Transmissions of Atomic-Size Aluminum Contacts”, *Phys. Rev. Lett.* **78**, 3535 (1997) DOI: [10.1103/PhysRevLett.78.3535](https://doi.org/10.1103/PhysRevLett.78.3535).
- [Sch+98] E. Scheer, N. Agraït, J. C. Cuevas, A. L. Yeyati, B. Ludoph, A. Martín-Rodero, G. R. Bollinger, J. M. van Ruitenbeek and C. Urbina: “The signature of chemical valence in the electrical conduction through a single-atom contact”, *Nature* **394**, 154 (1998) DOI: [10.1038/28112](https://doi.org/10.1038/28112).
- [Sch10] C. Schirm: “Einfluss hoher Ströme auf atomare Kontakte”, Universität Konstanz (2010).
- [Sch19] W. Schottky: “Über spontane Stromschwankungen in verschiedenen Elektrizitätsleitern”, *Ann. Phys.* **362**, 541 (1919) DOI: [10.1002/andp.19183622304](https://doi.org/10.1002/andp.19183622304).
- [SDT08] A. Smogunov, A. Dal Corso and E. Tosatti: “Magnetic Phenomena, Spin-Orbit Effects, and Landauer Conductance in Pt Nanowire Contacts: Density-Functional Theory Calculations”, *Phys. Rev. B* **78**, 014423 (2008) DOI: [10.1103/PhysRevB.78.014423](https://doi.org/10.1103/PhysRevB.78.014423).
- [Shi+07] S.-F. Shi, K. I. Bolotin, F. Kuemmeth and D. C. Ralph: “Temperature dependence of anisotropic magnetoresistance and atomic rearrangements in ferromagnetic metal break junctions”, *Phys. Rev. B* **76**, 184438 (2007) DOI: [10.1103/PhysRevB.76.184438](https://doi.org/10.1103/PhysRevB.76.184438).
- [Sme+08] K. M. Smelova, D. I. Bazhanov, V. S. Stepanyuk, W. Hergert, A. M. Saletsky and P. Bruno: “Interplay Between Magnetism and Structure in Atomic-Size Pd Contacts: *ab initio* Studies”, *Phys. Rev. B* **77**, 033408 (2008) DOI: [10.1103/PhysRevB.77.033408](https://doi.org/10.1103/PhysRevB.77.033408).
- [Smi+01] R. H. M. Smit, C. Untiedt, A. Yanson and J. M. van Ruitenbeek: “Common Origin for Surface Reconstruction and the Formation of Chains of Metal Atoms”, *Phys. Rev. Lett.* **87**, 266102 (2001) DOI: [10.1103/PhysRevLett.87.266102](https://doi.org/10.1103/PhysRevLett.87.266102).
- [Smi+03] R. H. M. Smit, C. Untiedt, G. Rubio-Bollinger, R. C. Segers and J. M. van Ruitenbeek: “Observation of a Parity Oscillation in the Conductance of Atomic Wires”, *Phys. Rev. Lett.* **91**, 076805 (2003) DOI: [10.1103/PhysRevLett.91.076805](https://doi.org/10.1103/PhysRevLett.91.076805).
- [Smo+08] A. Smogunov, A. Dal Corso, A. Delin, R. Weht and E. Tosatti: “Colossal Magnetic Anisotropy of Monatomic Free and Deposited Platinum Nanowires”, *Nat. Nano.* **3**, 22 (2008) DOI: [10.1038/nano.2007.419](https://doi.org/10.1038/nano.2007.419).

- [Sok+07] A. Sokolov, C. Zhang, E. Y. Tsymbal, J. Redepenning and B. Doudin: “Quantized magnetoresistance in atomic-size contacts”, *Nat. Nano.* **2**, 171 (2007) DOI: [10.1038/nnano.2007.36](https://doi.org/10.1038/nnano.2007.36).
- [Sou+98] R. J. Soulen, J. M. Byers, M. S. Osofsky, B. Nadgorny, R. Ambrose, et al.: “Measuring the Spin Polarization of a Metal with a Superconducting Point Contact”, *Science* **282**, 85 (1998) DOI: [10.1126/science.282.5386.85](https://doi.org/10.1126/science.282.5386.85).
- [Spr20] S. Sprenger: “Interplay between charging effects and multi-particle transport in superconducting single electron transistors with tunable junctions”, Universität Konstanz (2020).
- [SR07] S.-F. Shi and D. C. Ralph: “Atomic motion in ferromagnetic break junctions”, *Nat. Nano* **2**, 522 (2007) DOI: [10.1038/nnano.2007.251a](https://doi.org/10.1038/nnano.2007.251a).
- [SSF01] E. Z. da Silva, A. J. R. da Silva and A. Fazzio: “How Do Gold Nanowires Break?”, *Phys. Rev. Lett.* **87**, 256102 (2001) DOI: [10.1103/PhysRevLett.87.256102](https://doi.org/10.1103/PhysRevLett.87.256102).
- [Sto38] E. C. Stoner: “Collective electron ferromagnetism”, *Proc. R. Soc. Lond. A* **165**, 372 (1938) DOI: [10.1098/rspa.1938.0066](https://doi.org/10.1098/rspa.1938.0066).
- [Sto39] E. C. Stoner: “Collective Electron Ferromagnetism. II. Energy and Specific Heat”, *Proc. R. Soc. Lond. A* **169**, 339 (1939) DOI: [10.1098/rspa.1939.0003](https://doi.org/10.1098/rspa.1939.0003).
- [Str+15] F. Strigl, C. Espy, M. Bückle, E. Scheer and T. Pietsch: “Emerging magnetic order in platinum atomic contacts and chains”, *Nat. Comm.* **6**, 6172 (2015) DOI: [10.1038/ncomms7172](https://doi.org/10.1038/ncomms7172).
- [Str+16] F. Strigl, M. Keller, D. Weber, T. Pietsch and E. Scheer: “Magnetism in Pd: Magnetoconductance and transport spectroscopy of atomic contacts”, *Phys. Rev. B* **94**, 144431 (2016) DOI: [10.1103/PhysRevB.94.144431](https://doi.org/10.1103/PhysRevB.94.144431).
- [Str10] F. Strigl: “Regelbare atomare Kontakte aus Platin”, Universität Konstanz (2010).
- [Str16] F. Strigl: “Über den Einfluss magnetischer Korrelationen auf den Ladungstransport durch atomare Kontakte aus Übergangsmetallen”, Universität Konstanz (2016).
- [Str19] M. Strohmeier: “Herstellung und elektrischer Transport in atomaren Kontakten aus Selten-Erd- und Übergangsmetallen”, Universität Konstanz (2019).
- [Str79] B. Stritzker: “Superconductivity in Irradiated Palladium”, *Phys. Rev. Lett.* **42**, 1769 (1979) DOI: [10.1103/PhysRevLett.42.1769](https://doi.org/10.1103/PhysRevLett.42.1769).
- [Tai] Taiwan Semiconductor: *Glass Passivated Rectifiers: 6A05G thru 6A100G*.
- [Tex20] Texas Instruments: *OPAx211 1.1nV/ $\sqrt{\text{Hz}}$ Noise, Low Power, Precision Operational Amplifiers* (2020).

- [TG10] J. C. Tung and G. Y. Guo: “Magnetic moment and magnetic anisotropy of linear and zigzag 4d and 5d transition metal nanowires: First-principles calculations”, *Phys. Rev. B* **81**, 094422 (2010) DOI: [10.1103/PhysRevB.81.094422](https://doi.org/10.1103/PhysRevB.81.094422).
- [Tha+17] M. Thalmann, H.-F. Pernau, C. Strunk, E. Scheer and T. Pietsch: “Comparison of cryogenic low-pass filters”, *Rev. Sci. Instr.* **88**, 114703 (2017) DOI: [10.1063/1.4995076](https://doi.org/10.1063/1.4995076).
- [Thi+06] W. H. A. Thijssen, D. Marjenburgh, R. H. Bremmer and J. M. van Ruitenbeek: “Oxygen-Enhanced Atomic Chain Formation”, *Phys. Rev. Lett.* **96**, 026806 (2006) DOI: [10.1103/PhysRevLett.96.026806](https://doi.org/10.1103/PhysRevLett.96.026806).
- [Thi+08] A. Thiess, Y. Mokrousov, S. Blügel and S. Heinze: “Theory and Application of Chain Formation in Break Junctions”, *Nano Lett.* **8**, 2144 (2008) DOI: [10.1021/nl0800671](https://doi.org/10.1021/nl0800671).
- [Thi+09] A. Thiess, Y. Mokrousov, S. Heinze and S. Blügel: “Magnetically Hindered Chain Formation in Transition-Metal Break Junctions”, *Phys. Rev. Lett.* **103**, 217201 (2009) DOI: [10.1103/PhysRevLett.103.217201](https://doi.org/10.1103/PhysRevLett.103.217201).
- [Tin04] M. Tinkham: *Introduction to Superconductivity*, Dover Publications, Inc. (2004).
- [TMH10] A. Thiess, Y. Mokrousov and S. Heinze: “Competing Magnetic Anisotropies in Atomic-Scale Junctions”, *Phys. Rev. B* **81**, 054433 (2010) DOI: [10.1103/PhysRevB.81.054433](https://doi.org/10.1103/PhysRevB.81.054433).
- [TSR19] S. Tewari, C. Sabater and J. van Ruitenbeek: “Identification of vibration modes in single-molecule junctions by strong inelastic signals in noise”, *Nanoscale* **11**, 19462 (2019) DOI: [10.1039/c9nr05774a](https://doi.org/10.1039/c9nr05774a).
- [Unt+04] C. Untiedt, D. M. T. Dekker, D. Djukic and J. M. van Ruitenbeek: “Absence of magnetically induced fractional quantization in atomic contacts”, *Phys. Rev. B* **69**, 081401 (2004) DOI: [10.1103/PhysRevB.69.081401](https://doi.org/10.1103/PhysRevB.69.081401).
- [Vig80] P. B. Vigman: “Exact solution of s-d exchange model at T=0”, *Sov. Phys. JETP Lett.* **31**, 392 (1980).
- [Vir+02] M. Viret, S. Berger, M. Gabureac, O. F. D. Olligs, I. Petej, C. Fermon, G. Francinet and G. Le Goff: “Magnetoresistance through a single nickel atom”, *Phys. Rev. B* **66**, 220401 (2002) DOI: [10.1103/PhysRevB.66.220401](https://doi.org/10.1103/PhysRevB.66.220401).
- [Vir+06] M. Viret, M. Gabureac, O. F., C. Fermon, C. Barreteau and R. Guirado-Lopez: “Giant Anisotropic Magneto-Resistance in ferromagnetic atomic contacts”, *Eur. Phys. J. B* **51**, 1 (2006) DOI: [10.1140/epjb/e2006-00201-3](https://doi.org/10.1140/epjb/e2006-00201-3).
- [VKT13] R. Vardimon, M. Klionsky and O. Tal: “Experimental determination of conduction channels in atomic-scale conductors based on shot noise measurements”, *Phys. Rev. B* **88**, 161404 (2013) DOI: [10.1103/PhysRevB.88.161404](https://doi.org/10.1103/PhysRevB.88.161404).

- [Vro+05] S. A. G. Vrouwe, E. van der Giessen, S. J. van der Molen, D. Dulic, M. L. Trouwborst and B. J. van Wees: “Mechanics of lithographically defined break junctions”, *Phys. Rev. B* **71**, 035313 (2005) DOI: [10.1103/PhysRevB.71.035313](https://doi.org/10.1103/PhysRevB.71.035313).
- [VZ83] K. Vladár and A. Zawadowski: “Theory of the interaction between electrons and the two-level system in amorphous metals. I. Noncommutative model Hamiltonian and scaling of first order”, *Phys. Rev. B* **28**, 1564 (1983) DOI: [10.1103/PhysRevB.28.1564](https://doi.org/10.1103/PhysRevB.28.1564).
- [Wah+07] P. Wahl, P. Simon, L. Diekhöner, V. S. Stepanyuk, P. Bruno, M. A. Schneider and K. Kern: “Exchange Interaction between Single Magnetic Adatoms”, *Phys. Rev. Lett.* **98**, 056601 (2007) DOI: [10.1103/PhysRevLett.98.056601](https://doi.org/10.1103/PhysRevLett.98.056601).
- [WCT06] S. A. Wolf, A. Y. Chtchelkanova and D. M. Treger: “Spintronics—A retrospective and perspective”, *IBM J. Res. & Dev.* **50**, 101 (2006) DOI: [10.1147/rd.501.0101](https://doi.org/10.1147/rd.501.0101).
- [Web+78] R. A. Webb, J. B. Ketterson, W. P. Halperin, J. J. Vuillemin and N. B. Sandesara: “Very low temperature search for superconductivity in Pd, Pt, and Rh”, *J. Low Temp. Phys.* **32**, 659 (1978) DOI: [10.1007/BF00056650](https://doi.org/10.1007/BF00056650).
- [Wei+06] H.-X. Wei, T.-X. Wang, E. Clifford, R. M. Langford, X.-F. Han and J. M. D. Coey: “Magnetoresistance of nickel nanocontacts fabricated by different methods”, *J. Appl. Phys.* **99**, 08C512 (2006) DOI: [10.1063/1.2167061](https://doi.org/10.1063/1.2167061).
- [Wie94] R. Wiesendanger: *Scanning Probe Microscopy and Spectroscopy: Methods and Applications*, Cambridge University Press (1994).
- [Wil75] K. G. Wilson: “The renormalization group: Critical phenomena and the Kondo problem”, *Rev. Mod. Phys.* **47**, 773 (1975) DOI: [10.1103/RevModPhys.47.773](https://doi.org/10.1103/RevModPhys.47.773).
- [WW11] B. Wang and J. Wang: “Spin polarized I-V characteristics and shot noise of Pt atomic wires”, *Phys. Rev. B* **84**, 165401 (2011) DOI: [10.1103/PhysRevB.84.165401](https://doi.org/10.1103/PhysRevB.84.165401).
- [Yan+95] I. K. Yanson, V. V. Fison, R. Hesper, A. V. Khotkevich, J. M. Krans, J. A. Mydosh and J. M. van Ruitenbeek: “Size Dependence of Kondo Scattering in Point Contacts”, *Phys. Rev. Lett.* **74**, 302 (1995) DOI: [10.1103/PhysRevLett.74.302](https://doi.org/10.1103/PhysRevLett.74.302).
- [YR97] I. K. Yanson and J. M. van Ruitenbeek: “Do Histograms Constitute a Proof for Conductance Quantization?”, *Phys. Rev. Lett.* **79**, 2157 (1997) DOI: [10.1103/PhysRevLett.79.2157](https://doi.org/10.1103/PhysRevLett.79.2157).
- [YS86] I. K. Yanson and O. I. Shklyarevskij: “Point-contact spectroscopy of metallic alloys and compounds”, *Fiz. Nizk. Temp.* **12**, 899 (1986) [*Sov. J. Low Temp. Phys.* **12**, 509 (1986)].
- [Zha+14] B. Zhang, D. Wang, Z. Yang, L. Xu, R. Lui, P. Li and X. Li: “Non-collinear magnetic order and spin-orbit coupling effect in 4d transition metal monatomic chains”, *J. Mag. Mag. Mat.* **368**, 262 (2014) DOI: [10.1016/j.jmmm.2014.05.047](https://doi.org/10.1016/j.jmmm.2014.05.047).

- [Zha+95] J. Zhao, X. Chen, Q. Sun, F. Liu and G. Wang: “Critical Size for Magnetic–Non-magnetic Transition in Transition Metal Clusters”, *Eur. Phys. Lett.* **32**, 113 (1995)
DOI: [10.1209/0295-5075/32/2/004](https://doi.org/10.1209/0295-5075/32/2/004).
- [Zur18] Zurich Instruments: *HF2 User Manual - ziControl Edition* (2018).

Danksagung

Als erstes möchte ich Frau Prof. Dr. Elke Scheer für die Möglichkeit danken meine Doktorarbeit in ihrer Arbeitsgruppe anzufertigen. Sie war immer für neue Ideen für die Probenherstellung und die Konzeptionierung der Versuchsaufbauten offen. Ohne diese Freiheit und die guten Arbeitsbedingungen wäre es nicht möglich gewesen diese Arbeit anzufertigen.

Als nächstes möchte ich Herrn Prof. Dr. Wolfgang Belzig für das Zweitgutachten danken, sowie Herrn Prof. Dr. Peter Nielaba für die Bereitschaft, sich als Prüfer zur Verfügung zu stellen. Außerdem danke ich Herrn Prof. Dr. Paul Leiderer für die Möglichkeit, in seinem Aufbau Thermometer mit Hilfe des Heliumdampfdruckes zu testen, sowie für seine Bereitschaft sich als Prüfer zur Verfügung zu stellen.

Der Auf- und Umbau mehrerer Versuchsaufbauten wäre nicht ohne die Hilfe von Ansgar Fischer und Louis Kukk für die Mechanik sowie Harald Richter für die Elektronik möglich gewesen. Für die Umsetzung der Pläne und Änderungen danke ich allen Mitarbeitern der Wissenschaftlichen Werkstätten. Die Probenherstellung wäre nicht ohne die Unterstützung von Simon Haus möglich gewesen. Vielen Dank dafür.

Ich danke allen Mitgliedern der AG Scheer für die gute Arbeitsatmosphäre, die Kaffeerunden und die Besuche im Biergarten. Ganz besonders möchte ich meinen beiden Masterstudenten Markus Ritter und Marcel Strohmeier danken. Sie haben viele guten Ideen und noch mehr Zeit eingebracht, damit die Experimente durchgeführt werden konnten. Dr. Florian Strigl und Dr. Torsten Pietsch möchte ich für die Einführung in das wissenschaftliche Arbeiten und die AG Scheer danken. Ohne die Beiden hätte ich niemals eine Doktorarbeit begonnen. Ich kann nicht beschreiben, wie wichtig die nun schon 10 Jahre andauernde Freundschaft von Thomas Möller und Susanne Sprenger für diese Arbeit war, schon während des Studiums und dann erst recht in der AG Scheer. Die Laborarbeit und Diskussionen mit euch war immer anregend und lehrreich!

Ich danke der Carl-Zeiss Stiftung für das Doktoranden-Stipendium, ohne das die Doktorarbeit hätte nicht entstehen können.

Außerdem danke ich meiner Familie und meinen Freunden für die andauernde Unterstützung und die aufmunternden Worte. Als letztes möchte ich meiner Frau Katharina danken, dass sie das „Projekt“ Doktorarbeit immer mit unterstützt hat und immer für Gespräche über Tieftemperaturprobleme offen war. Auch wenn sie zu Beginn davon keine Ahnung hatte, ist so manche gute Idee in diesen Gesprächen entstanden.

Appendix A

Appendix

A.1 Noise Setup

The two devices of the noise setup, which might need some more information about the specifications and the additional noise, are the home-built adder and the IV converter. First, the adder is described and analyzed in terms of noise input. This device has been built by the electronic workshop of the university. The design is from M. Herz for noise measurements in a STM [Her+13].

A.1.1 Adder

The circuit diagram is shown in [figure A.1](#). Only one input is connected, so it is used as a voltage divider and a low-pass filter. To exclude any ground loops, the amplifier is powered by a battery pack. To reduce the noise input into the setup, a low-pass filter with cutoff frequency of $f_c = 16\text{Hz}$ is applied at the second operational amplifier. The first one divides the signal by a factor of 10, which allows for higher signals at the output of the sources. The two amplifier stages make the polarity of the output signal the same as the input.

To estimate the influence of the source and the adder on the noise, I made a full noise analysis for the adder including the noise of the source $e_{\text{source}} = 45\text{nV}/\sqrt{\text{Hz}}$. Due to the two stages of the adder, one can divide the analysis into two parts. One for the first operational amplifier (opamp) and one for the second. The equivalent circuit diagram for both stages is depicted in [figure A.2](#).

For the first stage one may exclude the disconnected input and neglect all capacitive influences. The different noise sources are:

e_α thermal noise of $R_1 = 33\text{k}\Omega$,

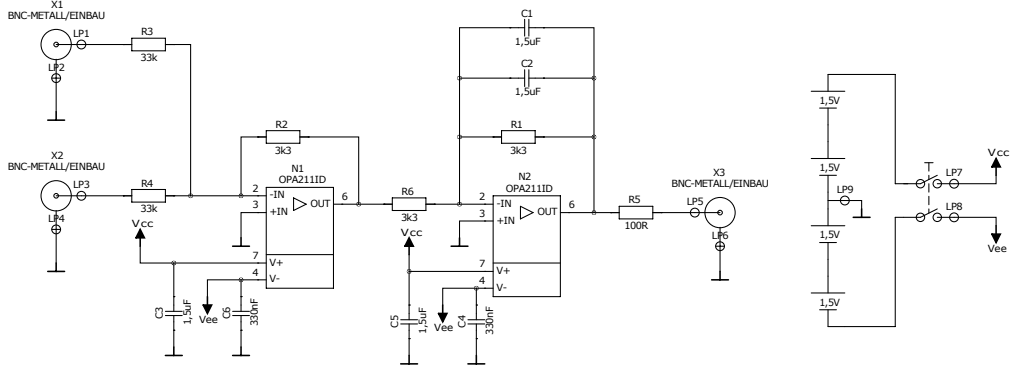


Figure A.1: The circuit diagram of the battery-powered adder with built-in low pass filter is shown. The cutoff frequency is 16 Hz. The design is from M. Herz, the diagram from the electronics workshop of the university. The 100 Ω resistor at the output was shorted to reduce the additional noise in the setup.

i_β input current noise of the opamp ($i_\beta = 1.7 \text{ nA}/\sqrt{\text{Hz}}$, [Tex20]),

e_γ input voltage noise of the opamp ($e_\gamma = 1.1 \text{ nV}/\sqrt{\text{Hz}}$, [Tex20]), and

e_δ thermal noise of $R_2 = 3.3 \text{ k}\Omega$.

At the output the different noise sources add up as

$$e_{\text{out}}^1 = \sqrt{\left(\frac{R_2}{R_1} e_{\text{source}}\right)^2 + \left(\frac{R_2}{R_1} e_\alpha\right)^2 + (R_2 i_\beta)^2 + \left(\frac{R_2}{R_1} e_\gamma\right)^2 + e_\delta^2} \quad (\text{A.1})$$

to a total of $10.6 \text{ nV}/\sqrt{\text{Hz}}$.

The second stage includes a total capacitance $C = 3 \mu\text{F}$ for filtering reasons. Therefore, one has to calculate with complex numbers. All given numbers are calculated for a frequency of 10 kHz. The filtering will increase for higher frequencies, lower frequencies are not interesting for the presented measurements. The following terminology is used: $X_1 = 3.3 \text{ k}\Omega$ resistor at the input, $X_2 = 3.3 \text{ k}\Omega$ feedback resistor, $X_3 = \frac{1}{i\omega C}$ impedance of the capacitance and $X_{2||3}$ impedance of X_2 parallel to X_3 . The noise sources are again:

e_{out}^1 noise from the previous stage,

$e_{\epsilon,\eta}$ thermal noise from $X_1 = X_2 = 3.3 \text{ k}\Omega$,

i_ζ input current noise of opamp ($i_\zeta = 1.7 \text{ nA}/\sqrt{\text{Hz}}$, [Tex20]), and

e_θ input voltage noise of the opamp ($e_\theta = 1.1 \text{ nV}/\sqrt{\text{Hz}}$, [Tex20]).

The 100 Ω resistor at the output of the second stage has been removed, since it is not filtered anymore and would add its full thermal noise. The noise contribution at the output $e_{\text{out}}^2 =$

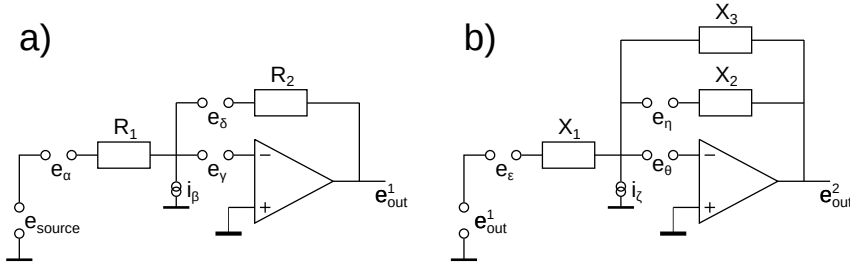


Figure A.2: The equivalent circuit diagram for both stages of the adder. The e_i indicate voltage sources and the i_i indicate current sources for the noise. They are labeled continuously with Greek letters.

W_u^{source} is then calculated via the sum of the squares of the absolute values.

$$e_{\text{out}}^2 = \sqrt{\left| \frac{X_2||3}{X_1} e_{\text{out}}^1 \right|^2 + \left| \frac{X_2||3}{X_1} e_\epsilon \right|^2 + \left| X_2||3 e_\zeta \right|^2 + \left| \frac{X_3}{X_2 + X_3} e_\eta \right|^2 + \left| \frac{X_2||3}{X_1} e_\theta \right|^2} \quad (\text{A.2})$$

For the already mentioned frequency $f = 10 \text{ kHz}$ the math leads to $e_{\text{out}}^2 \approx 23 \text{ pV}/\sqrt{\text{Hz}}$.

A.1.2 IV Converter

Measuring small currents with a high bandwidth is challenging. Therefore, a special amplifier, which was designed to fulfill the requirements of the setup, was used. The amplifier was designed and produced by “JanasCard” in Czech Republic. The key features are given in [table A.1](#). A more detailed description of the operating principle is given by the manufacturer¹.

gain	$1 \times 10^6 \text{ V/A}$	$1 \times 10^7 \text{ V/A}$
bandwidth	2 MHz	450 kHz
output swing	$\pm 10 \text{ V}$ @ load $> 2 \text{ k}\Omega$	
output impedance	50Ω	
input bias	$< 5 \text{ pA}$	
input voltage noise	typ. $1 \text{ nV}/\sqrt{\text{Hz}}$	
input resistance	100Ω	
acceptable input capacitance	max. 150 pF	

Table A.1: The specifications of the IV converter IVF10M by JanasCard.

¹<http://janascard.cz/PDF/Ultralownoisehighbandwidthtransimpedanceamplifiers.pdf> in section 4: “A composite ultra-low noise TIA”.

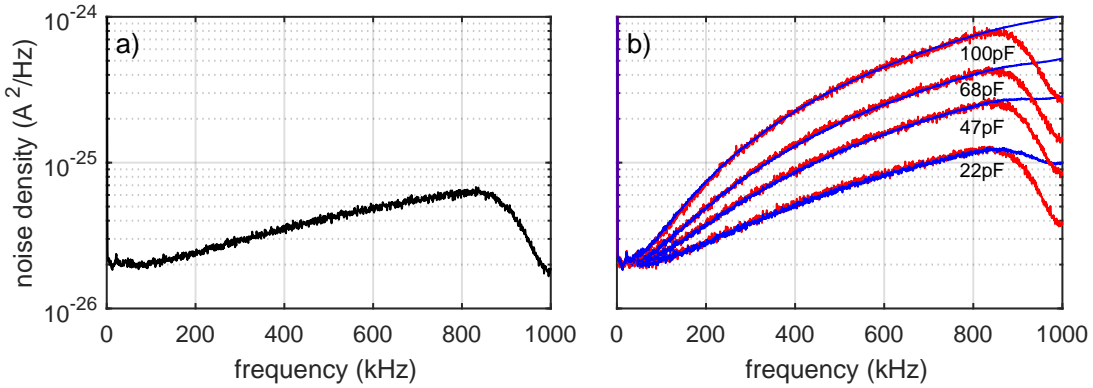


Figure A.3: In **a)**, the measured input current noise for the IV converter in the frequency regime up to 1 MHz is depicted. The roll-off starting at 800 kHz is caused by the settings of the oscilloscope. In **b)**, the measured spectra for four different capacitors (with nominal values of 22, 47, 68, 100 pF) at the input (in red) and the corresponding modeling with the parameter given in the text (in blue) are shown.

To calculate the noise of the sample, one has to know the contributions of the amplifier. As already written in [section 3.4.3](#), there are two contributions from the amplifier. One is the input current noise W_i^{amp} , which can be measured easily by recording a spectrum with an open input. To block radiation, the input is covered by a cap. The corresponding spectrum is depicted in [figure A.3](#).

The second contribution, the input voltage noise W_u^{amp} , is not that easy to determine. Therefore, the idea of Cron [[Cro01](#)] is adapted to an IV converter. Any resistor at the input will add some voltage noise to circuit, which is much higher than the expected value for the amplifier. Hence, one uses capacitors between the input and ground. The resulting spectra consist of the input current noise and the input voltage noise, which is converted to a current noise via the impedance of the capacitor and the input capacity of the amplifier $Z = 1/(i\omega(C_{\text{amp}} + C_{\text{add}}))$. The spectrum at the output of the amplifier can be modeled by

$$W^{\text{total}} = W_i^{\text{amp}} + \frac{W_u^{\text{amp}}}{|Z|^2}. \quad (\text{A.3})$$

Fitting the data for all four capacitors with the same input capacitance and input voltage noise leads to $C_{\text{amp}} = 6.5 \text{ pF}$ and $W_u^{\text{amp}}(f) = (2.82 \cdot 10^{-18} - 6.59 \cdot 10^{-25} \cdot f) \text{ V}^2/\text{Hz}$. The measured data as well as the modeling is depicted in [figure A.3](#).

A.2 MAR Setup

A.2.1 Adder MAR Setup

For the MAR setup only an adder was built, the corresponding circuit is presented in [figure A.4](#). This adder is used to add a DC voltage at “IN 1:1” and an AC voltage at “IN 1:10”. The “IN 1:10” is equipped with a high-pass filter at the input for blocking DC components coming from the lock-in amplifier. Additionally this input also reduces the voltage by a factor of 10 to allow for smaller AC signals in the setup². Both signals are added together with an offset voltage, which is adjustable via a potentiometer, for compensating offsets from input devices. The added signals are then fed into a differential amplifier to generate a symmetrical output. Just in front of the output, a relay switch can clamp the output to ground. This relay is switched by a 5 V signal at an additional input. Clamping the output to ground is used to measure the offset of the voltage amplifiers in the setup.

A.2.2 Chirp Noise of the Voltage Source

After first test measurements without a well formed superconducting *IV* curves in the tunneling regime, the signals of the different devices have been checked. At the output of the low-noise voltage source “Agilent B2962A” a chirp noise, depicted in [figure A.5](#) was measured. To remove this parasitic signal, a passive LCR-filter was attached directly at the output of the voltage source. This filter is shown in [figure A.5](#). It removes the chirp and leaves a flat signal. The 3 dB point is at 70 Hz. The residual noise is filtered by the adder and the cryogenic filters.

A.2.3 Shift in Magnetic Field

While measuring the first samples in aluminium, in the BlueFors, the cryostat for measuring MAR, one always measured a shift in the magnetic sweeps to determine the critical field of the samples. As shown in [figure A.6 a\)](#) this shift is always in the negative direction with slightly different values. Since the origin of that shift was not clear and I wanted to exclude the presence of any ferromagnetic material in the vicinity of the sample, several investigations have been performed. After replacing all ferromagnetic materials below the MXC, the shift was still present, therefore other sources have been considered. Since the shift also appeared in another experiment carried out in the same cryostat [[Gar18](#)], we directed our attention to the power supply for the magnet.

²Some AC sources or reference signals of lock-in amplifiers have a lower limit in the mV range.

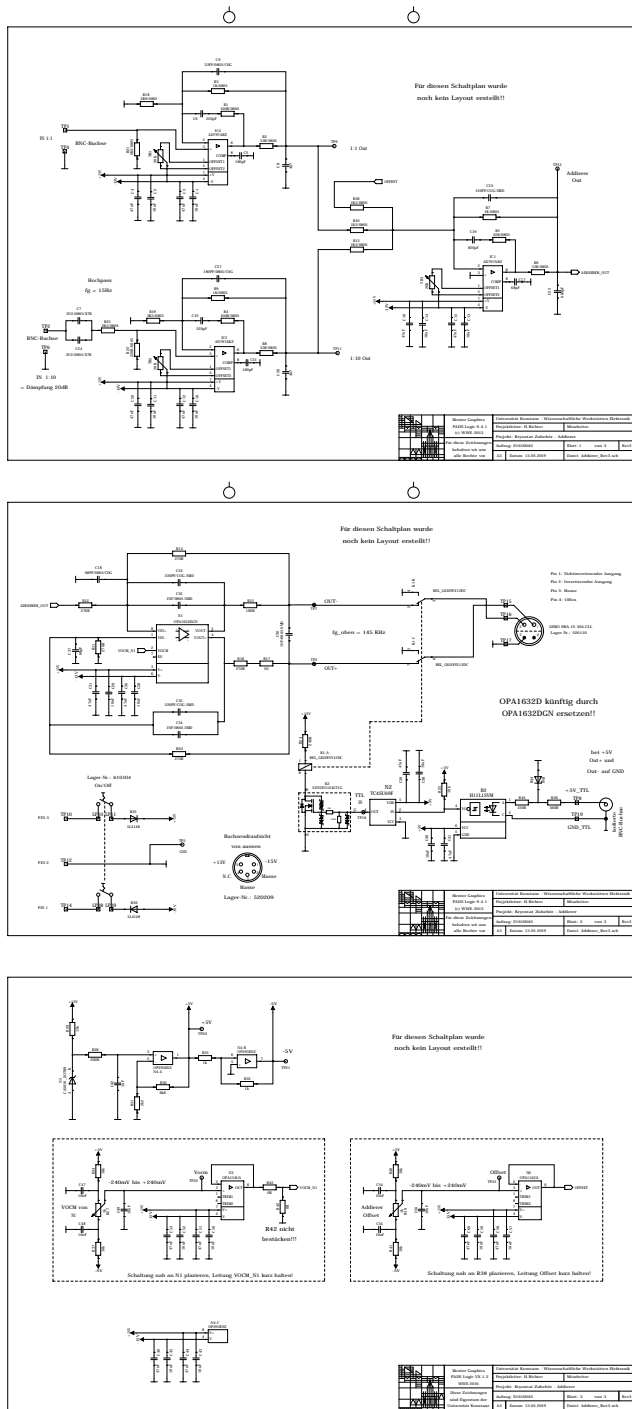


Figure A.4: The circuit diagram of the adder for the measurement with superconducting samples: The design was made by H. Richter from the electronics workshop of the university.

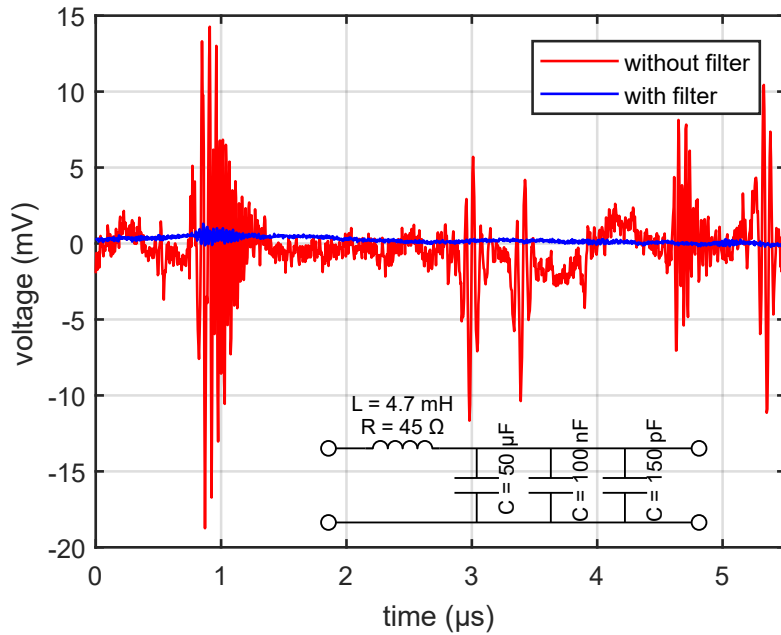


Figure A.5: The ‘Agilent B2962A’ adds a periodic repeated high frequency noise to the DC voltage. This additional signal is shown in red. It repeats every $5.7\text{ }\mu\text{s}$. To cut this signal a LCR-filter shown in the inset, is attached to the output of the device. The 3 dB frequency is at 70 Hz. Most parts of the unwanted signal are filtered out with this filter, as demonstrated by the blue curve.

To check the output of the power supply, an ampere meter was hooked up between the power supply and the superconducting magnet. In parallel, the resistance of an atomic aluminium contact was monitored with the setup. The results are plotted in figure A.6 b) as a function of the measured current through the superconducting magnet. As one clearly sees, a shift exists between zero current (and minimum resistance) and zero field reading of the power supply. In the example shown here, this shift amounts to about -7 mA or -0.75 mT , depending on the exact definition of the zero. This value is in agreement with the shift measured by investigating the critical fields of various samples. But one also has to mention, that the exact value changes when the power supply is switched off and on again, and temperature plays a roll as well. So for consecutive measurements the exact shift was measured after cooldown (and thermalization of the power supply) and repeatedly during the measurement by recording the critical field. All these measurements give values in the range of -0.8 mT to -0.65 mT . The appropriate value was taken as a reference for zero field.

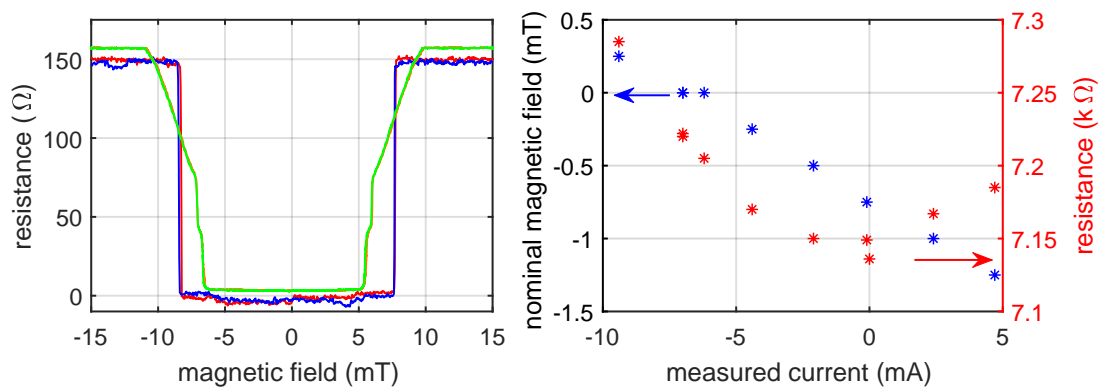


Figure A.6: Investigating the shift in magnetic field: **a)** Different measurements of the critical field lead to a shift of the sweeps to negative field. Samples: Red/blue: Al_31-II-06; Green/orange: AlAu_29-I-09. **b)** The reading of the power supply (left/blue) and the resistance of an atomic aluminium contact (right/red) are shown as a function of the measured current through the superconducting magnet. A minimal resistance is expected for zero magnetic field, because of the splitting of Cooper pairs caused by magnetic fields.